TIME RESOLVED MEASURMENTS OF DANGLING BONDS AND SURFACE STRUCTURES

BY

ERIKA A. LLOYD

A thesis submitted in partial fulfillment of the requirements for the degree of

Master of Science

Department of Physics

University of Alberta

ABSTRACT

This thesis will discuss the charge dynamics of dangling bonds (DBs) on the hydrogen terminated Si(100) surface under the effects of temperature and perturbations from local electric fields. The experimental methods are then extended towards DB chains. Electronic time resolved imaging techniques have been developed to create fast images of electron capture on a single DB - showcasing the mechanism behind atomic Negative Differential Resistance (NDR). This feature and its associated dynamics are further explored with experiments at 77 K and room temperature. A pump probe imaging technique was implemented and used to spatially capture the (+/0) transition level coming in to resonance with the valence band. It will be shown that a DB is sensitive to local fields and, once characterized, the DB can be used as a tool to probe the native charge properties of other structures on the surface. Of particular interest will be a bare dimer and DB chains of various lengths. These chains are then explored using DC, dI/dV, and time resolved methods. A tangential effort on the Si(111)-H surface will be mentioned, and will present a 6 atom Si "benzene" structure. The advantages of a symmetric surface will be discussed, and it's potentially useful 2x1 zig-zag reconstruction upon desorption of Hydrogen.

PREFACE

Some of the DC and time resolved images in Ch.5 have appeared in [27]. Also from this publication are the calculated rates in Fig.27. The dI/dV linescans in Ch.6 have appeared in [36]. The band diagram Fig.12 was taken from [37]. All other content is original.

ACKNOWLEDGMENTS

Above all, is my gratitude to my family. Where words fail me, I will try a few: I thank my caring mother whose strong mind, and lasagna, point me straight when I waver; my tinkering father who is always "up to no good" with crazy, fun projects; my brother for his humorous approach on life's most challenging curve-balls; my sister, who knows me better than anyone; and to Cat, for giving me a good meow when I need it.

To the group, for creating an environment that makes work not feel like work: John Wood, Taleana Huff, Roshan Achal, Jeremiah Croshaw, Wyatt Vine, Dr. Jason Pitters, Dr. Bruno Martins, Dr. Mohammad Koleini, Dr. Radovan Urban, Dr. Hedieh Kalachahi, Dr. Paul Piva and Dr. Isil Oxfidan. A special thanks to Mark Salomons and Martin Cloutier, whose technical and heroic skills maintain the machines that make our work possible.

Although he would prefer I buy him coffee over yet another expression of my gratitude, I thank Dr. Mohammad Rashidi, or Moe, for his guidance through all of my work. His experimental insight and technical skills make him a researcher to strive to be.

I sincerely thank my committee members Professor John Beamish and Professor Joseph Maciejko, for sparring me their time, patience, and advice.

Finally, my supervisor Dr. Robert Wolkow, who has been encouraging me since my undergraduate degree. His unique atomic insights and unrelenting enthusiasm has shaped the way I see and think - a true privilege I will carry with me in the years to come. Between the serious and humorous talks in the lab, to sharing tea and watching the birds – he creates an atmosphere with his students for genuine conversation, and continuously shows his support for their growth. Not only has he provided me with the opportunity, but also the confidence to be successful. For this and more, my gratitude is immeasurable.

CONTENTS

LIST OF FIGURES

ACRONYMS

STM Scanning Tunneling Microscopy

FIM Field Ion Microscopy

TIBB Tip Induced Band Bending

MCP Multi-Channel Plate

RF Radio Frequency

DB Dangling Bond

CB Conduction Band

VB Valence Band

FCC Face Centered Cubic

NDR Negative Differential Resistance

NEGF Non Equilibrium Green's Functions

NC-AFM Non Contact Atomic Force Microscopy

1

AN INTRODUCTION

This thesis is a study of atomic structures using the various methods made possible with a Scanning Tunneling Microscope (STM). First developed in 1982 by Binnig and Rohrer, the STM remains unique in it's ability to probe and manipulate individual atoms on a surface [4]. Its capabilities are continuously growing with sophisticated designs, some of which will be showcased here. The most novel being the all electronic time resolved measurements pioneered by Loth et al [22] which enables us to capture dynamics on the surface.

The STM is based on a very fundamental feature of Quantum Mechanics, tunneling. An atomically sharp metal probe is brought within a nanometer of the surface of a sample where an applied voltage will sustain a tunneling current. Since the electrons are traveling through the vacuum barrier the collected current will depend on the distance they have to travel. Using this principle the STM is able to create topographic maps of the surfaces of materials with atomic sensitivity. The most renowned being the 7x7 reconstruction of the Si(111) surface [5].

Our system is the hydrogen terminated Si(100)-2x1 surface. With the STM tip we are able to remove single hydrogen atoms to leave behind an isolated orbital. We call these Dangling Bonds (DBs), and their ability to hold up to two electrons has made them of great interest both scientifically and technologically. We will use time resolved techniques to probe the charge dynamics of single DBs and image electron capture events, as seen in [27]. This characterization is a necessary step in applying DBs as building blocks for larger, more complicated structures, with the eventual goal of making an atomic scale device. To this end, the interactions between DBs must be well understood. We will first explore closely spaced tunnel coupled DBs, building off the work of Wood et al [36], whose properties are important for possible applications in silicon based charge qubits [20]. We will then

look at relatively large distances where electrostatics are dominant. These effects may play an essential role in a device such as a silicon based Quantum Cellular Automata (QCA) architecture which is a transistorless form of binary logic [9].

2

INSTRUMENTATION

All work presented in this thesis was performed on an Omicron Low Temperature machine as pictured in Fig.1 and which was setup by previous group members prior to my involvment. An array of pumps maintains the chambers in ultra high vacuum (UHV), and the cryostat surrounding the scanner allows for operation at liquid helium temperatures. Additional chambers have been added to the system for sample and probe preparations, and electronics have been added for customized experiments. The hardware and controlling software enables probing of the same atomic structure for extended periods of time – from hours to days. This is the second Low Temperature machine in our lab, and has been appropriately named LT2.

2.1 THE SCANNER AND ELECTRONICS

The Scanner is the centerpiece of the machine, designed for both sub angstrom displacements and pico amp current measurements. The schematic in Fig.2 shows the scanner and the outside electrical components whose functions will be explained in this section. The tip is connected to both a coarse motor and piezoelectric materials which enable it to move while the sample stays stationary. A DC bias is applied to the sample while the tip is connected to ground or to a signal source for time resolved measurements. The current is collected at the sample end with a pre-amplifier.

The Nanonis SPM controlling software is able to control the tip sample distance z and the applied bias V_{DC} as it collects the corresponding current. There are two main types of scan modes. The first is a constant current mode that uses a

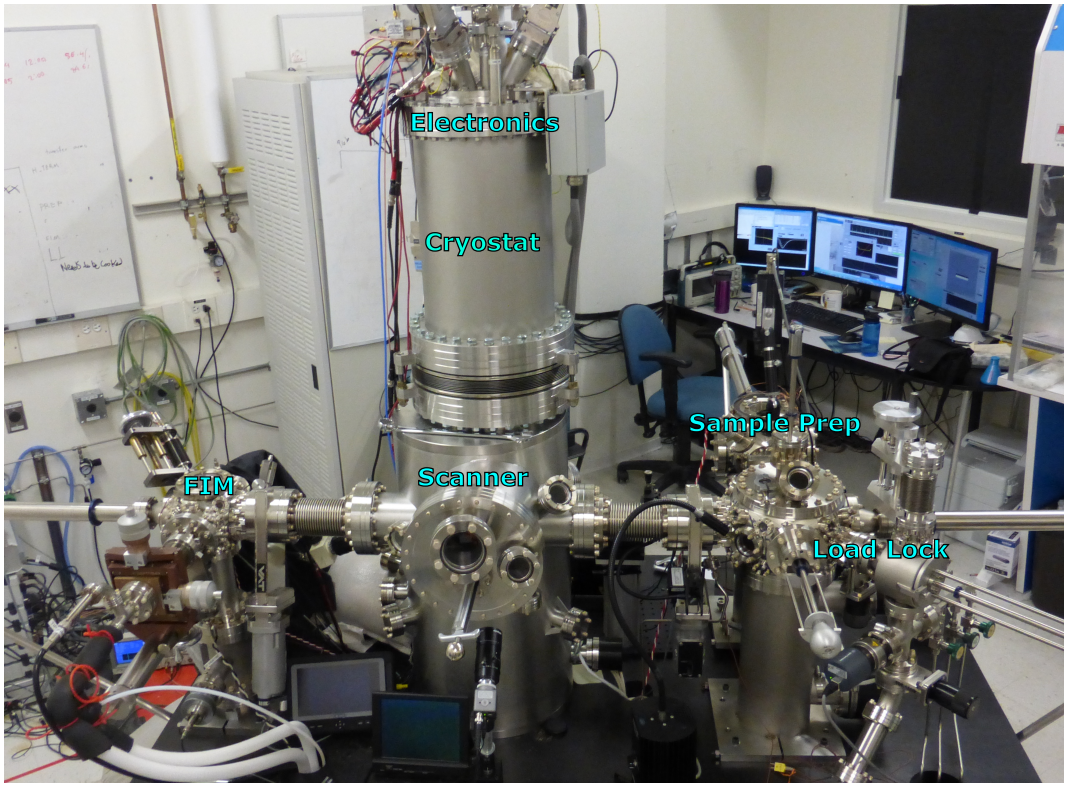

Figure 1: LT2 - An Omicron low temperature Scanning Tunneling Microscope. Supporting chambers include the load lock, the sample preparation chamber, and the field ion microscopy chamber. Specialized electronics include rf wiring, a lock-in amplifier, and a pre-amplifer.

feedback loop with the set point specified by the current at a given bias. As the tip moves across the surface the distance from the sample z is adjusted to maintain the defined set point. The collected z heights are stitched into an image creating a topographic map of the surface with atomic resolution. The second scan mode is at a constant height which is set by specifying a current and a bias, and then turning the feedback loop off. Rastering the tip and collecting the corresponding current will create a conductivity map of the scanned area. Fig.3 shows a DB scanned in constant height mode in (a) and constant current (b) with the same set point.

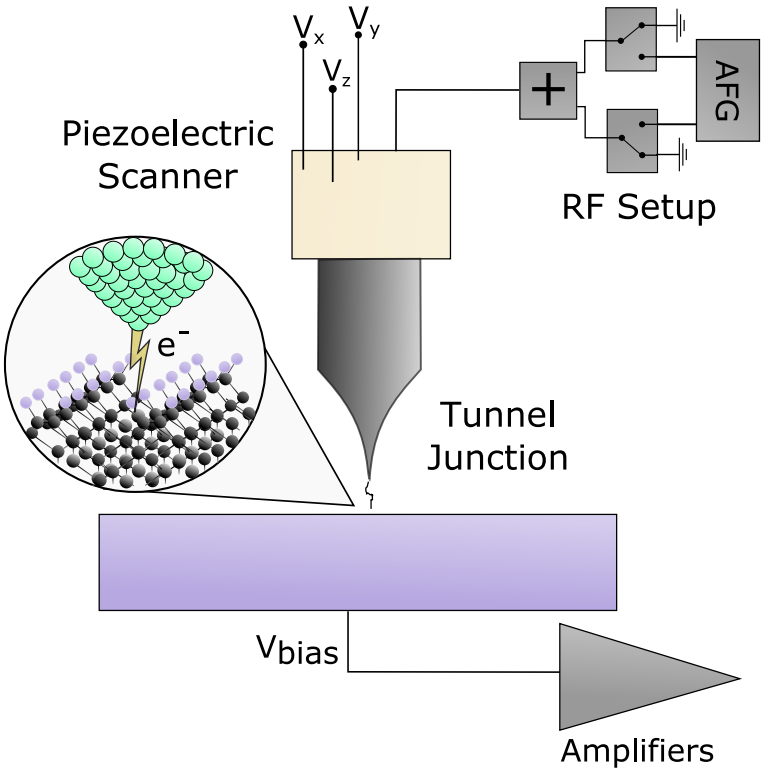

Figure 2: Schematic of the STM setup. The metal tip moves relative to the sample surface by applying voltages to the piezoeletric materials in the scanner. The RF wiring features the two outputs of the Tektronix AFG3252C signal generator with their respective switches that connect either to signal or ground. The signals are inputted to an adder and then fed to the tip. The DC bias is applied at the sample where the tunneling current is read with the pre-ampifier.

2.1.1 *RF Wiring*

The unique feature of LT2 is the radio frequency (rf) capable wiring with a 500 MHz bandwidth. This allows for time resolution on the order of nanoseconds. An rf switch (Mini-Circuits ZX80-DR230-S+) is connected to each of the two output channels of an arbitrary function generator (Tektronix AFG3252C), which switches between the channels and ground. These signals are then fed into an adder (Mini-Circuits ZFRSC-42-S+), and connected to the tip. This allows for pump probe type measurements with one channel as the pump and one channel as the probe. Applying a bias to the tip effectively shifts the ground of the tunnel junction. Special

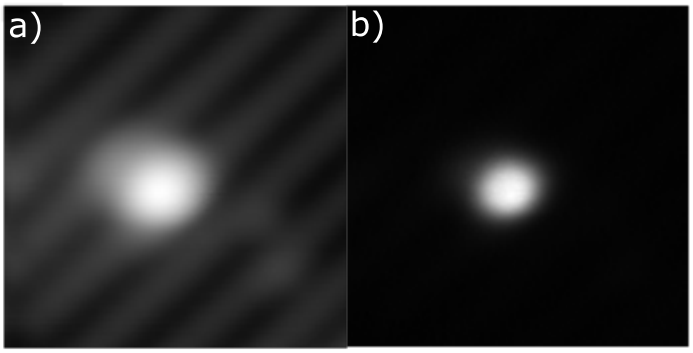

Figure 3: Different Scan modes. a) Constant current mode with set points V=-1.7 V and 30 pA. The image visually represents the changes in height needed to maintain the current setpoint. b) Constant height mode with height set at V=-1.7 V and 30pA over Si-H. The image visually represents the current collected at a given height with no feedback.

care is taken to eliminate sources of ringing, such as smearing the edges of the applied pulses. Auto-correlation signals are measured on H:Si to monitor the quality of the pulses at the junction and is used for calibration. For very short pulses the applied bias is not necessarily the voltage that reaches the tunneling junction, and a voltage shift may be needed. Typically this is only necessary for pulses on the order of $10 - 30$ ns which can experience a distortion at the junction. There are many parameters that can be varied in a time resolved measurement, these include: pulse amplitude, pulse frequency, pulse width, and relative delay between pump and probe pulse pairs.

2.1.2 *Lock-in amplifier*

Traditionally a lock-in amplifier can be used to extract very small amplitude signals from the noise. Locked at a chosen frequency, the applied voltage oscillates with a constant amplitude as the differential current is collected and integrated over time. Signals that are not at the specified frequency will be rejected and not contribute to the output. Such a measurement relates information about the local

density of states under the tip. For our measurements the DC bias is modulated with a 30 mV peak to peak signal at about 800 Hz. The assumption is that the dI/dV is constant over the oscillation amplitude, such that the measured signal is proportional to dI/dV at that bias. This measurement will become important in Ch.6 when we look at the electronic structure of Dangling Bond chains.

2.2 LOW TEMPERATURE

The scanner is surrounded by two successive shells of cryostats. This design allows the machine to operate at 4.5 K , 77 K and room temperature with the appropriate application of helium and nitrogen liquids. Room temperature experiments can be conducted with both cryostats empty. For operation at 77 K both the inner and outer cyrostats are filled with liquid nitrogen – this has a hold time of about 3 days. For 4.5 K the outer crysostat is filled with liquid nitrogen and the inner is filled with liquid helium which boils off after about 2 days. For minimal loss, the boil off is collected into a helium recovery system where the gas is compressed and liquefied to be reused.

The importance of low temperature (LT) is many-fold. For the physical system of interest it separates out the thermally activated processes, and reveals energetic features that may otherwise be washed out. This can be quantified in terms of the magnitude of $k_B T$, which for room temperatures is $\sim$ 25 meV, for 77 K is $\sim$ 6.6 meV, and 4.5 K is $\sim$ 0.39 meV. These values place a lower limit on the energetic resolution of experiments at those temperatures. LT also benefits scanning operation by eliminating piezoelectric creep, a thermally activated phenomena. The stability in tip position at liquid helium temperatures allows for averaged experiments to be performed over an extended period of time.

2.3 ULTRA HIGH VACUUM

A necessary feature of this system is its operation in Ultra High Vacuum (UHV), or approximately $1x10^{-11}$ Torr. Pressures this low are required for a sample to remain clean for the duration of an experiment. This is attained through the use of various types of pumps. The first stage from atmosphere (760 Torr) is a roughing pump which brings a chamber down to around $1x10^{-3}$ Torr. Turbo molecular pumps are then used to pump chambers to the edge of UHV. Ion pumps bring and maintain the machine at UHV and are supplemented with periodic uses of Titanium Sublimation Pumps (TSP). Cryopumping will also be present inside the inner cryostat where the sample sits – the pressure is not measured here but is expected to be much lower. Loading and unloading of tips and samples is done through a load lock, acting as the interface of the STM system to the (dirty) outside world. This is a small chamber that can be quickly pumped down from atmosphere to around $1x10^{-7}$ Torr in order to make transfers into the STM chambers. Periodically the machine must be baked in order to remove contaminants, mainly water, which stick to the walls of the vacuum chamber. This process consists of heating the entire machine to 130°C for a few days with the pumps active.

2.4 FIELD ION MICROSCOPY

Field Ion microscopy (FIM) is a method used to atomically resolve crystal structures of sharp materials. It can also be used to implement an etching procedure to fabricate single atom tips that are used as STM probes. The most widely used tip material is tungsten and will be used in this thesis. Prior to FIM a tungsten wire is electrochemically etched in a NaCl solution producing a tip that appears sharp under an optical microscope. It is then loaded into the FIM chamber for in situ processing which includes baking to 900°C and cleaning by electron bombardment from a hot filament – referred to as e-beaming.

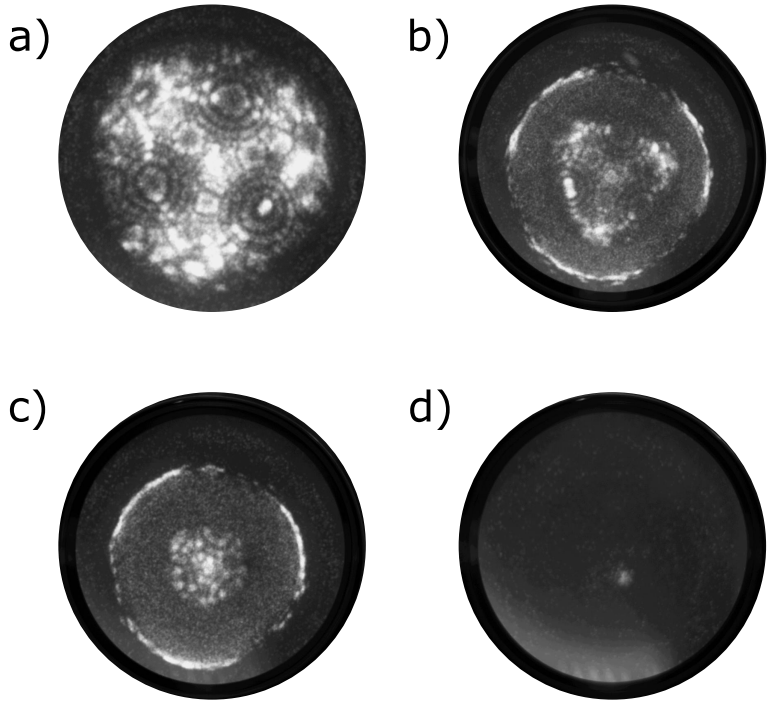

Figure 4: Four FIM images of a Tungsten 111 wire at different etching stages. a) Shows the Helium imaging. b-d) Show the nitrogen etching process, which finishes in a single emitting atom.

2.4.1 *Helium Imaging*

Once the tip has gone through the coarse etch and preliminary in situ cleaning – it can now be imaged in the FIM chamber with the introduction of Helium gas at a partial pressure of $1x10^{-6}$ Torr. Experimental set up includes the tip, a Multi-Channel Plate (MCP) and a screen. The MCP is set to -1700 V to accelerate the ions towards it from the tip, and the screen is set to $+2500$ V to collect the electrons from the MCP. A voltage applied to the tip creates a high field at the apex that will ionize impinging Helium atoms. The surface corrugation renders ionization more likely at atomic sites rather than in between them. Once ionized the atoms will be accelerated into the MCP. Here, the ions create an avalanche of secondary electrons that are accelerated towards the screen – creating a visible image that reflects the position of the apex atoms. An FIM image of the tungsten (111) tip with Helium gas is shown in Fig.4(a). The voltage applied to the tip starts from

0 and is increased until crystal structure is observed, anywhere from $3 - 25$ kV. A sharper tip will image at lower applied bias. The imaging process also further cleans the tip of weakly bound adsorbates through field evaporation.

2.4.2 *Nitrogen Etching*

The tip will sharpen under the exposure of N_2 gas at a partial pressure of $1x10^{-6}$ Torr. Nitrogen reacts with the tungsten tip creating a protrusion which then gets ionized and swept away by the field, taking tip material with it. An applied voltage will create a strong enough field at the apex of the tip to ionize the gas before it is etched. The etching occurs in a ring around the field protected apex. By slowly lowering the applied voltage the etching ring will move up the tip. This can be done until the apex has reached a single atom [30]. The etching is done simultaneously with the Helium imaging to keep track of the sharpening process. Fig.4(b-c) shows the etching of a tip to a single atom.

2.5 SAMPLE PREPARATION

Samples discussed in this thesis have all been prepared in-situ using the sample preparation chamber. The main advantage of this method over wet preparation is the cleanliness of the sample which is a top priority for controlled scanning and measurements. The chamber is equipped with contacts for the sample holder that are used to pass current and heat the sample. Upon initial loading, samples are typically brought in to this chamber and heated at 600°C for 24 hours to degas both sample and its holder. This process is intended to remove contaminants, mainly organics, brought in from the outside. There is a leak valve used to introduce gases, namely hydrogen. Finally there is a tungsten filament that can be used to crack the H2 molecules creating a flux of H atoms.

3

SCANNING TUNNELING MICROSCOPY

This Chapter will define the framework for discussing experimental STM results. While the object of interest is the sample, its interactions with the tip create a larger system where the native sample features are part of, but not the exclusive contributor to the observed signals. Care must be taken in interpreting the STM currents to extract the valuable sample information from the probing environment. We will be addressing the methods to understand the tip-sample interactions which allow us to make comments on the sample. The tunnel junction is often discussed schematically with energy diagrams with the tip and sample as contacts. Since our sample is silicon, it is similar to the study of Metal-Oxide-Semiconductor tunnel devices where the energy diagrams represent the local environment under the tip as opposed to a mesoscopic device. We will begin our discussion using energy diagrams to describe basic transport and the common nomenclature used in this field. What follows are several analyses on the STM tunnel junction which attempt to quantify and understand the tunnel current. Finally we discuss the interpretation of STM currents specific to our system, such as the implications of probing a semiconductor.

3.1 BASIC TRANSPORT AND ENERGY DIAGRAMS

The first basic question to ask is, why do electrons flow? A current can only be sustained through an electrochemical difference between two interacting objects. Imagine two contacts connected to a conducting channel. This can be represented using energy or "band" diagrams as pictured in Fig.5(a). The vertical axis represents energy, and the horizontal axis spans the space of the junction. These dia-

grams are general, but for our purposes we will name the left contact the "tip" which will always be a metal, and the right contact will be the "sample" which is a semiconductor. The metal contact has a continuum of available states represented by the band spanning all energies. The distinguishing feature of the semiconductor is the region of energy with no states represented by the band gap. The channel is vacuum, and although it acts as an insulator, we will assume that it can support some type of current and act as a conducting channel. The contacts are connected to leads where a voltage can be applied and the current read. This corresponds to the bias we apply to the sample and the current we observe via the pre-amplifier.

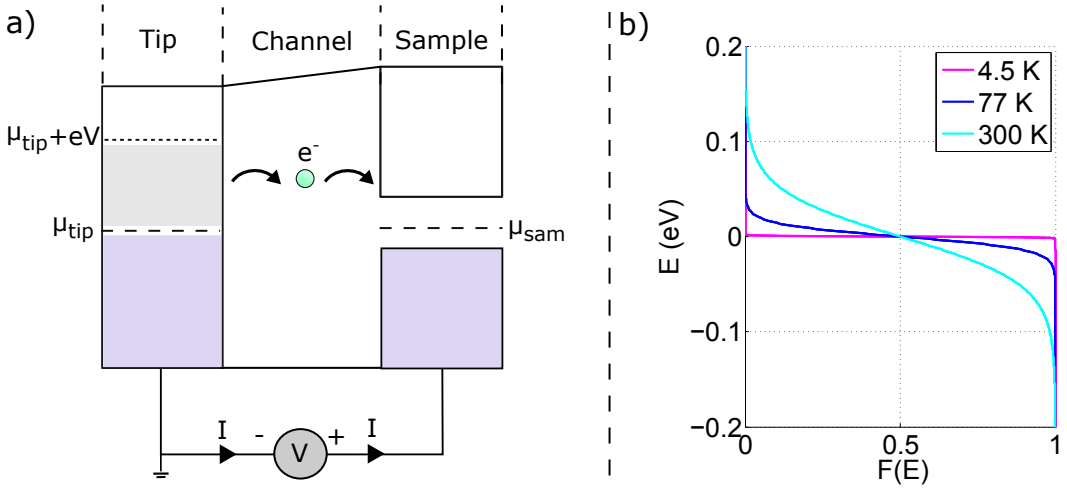

Figure 5: Energy Diagram and Fermi level. a) Shows an energy diagram spanning two contacts and a channel. For 0 applied bias the electrochemical potentials of the tip (left) and sample (right) contacts are equal and there is no net current. For an applied bias, the electrochemical potential of the tip is raised relative to the sample and there is a net transfer of electrons from tip to sample. b) The Fermi function plotted for 4.5 K, 77 K, and 300 K, where $E = 0$ is the electrochemical potential.

The dashed lines denote the electrochemical potential μ describing the work required to add an electron given the existing electronic forces on the contact. It is usually understood in terms of occupation, where states at energies below this level are "occupied" and an additional electron cannot be put into this state. The states at energies above this level are "empty" and can accept an electron at this

energy. Analogous to heat and temperature, electrons will move from high to low μ if there is an easy pathway to do so. When connected to the channel each contact will attempt to bring the electrochemical potential of the channel into equilibrium with it's own. Electrons will flow both into and out of the channel, establishing an equilibrium across the entire junction. These flows are continuous and a net current is only observed if in at steady state there is a net difference in electrochemical potential between the contacts. This difference can be maintained with an external source such as an applied bias, and is summarized in the following way:

$$eV = \mu_{tip} - \mu_{sam} \tag{1}$$

Where e is the charge of the electron, V is the applied bias, and μ_{tip} and μ_{sam} are tip and sample electrochemical potentials respectively. With no applied bias we do not expect current to flow. This corresponds to the situation where $\mu_{tip} = \mu_{sam}$, and there is no net difference in the inflows and outflows from the channel to each contact. Consider applying a bias to the sample. At positive bias, the electrochemical potential of the tip will be raised since an electron will require more energy to overcome the applied bias and be placed on the tip. If maintained at this bias there will be a net flow of electrons from the tip state to an available sample state in the exposed energy range. The scenario is similar for negative bias, where the net flow is from sample to tip states.

Occupation is formally defined using a Fermi function which quantifies the average number of electrons at an energy level E when in equilibrium:

$$f_0(E - \mu) = \frac{1}{1 + exp[(E - \mu)/k_B T]} \tag{2}$$

For energies much lower than μ the states are always occupied and $f_0 = 1$. Conversely, for energies much higher than μ the states are empty and $f_0 = 0$. The Fermi function takes into account the thermal energy of the electron at finite temperature. This causes a smearing of the Fermi function by $k_B T$ around μ [34]. Fig.5(b) plots the Fermi function for 4.5 K, 77 K, and room temperature 300 K. For lower temperatures the function becomes step like, and higher temperatures causes broadening as the available occupations grow. For our discussions the bias is always applied to

the sample, and we visualize the Fermi level of the tip changing. For each contact the Fermi functions are defined as:

$$f_{tip}(E) = \frac{1}{1 + exp[(E - \mu_{tip})/k_B T]} \tag{3}$$

$$f_{sam}(E) = \frac{1}{1 + exp[(E - \mu_{sam})/k_B T]} \tag{4}$$

The Fermi function is centered at the electrochemical potential, and since we operate at low temperature the Fermi level E_f and electrochemical potential μ will be used synonymously.

By collecting current for a range of voltages we can extract features of the band structure of silicon. At a given voltage, the observed current is related to the difference in occupation of each contact weighted by number of states of each contact at that level. This gives us the following expression:

$$I \propto \int \left[f_{tip}(E) - f_{sam}(E)\right] \rho_{tip}(E) \rho_{sam}(E) dE \tag{5}$$

Where $\rho_{tip}(E)$ and $\rho_{sam}(E)$ represent the tip and sample density of states respectively. The integration only runs from energies in between μ_{sam} and μ_{tip} because this is the energy range the tunneling current is drawn from. With the low temperature assumption the Fermi functions can be replaced by step functions giving:

$$I \propto \int_{E_f^{sam}}^{E_f^{tip}} \rho_{tip}(E) \rho_{sam}(E) dE \tag{6}$$

This shows that the collected current is a convolution of the density of states of the two electrodes in a symmetric and interchangeable way [6]. Confirmation of this comes from having a metallic tip and semiconducting sample, where an I(V) curve will have an identifiable band gap. A full expression would be found if we

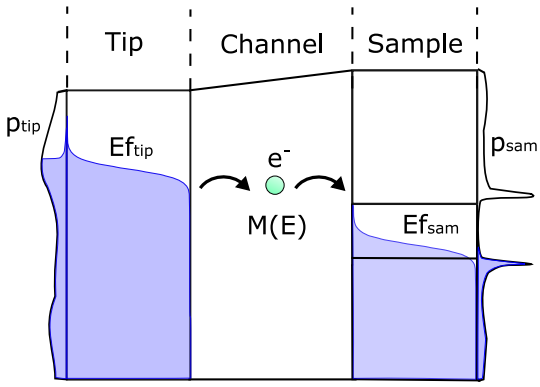

Figure 6: Energy diagram with the Fermi level at finite temperature and superimposed density of states.

understood what happens in the channel. We sum this up in what is called a "tunneling matrix" $M_{\mu\nu}$ whose elements we will attempt to unravel in the next section. Including this term the collected current at a given voltage can be expressed as:

$$I = \frac{4\pi}{\hbar} \int_{E_f^{sam}}^{E_f^{tip}} |M_{\mu\nu}|^2 \rho_{tip}(E) p_{sam}(E) dE \tag{7}$$

3.2 THE STM TUNNEL JUNCTION

Now that we have discussed why an electron would want to move from one contact to the other, now we shall describe how it will do so. Tunneling phenomena is one of the fundamental features of quantum mechanics, and the theory which is derived here has a rich history in the efforts to conceptually understand it. STM continues to be a platform for the study of tunneling phenomena. This section will discuss one-dimensional transport in the context of STM, whose currents travel through a vacuum barrier.

3.2.1 *Current vs Tunneling Current: Examples from Landauer*

Immediately, a distinction must be made between current, and tunneling current. We will do this with a 1D Landauer formalism comparing ballistic trans-

port through a conductive channel with one that has no states. If G describes the conductance of the channel, the basic expression for current is:

$$I = GV \tag{8}$$

In the Landauer formalism we can express the conductance in terms of a transmission coefficient T:

$$G = G_0 T \tag{9}$$

where G_0 is the quantum of conductance and is the upper limit of what a single state can transport. This value is defined in terms of fundamental constants:

$$G_0 = \frac{2e^2}{h} \approx 80nA/meV \tag{10}$$

The character of the channel becomes summarized in the transmission coefficient T. In either case, the system will satisfy the time dependent Schrödinger equation:

$$i\hbar\frac{\partial\Psi}{\partial t} = \left(-\frac{\hbar^2}{2m}\frac{\partial^2}{\partial z^2} + U(z)\right)\Psi \tag{11}$$

To simplify, we split the problem and solve for each contact independently. This will give stationary states:

$$\begin{aligned} \Psi(z) &= \psi_\mu(z)e^{-iE_\mu t/\hbar} \\ \Psi(z) &= \chi_\nu(z)e^{-iE_\nu t/\hbar} \end{aligned} \tag{12}$$

Where ψ_μ and χ_ν are the tip and sample states with eigenenergies E_μ and E_ν. If we assume plane wave solutions in both contacts, then we can describe the states as "modes", defined by their wavevector k.

$$\begin{aligned} \psi_\mu(z) &= Ae^{ikz} + Be^{-ikz} \\ \chi_\nu(z) &= Ce^{-ikz} + De^{ikz} \end{aligned} \tag{13}$$

In the channel we can assume that all right traveling waves +k will have originated from the tip and left traveling waves -k are from the sample. The transmission between contacts through a conductive channel will depend on the available modes

within the channel, defined for example by a square well – similar to a waveguide [33]. The transmission coefficient can be understood as the probability of finding an electron from the tip at the sample. If the contacts are reflectionless, as depicted in Fig.7(a), a +k mode traveling from the tip through the channel and into the sample will do so freely. In other words, the impinging current from that mode at the beginning of the junction $I(0)$ is equal to that at the end of the junction $I(z_0)$ giving us a transmission of 1.

$$T_{\mu\nu} = \frac{I(z_0)}{I(0)} = \frac{|\psi_\mu(z_0)|^2}{|\psi_\mu(0)|^2} = 1 \tag{14}$$

Where $T_{\mu\nu}$ indicates the transmission from the ψ_μ state of the tip to the χ_ν state of the sample. This is for a single mode, and can be extended to as many modes in the relevant energy range. We define the conductance of N modes as:

$$G = G_0 \sum_N T_N = G_0 N \tag{15}$$

This is true for a channel that can support modes. In contrast, the STM junction is vacuum with no available states. Conduction through the STM junction can be viewed like an evanescent wave as the contact states hit the vacuum barrier. The eigenstates in the tunnel barrier are given by the familiar solutions:

$$\begin{aligned} \psi_\mu(z) &= \psi_\mu(0) e^{-\kappa_\mu z} \\ \chi_\nu(z) &= \chi_\nu(z_0) e^{\kappa_\nu (z - z_0)} \end{aligned} \tag{16}$$

The decay constants κ are defined by the barrier as:

$$\begin{aligned} \kappa_\mu &= \sqrt{\frac{2m(\bar{\phi} - E_\mu)}{\hbar^2}} \\ \kappa_\nu &= \sqrt{\frac{2m(\bar{\phi} - E_\nu)}{\hbar^2}} \end{aligned} \tag{17}$$

Where $\bar{\phi}$ is the barrier height, usually taken to be an average of the work functions of tip and sample materials. For a right traveling wave, the transmission coefficient becomes:

$$T_{\mu\nu} = \frac{I(z_0)}{I(0)} = \frac{|\psi_\mu(0)e^{-\kappa_\mu z_0}|^2}{|\psi_\mu(0)|^2} = e^{-2\kappa_\mu z_0} \tag{18}$$

The tunneling conductance can be defined as:

$$G = G_0 e^{-2\kappa_\mu z} \tag{19}$$

To summarize, the transmission of a mode between identical tip and sample states through a conductive channel will have a transmission coefficient $T = 1$ and a conductance of G_0. If the mode is not supported by the channel its transmission will be determined by the energy and width of the barrier $T = e^{-2\kappa z_0}$, modifying the conductance such that $G = G_0 e^{-2\kappa z_0}$. This exponential dependence of tunneling current on barrier width is what allows STM to have such sensitivity to the atomic scale.

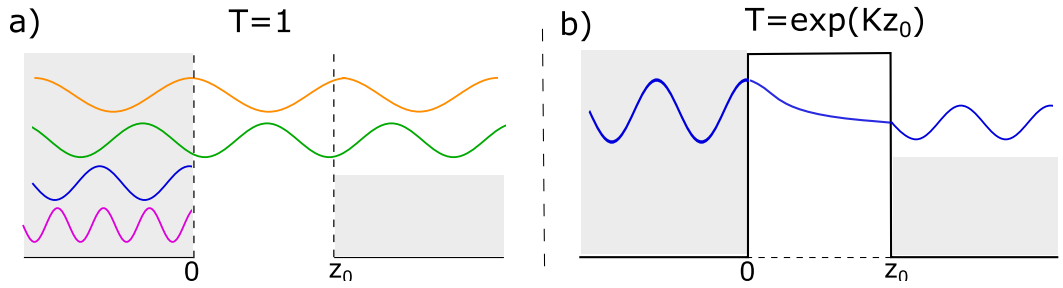

Figure 7: 1D schematics of ballistic currents in a channel, the gray shaded area denotes the Fermi level of the contacts. a) Transport through a conductive channel. The modes supported by the channel are able to pass from the tip to the sample with a transmission coefficient of 1. b) Transport through a channel that has no available states. The modes from the tip leak into the channel and decay as e^{-kz}. For small enough barriers a there will exist a finite tip state that reaches the sample.

While the expressions give a qualitative description of transport through the tunneling junction, analytical expressions for the current that can be compared

with experiments do not follow trivially. Comparing the transmission term from the Landauer formalism with Eq.7 we can define:

$$T_{\mu\nu} = 2\pi^2 |M_{\mu\nu}|^2 \rho_{tip}(E)\rho_{sam}(E) \tag{20}$$

Where we see that this analysis has lacked details of the contacts, such as the density of states, and focuses only on what occurs in the channel. Further, in evaluating the transmission between tip and sample we have assumed that tunneling will occur between two equivalent states from each contact. In reality the solutions of each contact are neither identical nor trivial. Work has been done by Chen to determine what wavefunctions of both tip and sample are involved in tunneling and evaluating the matrix elements $M_{\mu\nu}$ [6]. It pivots on adopting a perturbative philosophy, where we posit a rate through which transitions between tip state μ to sample state ν occur:

$$p_{\mu\nu}(t) = \frac{2\pi}{\hbar^2} |M_{\mu\nu}|^2 \tag{21}$$

This is the premise of the Bardeen tunneling formalism which we will now turn to.

3.2.2 *The Tunneling Matrix: Bardeen Tunneling*

Instead of viewing transport in terms of transmission of eigenstates through a channel from their respective reservoirs, we can view it as a transfer between two weakly coupled reservoirs. What will be derived here is Bardeen's first order perturbation theory which is widely applied in solid state systems and was originally developed to connect tunneling experiments to the Bardeen-Cooper-Schrieffer theory of superconductivity. Formulating it using nonequilibirum Green's functions (NEGF) would show explicitly its correspondence to a Landauer formalism, here however we will take the "traditional" approach. A full tutorial comes from [13] and [6], and the NEGF method is described in [7] and [19]. The theory is perturbative in nature, and $M_{\mu\nu}$ expresses the transport ability between states due to the perturbing potential $U(z)$. Their final form describes the "overlap" between

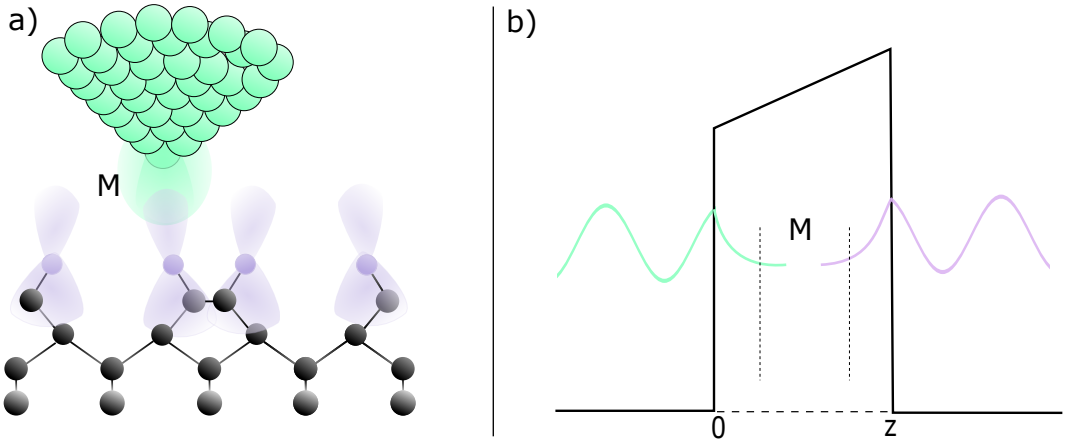

Figure 8: Visualizing the overlap matrices $M_{\mu\nu}$. a) Spatial schematic of the STM Junction and the wavefunctions of both tip and sample atoms. Tunneling occurs in the overlapping region in the junction between the tip and sample atom. b) Energy schematic of two contacts whose states are weakly coupled in the channel.

the tip and and sample wavefunctions that are involved in the tunneling process, this is shown schematically in Fig.8. Like the previous section, Bardeen's approach separates the problem into different subsystems that are easy to solve, and then it introduces a weak coupling between them. The contacts will have stationary states:

$$\Psi = \psi_\mu e^{-iE_\mu t/\hbar}$$

$$\Psi = \chi_\nu e^{-iE_\nu t/\hbar} \tag{22}$$

and satisfy the time independent equations:

$$\left[-\frac{\hbar}{2m}\frac{\partial^2}{\partial z^2} + U_{tip} \right] \psi_\mu = E_\mu \psi_\mu$$

$$\left[-\frac{\hbar}{2m}\frac{\partial^2}{\partial z^2} + U_{sam} \right] \chi_\nu = E_\nu \chi_\nu \tag{23}$$

The eigenfunctions ψ_μ and χ_ν of the isolated electrodes will be referred to as "tip states" and "sample states" respectively. Bringing the two systems together will create a combined Hamiltonian which satisfies the Schrödinger equation:

$$i\hbar\frac{\partial\Psi}{\partial t} = \left(-\frac{\hbar^2}{2m}\frac{\partial^2}{\partial z^2} + U_{tip} + U_{sam}\right)\Psi \tag{24}$$

Focusing on a tip state, this combined potential will alter the time evolution of ψ_μ such that there is a finite probability for it to transfer to a state in the sample χ_ν. This is expressed as:

$$\Psi = \psi_\mu e^{-iE_\mu t/\hbar} + \sum_{\nu=1}^{\infty} c_\nu(t)\chi_\nu e^{-iE_\nu t/\hbar} \tag{25}$$

where the coefficients $c_\nu(t)$ are determined by Eq.24 with the condition of $c_\nu(0) = 0$. A basic assumption is that these two sets of wavefunctions are nearly orthogonal:

$$\int \psi_\mu^* \chi_\nu d^3\mathbf{r} \cong 0 \tag{26}$$

Which is an application of Oppenheimer's perturbation theory. Inserting the trial wavefunction gives:

$$i\hbar\sum_{\nu=1}^{\infty}\frac{dc_\nu(t)}{dt}\chi_\nu e^{-iE_\nu t/\hbar} = U_{sam}\psi_\mu e^{-iE_\mu t/\hbar} + U_{tip}\sum_{\nu=1}^{\infty} c_\nu(t)\chi_\nu e^{-iE_\nu t/\hbar} \tag{27}$$

The second term on the right hand side of this equation is considered second order infinitesimal. A second application of Oppenheimer's perturbation theory is that tunneling is weak enough for a first order approximation to be valid:

$$i\hbar\frac{dc_\nu(t)}{dt} = e^{-i(E_\mu - E_\nu)t/\hbar}\int_{z>z_0}\psi_\mu U_{sam}\chi_\nu^* d^3\mathbf{r} \tag{28}$$

The integral is only evaluated in the sample $z > z_0$ where U_{sam} is non zero. Here is where the tunneling matrix elements are defined as:

$$M_{\mu\nu} = \int_{z>z0}\psi_\mu U_{sam}\chi_\nu^* d^3\mathbf{r} \tag{29}$$

A time integration of Eq.28 gives:

$$c_\nu(t) = M_{\mu\nu}\frac{e^{-i(E_\mu - E_\nu)t/\hbar} - 1}{E_\mu - E_\nu} \tag{30}$$

The coefficients $|c_\nu(t)|^2$ evaluate the probability of having a tip state μ at time $t = 0$, and a sample state ν at time t. These amplitudes are expressed as:

$$p_{\mu\nu}(t) = |c_\nu(t)|^2 = |M_{\mu\nu}|^2\frac{4sin^2[(E_\mu - E_\nu)t/2\hbar]}{(E_\mu - E_\nu)^2} \tag{31}$$

The probability is maximal at $E_\mu = E_\nu$ and drops off quickly otherwise. The tunneling current will depend on how many states of the sample near energy E_μ are available for the tip states to tunnel into, in other words $\rho_{sam}(E_\mu)$. With this restriction, the total probability of a tip state ψ_μ at energy E_μ in a time interval t is given by:

$$p_{\mu\nu}(t) = \frac{2\pi}{\hbar}|M_{\mu\nu}|^2\rho_{sam}(E_\mu)t \tag{32}$$

We can impose elastic tunneling by looking at the integral identity:

$$\int_{-\infty}^{\infty}\frac{sin^2(au)}{\pi au^2}du = 1 \tag{33}$$

The integrand will approach a delta function if values of a are large. The time for tunneling is assumed to be much greater than the interval $\hbar/\Delta E$, such that Eq.31 will only be non zero for $E_\mu = E_\nu$.

By imposing this elastic condition the matrix elements can be converted into an integral that depends only on the unperturbed wavefunctions of each electrode at the separation surface. Beginning with the application of Eq.23 for the sample, the potential in 29 is replaced such that:

$$M_{\mu\nu} = \int_{z>z0}\psi_\mu\left(E_\nu + \frac{\hbar^2}{2m}\frac{\partial^2}{\partial z^2}\right)\chi_\nu^* d^3\mathbf{r} \tag{34}$$

Using the elastic condition $E_\mu = E_\nu$:

$$M_{\mu\nu} = \int_{z>z0} \left(\chi_\nu^* E_\mu \psi_\mu + \psi_\mu \frac{\hbar^2}{2m} \frac{\partial^2}{\partial z^2} \chi_\nu^* \right) d^3\mathbf{r} \tag{35}$$

Now applying Eq.23 for the tip, and taking its potential U_{tip} to be zero at the sample gives:

$$M_{\mu\nu} = \int_{z>z0} -\frac{\hbar^2}{2m} \left(\chi_\nu^* \frac{\partial^2 \psi_\mu}{\partial z^2} - \psi_\mu \frac{\partial^2 \chi_\nu^*}{\partial z^2} \right) d^3\mathbf{r} \tag{36}$$

With the following identity:

$$\chi_\nu^* \frac{\partial^2 \psi_\mu}{\partial z^2} - \psi_\mu \frac{\partial^2 \chi_\nu^*}{\partial z^2} = \frac{\partial}{\partial z} \left[\psi_\mu \frac{\partial \chi_\nu^*}{\partial z} - \chi_\nu^* \frac{\partial \psi}{\partial z} \right] \tag{37}$$

We can carry out an integration over z, giving our final result:

$$M_{\mu\nu} = \frac{\hbar^2}{2m} \int_{z=z_0} \left[\psi_\mu \frac{\partial \chi_\nu^*}{\partial z} - \chi_\nu^* \frac{\partial \psi}{\partial z} \right] dxdy \tag{38}$$

If the wavefunctions involved in tunneling are known, then their overlap in the barrier region can be calculated directly from this expression. The potential itself does not appear explicitly, and the only required information is the tip-sample distance z_0 – which controls the extent of "coupling" between the two electrodes.

Assuming the density of states does not vary appreciably near the Fermi level, the associated current for tunneling states of the tip $\rho_{tip}(E_f^{tip})$ in the energy interval V is:

$$I = \frac{2\pi e^2}{\hbar} |M_{\mu\nu}|^2 \rho_{tip}(E_f^{tip}) \rho_{sam}(E_f^{sam}) V \tag{39}$$

Where we have recovered the tunneling conductance

$$G = 2\pi^2 G_0 |M_{\mu\nu}|^2 \rho_{tip}(E_f^{tip}) \rho_{sam}(E_f^{sam}) \tag{40}$$

And integration for the total tunneling current will correspond to Eq.7, but now with matrix elements defined by Eq.38.

3.3 SEMICONDUCTORS AND ENERGY DEPENDENCE

Exclusively, the work presented in this thesis will be on silicon samples whose semiconducting properties have important implications on our observations. Until now we have also not considered the possible energy dependencies of the tunneling matrices. This section will discuss these remaining topics that will be important to decipher the data presented in subsequent chapters.

3.3.1 *Tip Induced Band Bending*

An important concept in the STM of semiconductors is tip induced band bending (TIBB) caused by fields in the tunnel junction. For a metal sample the potential in the channel can be easily solved using Laplace's equation. The problem becomes more difficult for a semiconductor whose charge carriers are lacking in both number and mobility, making them unable to keep the voltage throughout the sample constant. This causes some of the tip field to leak into the surface of the sample. Solutions of the channel potential must include this portion of the semiconductor and requires us to solve Poisson's equation. This voltage drop alters the native electronic structure by bending the bands near the interface. The most intensive studies on this topic have been done by Feenstra et al [12] who have made available a software called SEMITIP that calculates the extent of TIBB in STM experiments. We will go through the basics of their work here. Using finite element techniques the software solves the electrostatic potential at all points in the semiconductor. The electrostatic potential energy ϕ_T of the tip relative to a point deep within the semiconductor is related to the applied voltage V like so:

$$\phi_T = eV + \Delta\phi \tag{41}$$

Where the contact potential $\Delta\phi$ is defined in terms of the work functions ϕ of the tip and sample:

$$\Delta\phi = \phi_{tip} - \phi_{sam} \tag{42}$$

The work function describes the amount of energy required to eject an electron from the material to vacuum. For the semiconducting sample it is dependent on the electron affinity χ and the doping level which adjusts its Fermi level: $\phi_{sam} = \chi - (E_C - E_f^{sam})$. Of particular interest is the electrostatic potential at a point just below the tip denoted as ϕ_0. Even at zero bias there will be a difference in work functions of the tip and sample materials as shown in Fig.9(a). This is called the Contact Potential Difference and results in a field at the junction even at zero bias which bends the bands. In our case we use a tungsten tip with $\phi_{tip} = 4.5$ eV and a silicon sample with $\chi = 4.05$ eV and due to doping $E_C - E_f^{sam} \approx 25$ meV. This means that at zero bias $\phi_{sam} < \phi_{tip}$ causing an upward band bending effect ϕ_0. An applied positive bias will further increase this upward band bending as shown in Fig.9(b). For some negative bias there will be a flat band condition. A larger negative bias will make the tip positive with respect to the sample and cause downward band bending shown in Fig.9(c).

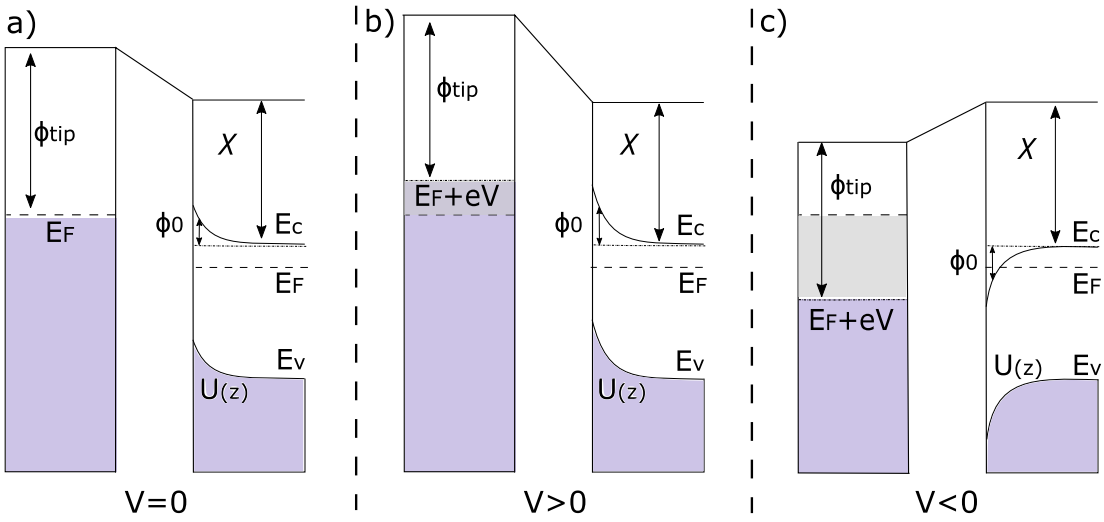

Figure 9: Schematics of Tip Induced Band Bending. a) Shows the $V = 0$ case and the contact potential difference. b) Is the $V > 0$ case showing upward band bending. c) Is the $V < 0$ case showing downward band bending

To understand the effects that band bending has on tunneling spectroscopy we look at an energy state E which would normally satisfy $E - E_f^{sam} = eV$. In the presence of band bending this will be altered such that:

$$E - E_f^{sam} = eV - \phi_0 \tag{43}$$

The influence of band bending will affect the tunneling current by shifting the spectra. This equation is effective for describing discrete states at the surface and under the tip, but a finite element method must be used to solve for the extent of band bending into the sample $U(z)$. 3D versions of this analysis can also be done to quantify the bending in the regions lateral to the apex.

Generally speaking, the bands of silicon will bend depending on the electronic environment in which it resides. The bands themselves represent the energy at which a charge carrier may occupy that state, or the energy the charge carrier will have once removed from that state. It makes sense then, that the electrostatic effects will shift the bands as it adjusts these energetic barriers. Band bending does not only occur via the tip, but also for electronically active quantities in the region of interest - for example defects or dopants. In the presence of a positive charge the bands will shift downward – and will shift upwards for a negative charge. The extent of this bending will depend on how well the charges can be screened, which can be experimentally tuned with doping. This trend is important to remember when we reach the discussion of dangling bonds states which can hold a positive, neutral, or negative charge and for the electrostatic studies in CH7.

It is noteworthy that the values of the tip work function mentioned is a bulk property. It is generally believed that the work function of a sharp tip will vary from this value and may be dependent on local geometry of the tip [10]. The "active“ work function for a tip during an experiment may be very difficult to determine.

3.3.2 *Energy Dependence and dI/dV*

An assumption by Bardeen is that the matrix elements are independent of energy. This was appropriate for his application but not so much for STM whose spectra range from ± 2 V. If we instead assume that the wavefunctions will decay given by Eq.16 and impose the elastic tunneling condition such that $\kappa_\mu = \kappa_\nu = \kappa$, the tunneling matrices will adopt an energy dependence [6]:

$$M(E) = M_{\mu\nu}(0)e^{-\kappa z_0} \tag{44}$$

This implies that higher energies will experience a smaller decay. This asymmetry is indeed observed in STM tunneling spectra, where the current magnitude at positive bias is greater than at negative bias. We do assume that κ is slowly varying with energy [6], which allows us to make use of the lock-in amplifier and its dI/dV spectra. To interpret these signals we will begin with Eq.7. Assuming that the density of states of the metallic tip is constant with respect to voltage the equation becomes:

$$I = \frac{4\pi}{\hbar}\rho_{tip}\int_{E_f^{sam}}^{E_f^{tip}} |M(E)|^2 \rho_{sam}(E)dE \tag{45}$$

For small oscillation amplitudes, the change in energy E is much smaller than $\bar{\phi}$. This allows us to assume upon taking the derivative the energy dependence of the matrix elements mentioned in Eq.44 is negligible:

$$\left(\frac{dI}{dU}\right)_{U=V} = \frac{2\pi e}{\hbar}\rho_{tip}|M(0)|^2\rho_{sam}(E_F^{sam} + eV) \tag{46}$$

$$\left(\frac{dI}{dU}\right)_{U=V} \propto \rho_{sam}(E_F^{sam} + eV) \tag{47}$$

This shows us how dI/dV measurements relate to the density of states of the sample and will be used in Ch6 to probe the electronic properties of dangling bond structures.

4

SILICON AND SURFACES

Silicon and its interfaces are a widely studied field because of their importance to the semiconductor industry where surface effects become larger as the device size becomes smaller. This chapter is an exploration of the silicon crystal and its interface with vacuum where the periodicity of the atoms is abruptly broken. As continuity is imposed the surface atoms rearrange in order to minimize their energy. This process is unique to the environmental conditions such as temperature and exposure to hydrogen atoms. The first and most important surface we discuss is the hydrogen terminated Si(100) surface followed by the Si(111) terminated and 2x1 reconstructed surfaces. The STM current probes both the bulk electronic properties and the surface effects. The collected signal does not directly reveal the atomic structure of the surface, but rather the electronic features [6]. This chapter will discuss these signals and their meaning.

4.1 THE SILICON CRYSTAL

Silicon is a covalent crystal. This means that the distribution of electrons between atoms is non uniform and is localized in specific directions – in other words, bonds [1]. The silicon atom has 14 electrons occupying $1s^2 2s^2 2p^6 3s^2 3p^2$ shells. The four valence electrons in the $3s$ and $3p$ orbitals hybridize to approximately form 4 sp^3 mixed orbitals as shown in Fig.10(a) which are capable of 4 covalent bonds. A crystal is a solid where bonding of the atoms forms a lattice that is periodic in space. The wavefunctions are periodic and symmetric, but only under a translation specified by $\mathbf{R}$. This is expressed according to Bloch's theorem:

$$\psi(\mathbf{r} + \mathbf{R}) = e^{i\mathbf{k}\cdot\mathbf{R}}\psi(\mathbf{r}) \tag{48}$$

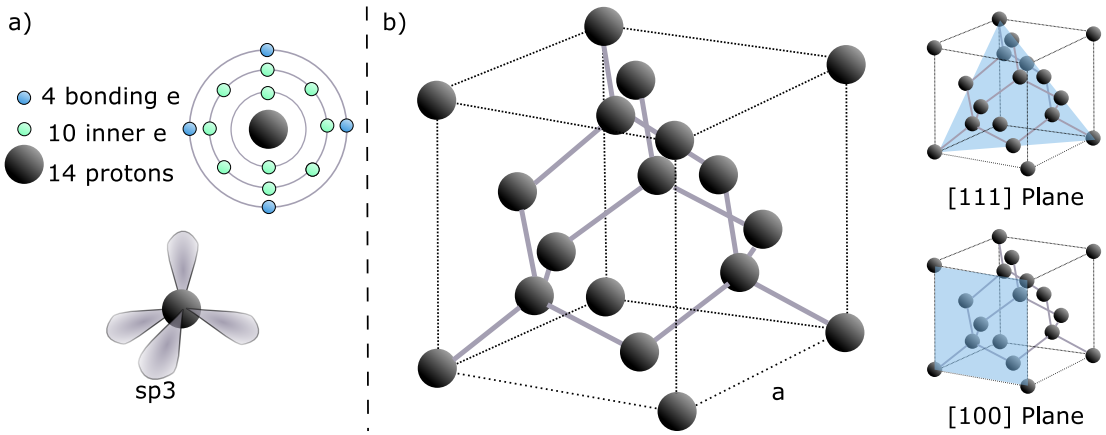

Figure 10: Silicon atom and unit cell. a) The silicon atom has 4 bonding electrons that hybridize into the sp^3 orbitals, capable of 4 covalent bonds. b) The unit cell of a silicon crystal. It a face centered cubic with two atoms per basis.

The repeating unit of the silicon crystal is shown in Fig.10(b). Translations of this unit cell will build the crystal into what is called a diamond like structure [1]. Specifically, the cell is face centered cubic with two silicon atoms per basis. A silicon wafer is most often cut along the [100] and [111] orientations shown Fig.10(b). Our primary focus will be the [100] orientation, but we will also discuss the [111] orientation.

4.1.1 *From Bonds to Bands*

When two silicon atoms are brought close together, they will minimize their energy by forming a lower energy bonding, and a higher energy antibonding state. Likewise, bonding and antibonding bands form when many atoms form a crystal shown in Fig.11(a). The electrons will populate the levels beginning in the ground state and ending at the Fermi level. A tight binding model can be used to approximate the extent of splitting that forms these bands based on the overlap of the atomic wavefunctions. It begins with the Hamiltonian of each lattice site corresponding to that of a single isolated atom:

$$H_{at}\psi_n = E_n\psi_n \tag{49}$$

Where ψ_n represents the atomic wavefunctions of the atom. Corrections to this wavefunction for an atom in a periodic crystal will be of the form:

$$H = H_{at} + \Delta U(\mathbf{r}) \tag{50}$$

Which will still satisfy the Bloch criteria given in Eq.48 with periodic boundary conditions. The corrected wavefunctions $\phi(\mathbf{r})$ may be approximated by a linear combination of the isolated orbitals:

$$\phi(\mathbf{r}) = \sum_n c_n \psi_n(\mathbf{r}) \tag{51}$$

The corrections of $\Delta U(\mathbf{r})$ mainly appear in what is called an overlap integral, approximating the effects of spatial proximity of the neighboring atomic wavefunctions.

$$\gamma = -\int d\mathbf{r} \phi^*(\mathbf{r}) \Delta U(\mathbf{r}) \phi(\mathbf{r} - \mathbf{R}) \tag{52}$$

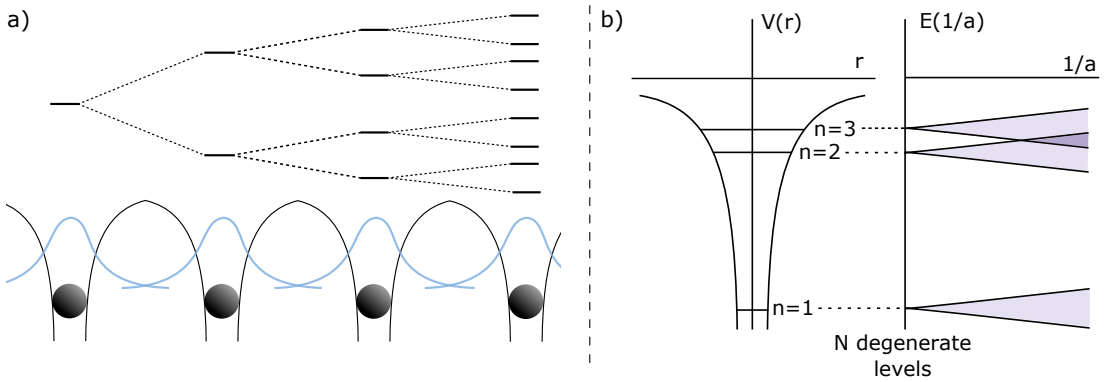

Figure 11: Energy splitting, from bonds to bands. a) Energy splitting for increasing number of atoms becoming bonded, eventually forming a band. b) Created from Fig 10.4 in Aschroft and Mermin Solid State Physics [1]. The degeneracy of N atomic levels is lifted as the overlap integral is increased.

For an N atom system Fig.11(b) shows the energy relation for different values of γ. If the overlap is small, then the system will resemble that of a single atomic potential with N degenerate levels. For increasing overlap, the degeneracy is lifted as the levels split. This splitting eventually forms continuous bands as the atoms are closer and have large overlap integrals. In general, the spatial extent of

a wavefunction increases with the energy of the atomic level. Correspondingly in a crystal, the bandwidths will increase with the mean band energy [1]. This is why the gap between bands decreases for crystals with the same structure but higher atomic energy levels – comparing diamond, silicon, and germanium, with band gaps of 5.5 eV, 1.14 eV and 0.6 eV respectively.

Solving for the exact band structure for silicon can be quite difficult, having to take into account at least 8 bands. Fig.12(a) shows the band structure calculated using a $\mathbf{k} \cdot \mathbf{p}$ method taken from [37]. For our purposes the exact band structure is not necessary, but certain features are important such as the magnitude and relative position of the silicon band gap. Fig.12(b) shows an STM I(V) spectroscopy, where the current is collected as the voltage is swept. From this curve we are able to resolve the valence band, the band gap, and the conduction band. The gap measured here is not the true gap size, as the signal is subject to TIBB.

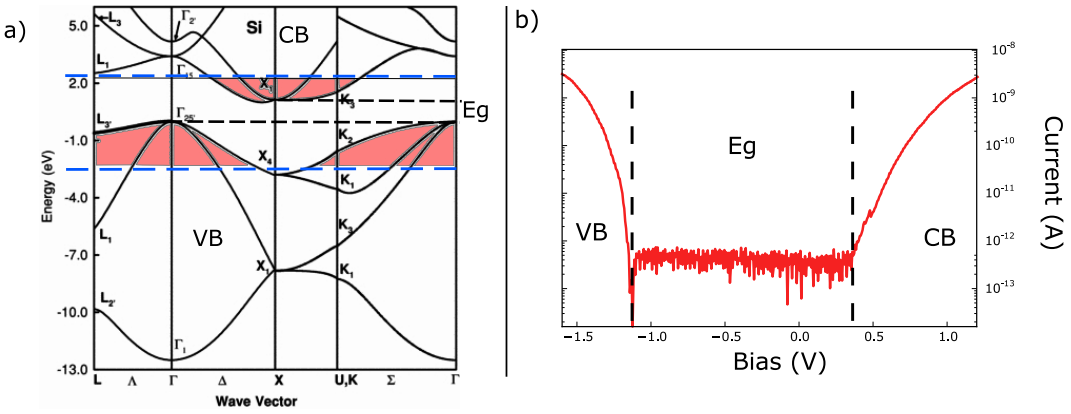

Figure 12: The Silicon Band Structure. a) Shows a calculated band structure of silicon taken from [37] with superimposed lines to denote the energy regime an STM typically probes. b) Shows an STM I(V) for the energies in the band diagram marked in red. This spectra is able to resolve the conduction band, the valence band, and the band gap.

The valence electrons of the silicon atom are localized in their bonds, such that there are no mobile charges on the native silicon crystal aside from thermally induced carriers. The Fermi level is placed inside the band gap such that the lower band is full – representing the valence band, and the upper bands are empty – representing the conduction band. The introduction of impurities with lesser or

fewer electrons will provide positive or negative carriers that facilitate currents. This is called doping, which will be addressed in the following section.

4.1.2 *Dopants*

Silicon is a well studied material and its preparation techniques are highly developed. The ability to introduce carriers with dopants into semiconducting materials is what makes them so versatile and valuable. A dopant is a defect atom that has one more, or one fewer electron than the host, called "donors" or "acceptors" respectively. The electronic effect of adding dopants is to shift the Fermi level. Materials with "donors" are called n-type because they have extra electrons, or negative carriers, and their Fermi level is shifted towards the conduction band. Conversely, materials with "acceptors" are called p-type because they have a deficit of electrons, or positive carriers, and their Fermi level is shifted towards the valence band. The main donor atoms used in silicon are from group V in the periodic table, namely: arsenic, phosphorous and antimony. Acceptor atoms in silicon come from group III and is typically boron.

The experiments presented in this thesis are done on degenerately doped $1x10^{19}/cm^3$ (3-4mOhm.cm) n-type arsenic doped samples. Degenerate doping means that the density of carriers is large enough that electrons can "hop" between sites, and their overlap is large enough to create a donor band [24]. This band is 50 meV under the silicon CB with the Fermi level placed in its center around 25 meV below the CB. This Fermi level has been theoretically predicted [17] and measured with infrared absorption [2]. A partially filled band means it has metallic like behavior - but in this case there are fewer and less mobile charges than in a true metal. Degenerate doping is an essential component for STM of semiconductors at low temperatures because it maintains the tunneling current where there are few thermal carriers. This is casually referred to as "freezing out“ the charge carriers whose ionization energies are on the order of 10s of meV [23]

The doping concentration, and subsequently the number and mobility of charges have an effect on the screening ability of the sample. A point charge in a solid full of carriers will obey a screened Poisson's equation, with the solution for the effective field:

$$E(\mathbf{r}) = \frac{Q}{r} e^{-k_0 r} \tag{53}$$

Where k_0 is the Thomas-Fermi wavevector which characterizes the damping of the field:

$$k_0^2 = 4\pi e^2 \frac{\partial n}{\partial \mu} \tag{54}$$

At low temperature it is related to the number of carriers n by [1]:

$$k_0^2 \approx a_o (\frac{4n\pi}{3})^{1/3} \tag{55}$$

As n increases so does the damping of the electric field from the point charge. This directly impacts the effects of TIBB, and the spatial extent of a charged entity on the surface such as a dangling bond.

4.2 SI(100)-H

Fig.13(a,b) shows schematics of the 2x1 reconstructed Si(100)-H surface from the side and top view. The surface atoms have rearranged to form dimer rows, and what would normally be an unsatisfied bond is capped with a hydrogen atom. An STM image of these dimer rows is featured in Fig.14, where we can see their orientations switch between surface layers.

4.2.1 *Sample Preparation*

The 2x1 reconstruction is done in UHV with controlled temperature and flux of H atoms. After degassing, the sample is flashed between 1050-1250°C several times

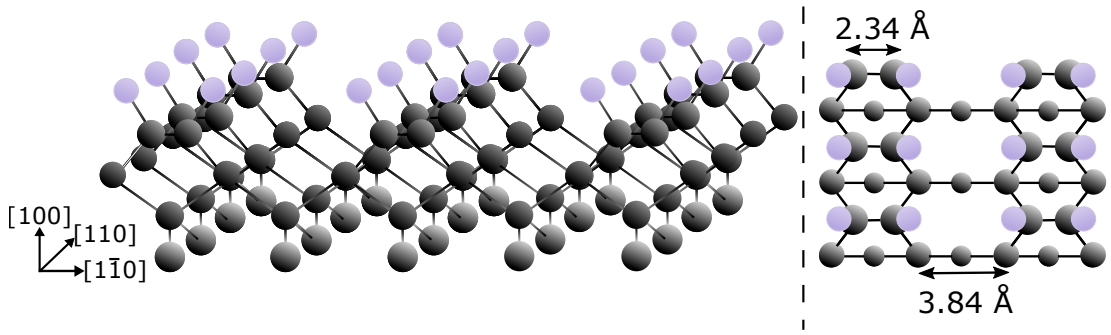

Figure 13: Schematic of the Si(100)-H surface. a) Shows the side view of the wafer and crystal orientations. b) Shows the dimer rows seen by the STM and the lower layer Si atoms.

to remove the protective oxide layer on the sample. The importance of this temperature range will be discussed in a subsequent section. The termination process begins after the final flash. First, hydrogen gas is leaked in to the chamber at $1x10^{-6}$ Torr, and a tungsten filament is heated to 1700°C that will crack the H_2 into atoms. The sample is left at room temperature under the flux of H atoms for 60 seconds which etches the first few surface layers. A final flash is done, and then the sample is brought down to 330°C for 30 seconds. During this time the surface reconstructs in to the 2x1 phase and the remaining unsatisfied bonds are capped with an H atom. Lower temperatures during this termination process will produce a 3x1 reconstruction.

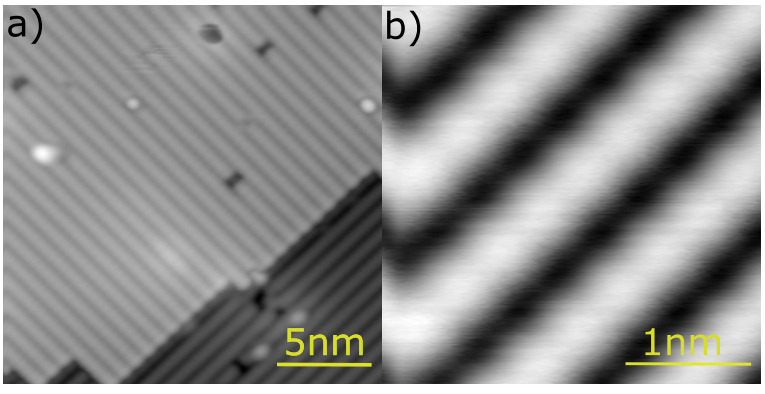

Figure 14: STM constant current images of the Si(100)-H surface. a) 20x20 nm image taken with a setpoint of -1.8 V and 30 pA. The dimer rows switch orientation for the lower surface layer. b) 3x3 nm image taken at -1.8 V and 30 pA.

4.2.2 *Metallic Surface States*

Hydrogen termination acts to satisfy the dangling bonds at the surface and significantly changes the electronic properties observed by STM. Fig.15(a) shows the bare 2x1 reconstructed surface. The unsatisfied bonds each carry an extra electron, and their proximity allows them to delocalize and exhibit metallic like character. These surface states are observed by the STM in the blue curve in Fig.15(c) that shows current in the band gap. The purple curve shows spectroscopy of the hydrogen terminated surface where the hydrogen atoms have capped the unsatisfied bonds, and the silicon band gap becomes visible.

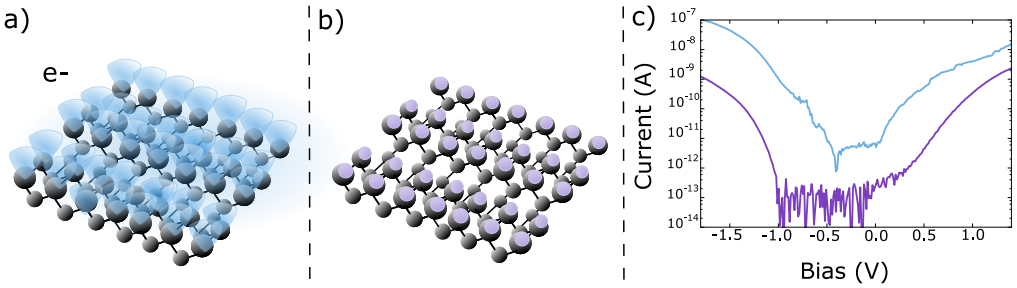

Figure 15: Observation of surface states. a) Schematic of the bare Si(100) surface whose unsatisfied bonds become delocalized. b) Schematic of the hydrogen terminated Si(100) whose bonds are satisfied. c) Compares the spectra of bare silicon in blue, and hydrogen terminated silicon in purple. The curves were taken at the same height set at -1.8 V and 30 pA over Si-H. The conduction in the gap for bare silicon is attributed to the surface states.

4.2.3 *Depletion region*

During sample preparation the annealing temperature is important because it causes the dopants to diffuse. It has been found that heating the sample to 1250°C will result in a depletion layer of about 150 nm as determined by Secondary Ion Mass Spectroscopy (SIMS) [26]. In this region the dopant density is estimated to be about 3 orders of magnitude lower [26] and falls below the criteria for degen-

eracy, causing the dopants to remain unionized. The characteristics of this surface depletion region can be seen in the I(V) spectroscopy. Fig.16 compares the I(V) spectra over a 1050°C in (a) and 1250°C in (b) flashed samples for decreasing tip and sample distance. What emerges at closer distances is a shoulder at negative bias in the gap for 1050°C which is absent on the 1250°C sample. This is indicative of the Fermi level shift and the dopant current. [26]. The donor band is easier to resolve at closer distances as the TIBB brings states from the CB below the donor band Fermi level. It is a helpful reminder at this point that the positive biases are probing the empty states of the sample while negative bias is probing its filled states.

4.3 SI(111)-H

Hydrogen termination of the Si(111) surface will create a 1x1 hexagonal reconstruction whose side and top view are shown schematically in Fig.17. The UHV process of hydrogen terminating the Si(111) surface is very similar to the Si(100), however the resulting surface is full of defects. Fig.18(a) is a 10x10 nm STM image capturing the three main types of defects. Owman et al [25] attributed each of them as a consequence of terminating the 7x7 bare Si(111) reconstructed surface. In reference to Fig.18(a) they are identified as follows: The triangles A are stacking faults; The bright protrusions B are hydrogen terminated silicon islands; And the small defects such as C are dangling bonds. There has yet to be a reported method of obtaining a defect free 1x1 reconstruction hydrogen terminated surface on the Si(111) crystal using the in-situ method. The types of surface defects depend greatly on both the termination temperatures 350-400°C and dosage 1000-5000 L where L is the unit of Langmuirs (10^{-8} Torr*100 seconds= 1 L)[25]. Fig.18.(b) shows a 5x5nm patch where we resolve the hexagonal hydrogen terminated surface. Work towards a defect free surface may be achievable through a wet chemical etch with NH_4F [32] where the challenge is to get the sample into UHV without contaminants.

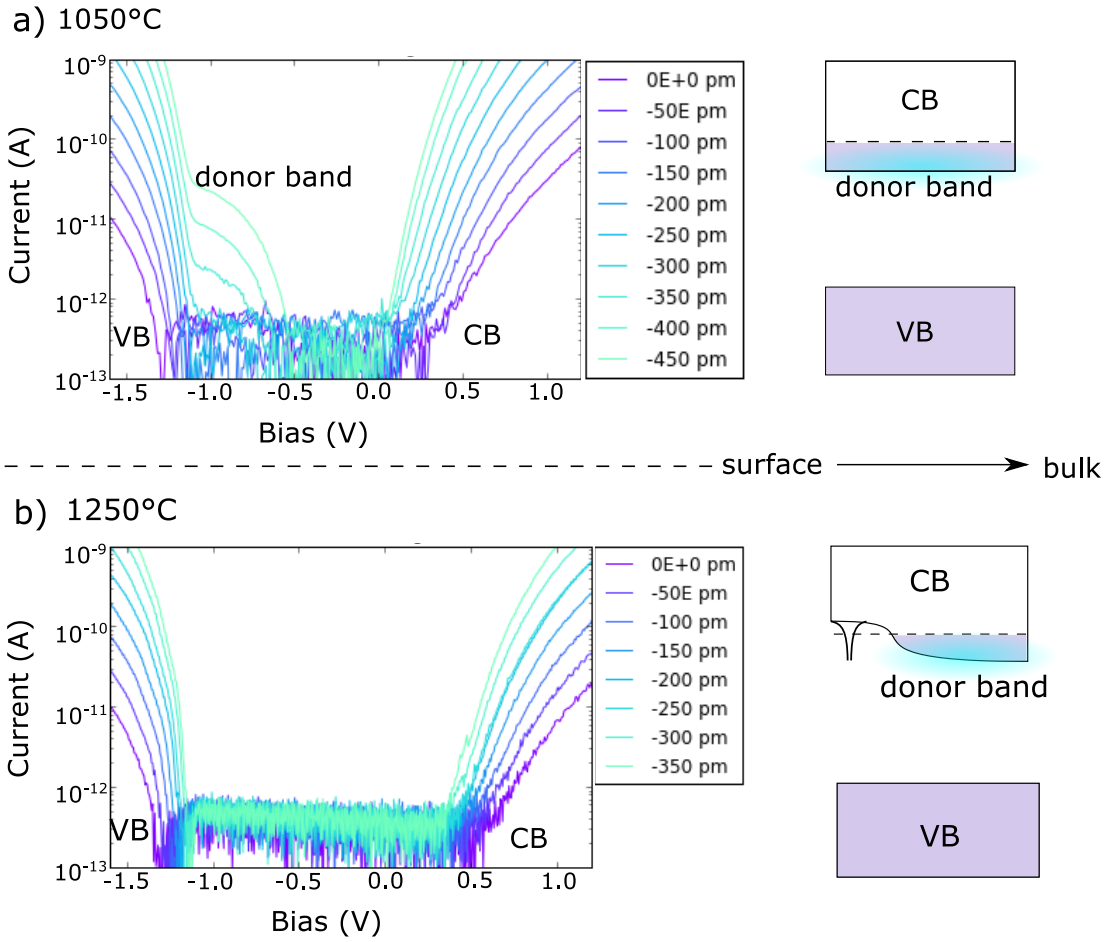

Figure 16: The depletion region, a comparison of spectra from 1050°C and 1250°C flashed samples. a) The 1050°C sample. I(V) spectra for decreasing tip-sample distance shows the emergence of the donor band featured in the schematic to the right. b) The 1250°C sample. I(V) spectra for decreasing tip-sample distance lacks the donor band, the schematic to the right shows the required ionization potential for the depleted surface region.

4.3.1 *Surface States*

The lack of periodicity from the defects creates extrinsic surface states. Fig.19 shows, for example, height spectra taken over Si-H at two different locations on the same sample. In one case there is a shoulder inside the gap, and the other there is not. Regions close together have similar I(V) character but cannot be compared to other regions. The local surface states are dependent on the surrounding

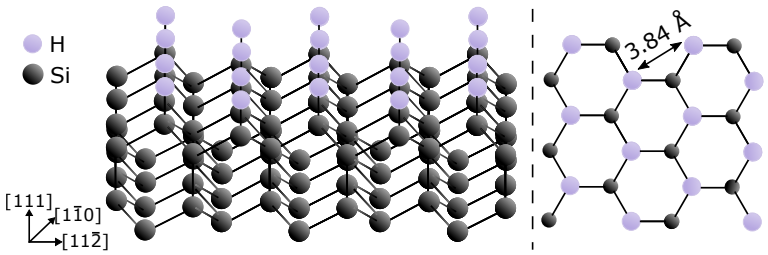

Figure 17: Schematic of the Si(111)-H surface. a) Shows the side view of the wafer and crystal orientations. b) Shows the hexagonal lattice seen by the STM and the lower layer Si atoms.

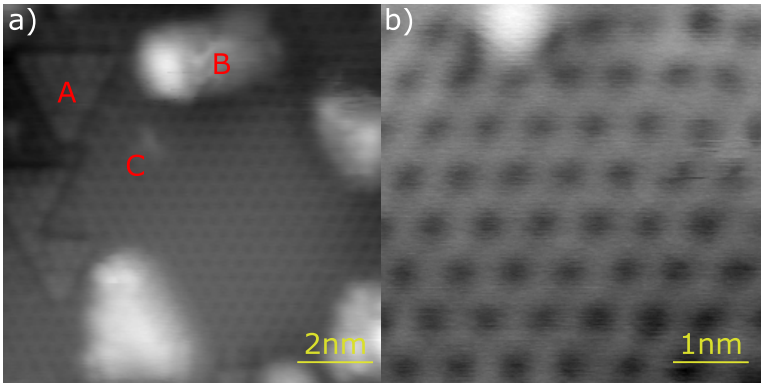

Figure 18: STM constant current images of the Si(111)-H surface prepared in-situ. a) 10x10 nm image taken with a set point of -1.8 V and 30 pA which shows the three common defects on this surface. A is a stacking fault, B is a terminated silicon island, and C is a dangling bond. b) 5x5 nm image taken at a set point of -1.8 V and 30 pA that shows the surfaces hexagonal structure.

defects and makes conclusions about the electronic properties difficult. For this reason we abstain from studies on this surface as we search for new methods to mitigate these effects.

4.3.2 *2x1 Reconstruction*

When an area of H is removed from the Si(111) surface it will reconstruct into a 2x1 pattern. This reconstruction is believed to be very conductive through the formation of long π-bonded chains [11]. Desorption in large patches can be done by subjecting the atoms to a high field from the tip, a set point of 4 V and 150

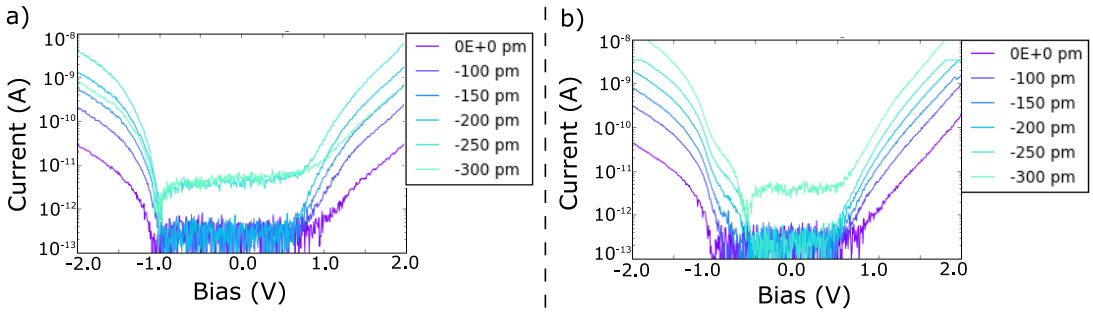

Figure 19: Local extrinsic surface states on the Si(111)-H UHV sample. a) Shows an expected I(V) curve over Si-H resolving the band gap. b) Shows I(V) over Si-H on the same sample but in a different region. A shoulder appears at negative bias that is believed to be from surface states.

pA is usually sufficient. The red arrows in Fig.20(a) show the three possible directions the 2x1 lines can take. For future study would be to see at what the scale the chains will reproducibly point in the same direction, and if this process is affected by local surface defects. Fig.20(b) shows a 10x10 nm patch whose rows are all orientated the same way. A possible application would be to have 2x1 wires connecting components on a surface.

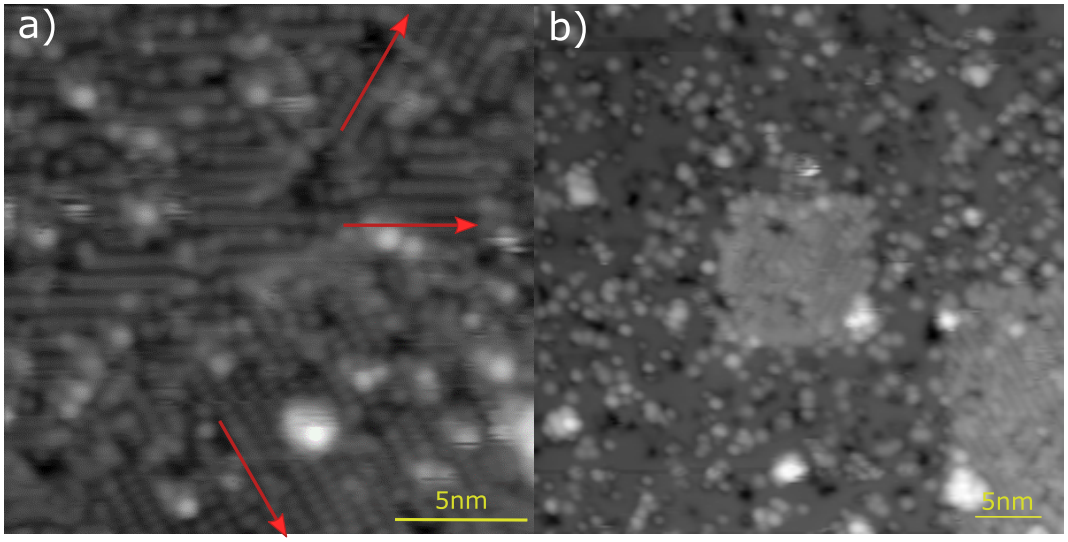

Figure 20: The 2 x 1 reconstructed Si(111) surface upon desorption of Hydrogen. a) 20 x 20 nm image with a setpoint of -2 V and 50 pA shows the three possible orientations of the reconstruction b) 40 x 40 nm image with a setpoint of -2 V and 50 pA shows a small 10 x 10 nm patch whose reconstructions are all in the same direction.

5

DANGLING BONDS

Dangling Bonds (DBs) are the focal point of this thesis, and of the research in our group. The semiconductor industry views them as defects while our atomic scale device group sees them as a platform for both scientific and technological interest. A DB exists at a silicon atom that is missing a capping H atom, leaving behind an empty orbital. They occur both natively on the hydrogen terminated surface and can be created with the tip by applying a voltage pulse, around 2 V, that supplies enough energy to break the Si-H bond.

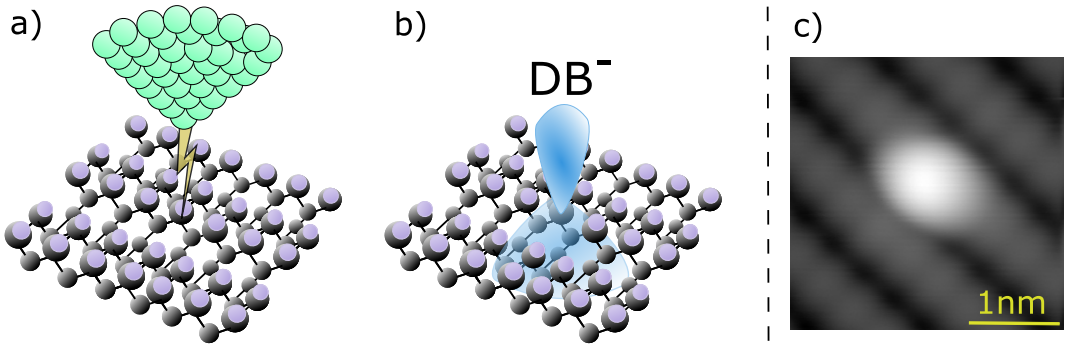

Figure 21: Dangling Bond Fabrication. a) The tip is brought on top of a hydrogen atom and a positive voltage pulse, around 2 V is applied between the tip and sample. b) The Si-H bond is broken, leaving behind a dangling bond from the underlying silicon atom. This DB natively has a negative charge on the n-type silicon surface. c) A 3 x 3 nm empty state image of a DB

Unlike on the bare silicon surface, a single DB cannot delocalize to form a surface band. Instead it remains as a single localized level which is energetically inside the band gap. Due to its energetic position it is sometimes referred to as a mid gap state or a deep level because it is isolated from the bulk states and has a greater ionization energy relative to a shallow donor. This feature makes them accessible for probes, and a promising candidate for atomic scale devices

such as Quantum Cellular Automata [9] or silicon based qubits [21]. This Chapter will review basic concepts around DBs, and the novel ways we have learned to characterize them.

5.1 BASIC PROPERTIES

An important feature of the DB is that it can be occupied by up to two electrons, allowing three possible charge states. An empty DB leaves the host silicon atom as a net positive, a singly occupied DB as neutral, and a doubly occupied DB as negative. What is shown schematically in Fig.22(a) are the transition levels (+/0) and (0/-) denoting the amount of energy required to add the first, and second electron respectively [35]. Deep Level Transient Spectroscopy of defects at an $Si - SiO_2$ interface show the position of the (0/-) level to be 0.25 eV below the conduction band, and the (+/0) level to be 0.3 eV above the valence band – we take these to be the approximate positions of the DB levels [16]. The energy difference between these transition levels is around 0.6 eV and represents the on-site Coulombic repulsion, U, felt by the second electron from the first. The presence of a state within the bandgap implies that current can be drawn through it where it otherwise couldn't with an STM tip over Si-H. Indeed this is shown in the I(V) curves in Fig.22.(b) for a DB on Si(100)-H. At positive bias in the CB, the curves are very similar. Negative bias probes the gap and the VB, and the curve over the DB shows current in the gap region where the Si-H does not. The DB is acting as a stepping stone from the bulk through surface to the tip. At these energies, a Negative Differential Resistance (NDR) feature is observed. This is when an increase in voltage has a corresponding decrease in current and is characteristic of the different conduction pathways through a DB. This feature will be focused on later in this chapter.

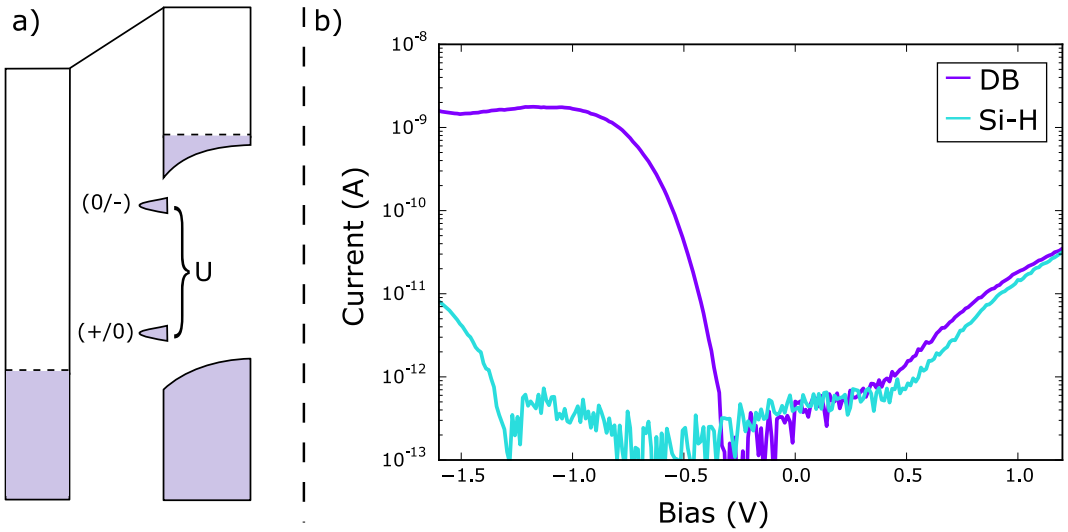

Figure 22: Energy Diagram and Spectroscopy of a Dangling bond. a) Schematically shows the energetic placement of the transition levels in the band gap of silicon. The (+/0) transition level describes the amount of energy to put a single on the DB changing its charge state from positive to neutral. The (0/-) level denotes the energy to put a second electron on the DB, changing its charge state from neutral to negative. The spacing between these levels is the coulomb repulsion between the electrons. b) A comparative spectroscopy of Si-H and a DB for the same height set point. For voltages representative of the band gap there is conduction through a DB but not Si-H.

5.1.1 *Broadening and Rates*

The DB is a single state interfacing with a continuum of states. This leads to an energetic broadening which is schematically visualized in the band diagrams with the levels occupying a small range of energy. The amount of current that can go through a single state is limited by the coupling strength between it and its reservoir. The parameter that quantifies coupling is defined by the transfer rate $\gamma = \hbar\Gamma$, where Γ contains the details of both overlap and electron transport, ultimately defined by the tunneling matrices in Eq.38. The inflows and outflows from a single

level into two contacts is shown schematically in Fig.23.(a) and the current can be described by:

$$I = \frac{q}{\hbar}\frac{\gamma_1\gamma_2}{\gamma_1+\gamma_2}[f_1(E) - f_2(E)] \tag{56}$$

Larger coupling will increase the transfer rate, and simultaneously broaden the level. It can be thought of as the bulk states "spreading" into the channel, and the single state will equivalently mix part of its state to the bulk. This mixing of the single state to the bulk can only occur at one energy $f(E)$, while the "spread" from the bulk into the channel can occur from a continuum of states N - effectively broadening single level due to its interaction with the bulk [34]. While the level can have any shape it is usually described in terms of a Lorentzian. By setting $\gamma_1 = \gamma_2$ we can visualize the broadening with the following equation:

$$D(E) = \frac{1}{2\pi}\frac{\gamma}{(E)^2 + (\gamma/2)^2} \tag{57}$$

Where $D(E)$ is the density of states at energy E. Importantly, it remains true that an integration over the full energy range of the level will result in an occupation of a single electron. Fig.23.(b) shows the extent of broadening for several values of γ. The coupling is related to the emptying and filling rates for a DB which can be measured. For negative bias, the pathways for emptying and filling the transition levels are shown in Fig.23(c) and will depend on relative band bending, carriers, and tip height. These rates will be explored in this chapter and their connection to NDR. Further, they are relevant parameters to know for device applications since they govern the charge dynamics.

5.1.2 *Imaging*

Spectroscopy reveals information about the electronic properties of a single point and images reveal their spatial dependence. The orbital of a DB extends in 3D both into vacuum and into the surface where its shape is highly dependent on the local reconstruction and its own occupation. Methods such as Density Function Theory can be used to simulate the shape of the wavefunction. Fig.24 shows two different

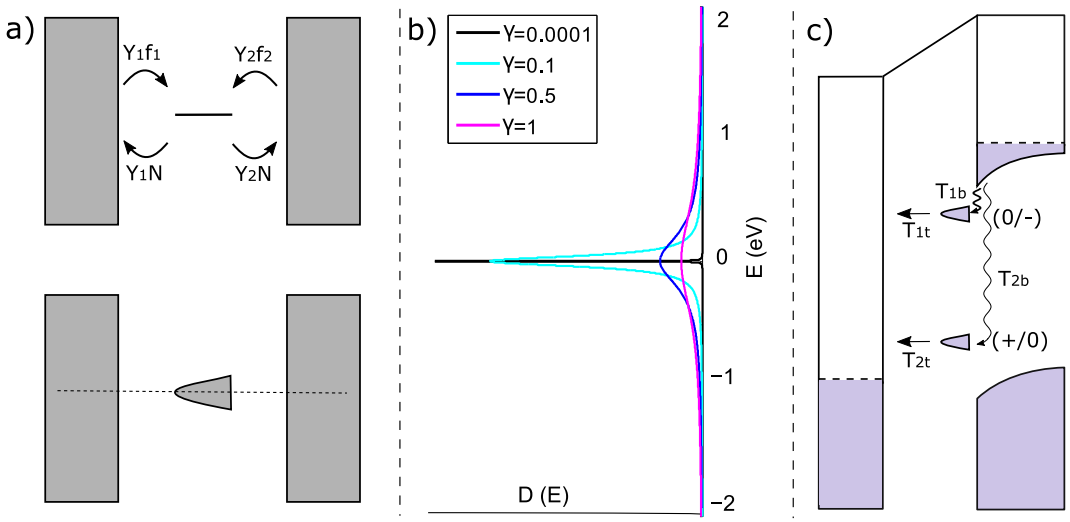

Figure 23: Level Broadening and Interactions with the Bulk a) Shows a schematic of the coupling into and out of a single level which determine the filling and emptying rates. Inflow can occur at one single level, while the outflow goes into a continuum. The lower figure shows a schematic of a broadened level after bulk interactions. b) A Lorentzian function plotted for increasing broadening parameter γ. For small values it approaches a delta function, and larger values approach a line. c) The relevant rates for a DB interacting with the tip and sample.

imaging regimes for both a DB on the Si(111)-H and Si(100)-H surfaces at constant current. The first is filled state imaging where the fermi level of the tip is below that of silicon and we receive current through the (0/-) or the (+/0) level. The second is empty state imaging where the fermi level of tip is above that of silicon. In this regime the DB is always doubly occupied and we are able to image a halo around the DB that is representative of its wavefunction [35]. What becomes evident for the DB on the Si(111)-H surface is that it appears more isotropic. The wavefunction of a DB on the Si(100)-H surface will also flip depending on which side of the dimer row its on. The symmetry of the DB on the Si(111)-H surface makes it a more desirable candidate for atomic scale devices because it removes several variables needed to work around in both geometry and electronic properties. Although this is true, a clean degenerately doped Si(111)-H that is compatible with 4 K STM is

difficult to achieve. The rest of this chapter will be concerned with characterizing DBs on the Si(100)-H surface at negative bias.

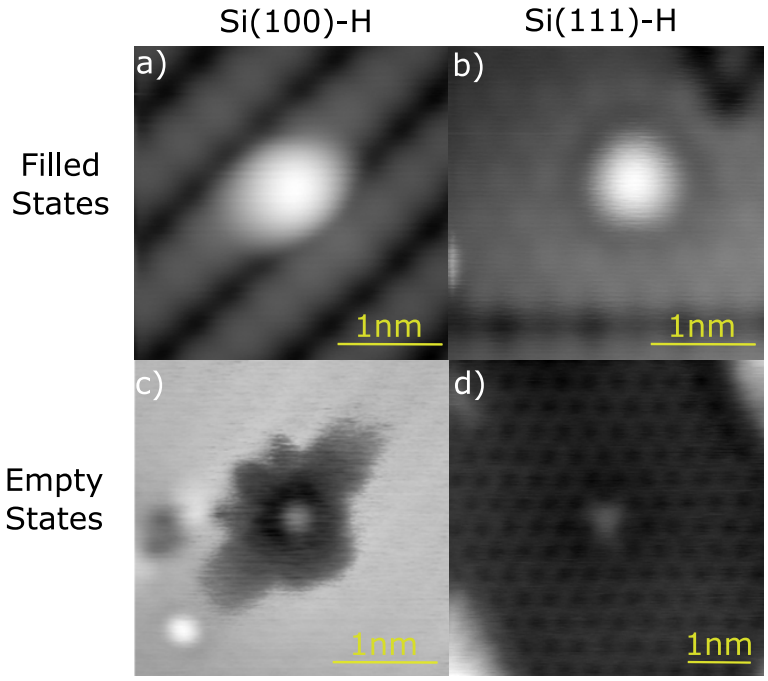

Figure 24: Filled and empty states constant current images of DBs on the Si(100)-H and Si(111)-H surfaces. a) 3x3 nm filled state image of DB on Si(100)-H with set point of -1.8 V and 30 pA. b) 3x3 nm filled state image of DB on Si(111)-H with set point of -1.8 V and 30 pA. c) 3x3 nm empty state image of DB on Si(100)-H with set point of 1.4 V and 50 pA. d) 5x5 nm empty state image of DB on Si(111)-H with set point of 2 V and 30 pA.

5.1.3 *1250°C and 1050°C Spectroscopy*

The depletion region mentioned in Ch.4 has important implications on the spectroscopy of DBs which can influence and be influenced by dopants. For a 1250°C sample, the depletion region implies a sparse distribution of dopants at the surface whose carriers are released upon ionization. It has been shown by Rashidi et al [28] that while probing a DB, a nearby isolated dopant can ionize and cause an abrupt change in the I(V) curves, like an "on" switch. The energy and the strength of the ionization event varies with the proximity of the DB to the dopant. These

interactions cause the spectroscopy of DBs on a 1250°C sample at negative bias to be far from uniform. With this in mind we can be selective with the DBs we choose to study. For the DBs described in this thesis there are no recognizable ionization events, and the main implication of a 1250°C sample is the lack of charge carriers compared to a 1050°C sample. A 1050°C sample remains degenerate and there is uniform spectroscopy over different DBs. The degeneracy also implies a shorter range for charge effects such as band bending and screening.

5.2 NEGATIVE DIFFERENTIAL RESISTANCE

Empty state spectra of DBs reveal an NDR feature which has been explored by Rashidi et al [27]. We understand this feature as in terms of the transfer of charge between the (+/0) and (0/-) transition levels, and their occupation probabilities. The observed tunneling current I_T is a summation of the contributions from each level:

$$I_T = I_{(+/0)} + I_{(0/-)} \tag{58}$$

Where the amount of current that can be drawn through a level is limited by the emptying or filling rate as pictured in Fig.23(c). The filling rates T_{1b} and T_{2b} are influenced by the number of carriers and the relative band bending from the tip or any nearby charge. The emptying rates T_{1t} and T_{2t} will depend most strongly on the spatial overlap with the DB, both in tip sample distance z and laterally. An analysis of the delicate balance of rates and their relation to NDR will be explained in detail and is featured in the supplementary of [27].

5.2.1 *DC Measurements and Model*

The curves in Fig.25(a) show a DB on a 1050 sample at negative bias for different heights. The tip begins with a 0 pm offset and is incrementally brought 210 pm towards the sample. For spectra further away, the NDR is absent and becomes

more prominent as the tip is brought closer. We will divide the NDR curve into 4 different regimes and describe the current in terms of the conduction pathways through the DB. The magnitude of the current depends on the supply of electrons, and which process in Fig.23(c) is rate limiting.

We will start at 0 bias and sweep to more negative bias. The first section is the onset of the current, where the tip is brought below the (0/-) level and can receive current from the CB through the doubly occupied state. This onset shifts to lower bias as the tip is moved closer due to TIBB, as seen more clearly in the log plot inset on Fig.25(a). The second section is the rise and peak of the current before NDR. In this case the Fermi level is above the (+/0) level and below the (0/-) level. This means the DB will be occupied by at least one electron and the current is flowing only through the (0/-) level. The total current will be related to the emptying rate of the tip and the filling rate from the bulk:

$$I_T = I_{(0/-)} = e\frac{\Gamma_{1b}\Gamma_{1t}}{\Gamma_{1b}+\Gamma_{1t}} \tag{59}$$

where all rates are related to their respective time constants by $\Gamma = 1/T$. From far away the rate limiting process is the emptying rate from the (0/-) level to the tip Γ_{1t}. As the tip moves closer, the overlap between the tip and DB wavefunctions increases and Γ_{1t} with it. This means that the height of the peak will grow as it can draw more current but eventually it will saturate. At this point the bulk cannot supply more current and $\Gamma_{1t} > \Gamma_{1b}$. This saturation current allows us to infer the filling rate of the bulk to (0/-) level Γ_{1b}.

The third section is the NDR regime. Here, the tip Fermi level is swept below the (+/0) level introducing a second conduction pathway through the DB. The (0/-) and (+/0) states cannot exist simultaneously, because the DB cannot be both singly and doubly occupied at the same time This distinction is important because the singly occupied state is approximately 0.6 eV lower in energy. Filling this level from the bulk must occur from the CB through a highly inelastic process. The resulting rate Γ_{2b}, is much slower than Γ_{1b}. The total current is:

$$I_T = I_{(+/0)} + I_{(0/-)} \tag{60}$$

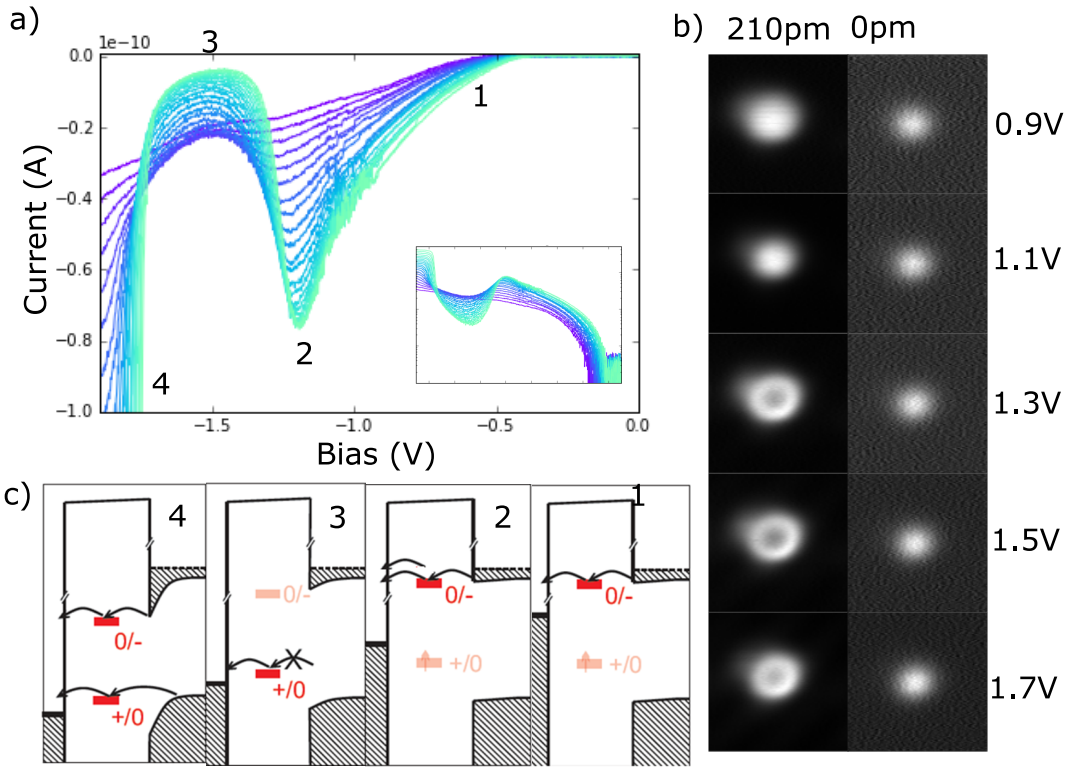

Figure 25: Negative Differential Resistance DC measurements and Model. a) Empty states spectra for decreasing tip sample distance, starting from 0 pm in purple and going to 210 pm in cyan in 10 pm increments The NDR peak grows as the tip is moved closer and eventually saturates. The inset features a log plot. b) Constant height images for the DB at 0 pm and 210 pm offsets which show the "donut" feature that appears in the NDR regime. Where the overlap is strong in the center, the tip is able to fully empty the DB. As the tip moves laterally is the overlap decreases and is not able to fully empty the DB. c) The 4 tunneling regimes in filled state spectroscopy. 1- The tip is swept below the (0/-) level and the tip begins to draw current. 2- The tip contunues to lower drawing more current. If the tip emptying rate is fast enough, then the current may saturate as the bulk supply is limited by $T_1 b$. 3- The tip is swept below the (+/0) and can fully empty the DB. This causes the NDR feature as the current because rate limited by the slower filling rate $T_2 b$. 4- The tip is swept lower, and tibb brings the (+/0) into resonance with the valence band so it will always be full, and the collected current is no longer limited by $T_2 b$.

We look to find an expression for each current contribution. In this regime there is a finite probability the DB will either be positive, neutral or negative. This can

be described using a probability vector $\mathbf{P} = \left(P^+, P^0, P^-\right)^T$ whose elements sum to unity. Since we are interested in the current, we want to look at the time dependent change in occupation. The probability vector will satisfy the differential equation $\dot{\mathbf{P}} = \mathbb{M}\mathbf{P}$. We can populate the matrix elements by considering the rates that would influence a transition, where each element will be the flux into minus the flux out of that state. Ruling out the direct transition from a positive to negative charge state the matrix $\mathbb{M}$ is given by:

$$\mathbb{M} = \begin{bmatrix} -\Gamma_{2b} & \Gamma_{2t} & 0 \\ \Gamma_{2b} & -(\Gamma_{1b} + \Gamma_{2t}) & \Gamma_{1t} \\ 0 & \Gamma_{1b} & -\Gamma_{1t} \end{bmatrix}$$

Our DC I(V) measurements are the steady state solution which corresponds to the 0 eigenvalue:

$$\mathbf{P}_{ss} = \frac{1}{\Gamma_{1t}\Gamma_{2t} + \Gamma_{1t}\Gamma_{2b} + \Gamma_{1t}\Gamma_{2b}} \begin{bmatrix} \Gamma_{1t}\Gamma_{2t} \\ \Gamma_{1t}\Gamma_{2b} \\ \Gamma_{1b}\Gamma_{2b} \end{bmatrix}$$

Where the probability for each state is defined in terms of the relevant rates. We use these steady state values to decompose the tunneling current by taking the product of the probability of a state and its emptying rate:

$$I_{(+/0)} = eP^0\Gamma_{2t} = e\frac{\Gamma_{1t}\Gamma_{2t}\Gamma_{2b}}{\Gamma_{1t}\Gamma_{2t} + \Gamma_{1t}\Gamma_{2b} + \Gamma_{1b}\Gamma_{2b}} \tag{61}$$

and

$$I_{(0/-)} = eP^-\Gamma_{1t} = e\frac{\Gamma_{1b}\Gamma_{1t}}{\Gamma_{1b} + \Gamma_{1t} + \frac{\Gamma_{1t}\Gamma_{2t}}{\Gamma_{2b}}} \tag{62}$$

The $I_{(0/-)}$ level is written in this form to contrast it with Eq.59 where we see there is an extra term in the denominator that grows with decreasing Γ_{2b}. From far away, the occupation of the DB is on average more than 1 because the filling rate from the bulk is fast enough to supply electrons before the tip takes them away. As the tip

is moved closer, the emptying rate from the (+/0) level will increase. Eventually it will exceed the filling rate, $\Gamma_{2t} > \Gamma_{2b}$. At this point the current contributions from each level are limited by Γ_{2b} and the occupation of the DB is on average less than 1. The current will tend to 0 as the average occupation of the DB tends to 0. This process was modeled using Non-equilibrium Green's functions which can be reviewed in [27].

The figures shown in Fig.25(b) are constant height images for different biases. At far tip-sample distances the DB looks like a bright circular protrusion. When the tip is brought in 210 pm towards the surface, the images begin to show a donut shape for voltages in the NDR regime. The overlap of the tip and sample has a spatial dependence that influences the emptying rates. The darkening center of the DB is indicative of the NDR regime where the tip sample overlap is high. This overlap decreases as the tip is moved away from the center of the DB, decreasing the emptying rate Γ_{2t}, and ceases to trigger NDR.

The fourth section is the onset of the VB. Here the tip will is swept below the VB edge and resonant tunneling can occur. The final section of this chapter will probe this onset and the (+/0) charge transition.

5.2.2 *Time Resolved Measurements*

The NDR feature is a balance between the different emptying and filling rates to and from the DB. This section will show time resolved measurements that allow us to calculate the rates in Fig.23(c). The setup is shown in Fig.26(a). A channel from the signal generator is connected to the tip and the bias on the sample is set to 0. The signal generator will output a series of voltage pulses whose parameters such as frequency, width, and height can be tuned. Using this we are able to chop up the DC signal into pulses and resolve features that occur on the timescale of the pulse. Each pulse probes the system at the pulse height and collects the corresponding current. Processes slower than the pulse will not be resolved. The measured current is an average over many pulse series due to bandwidth of the

preamplifier. Since the DC bias is set to 0 for these measurements we can find the current due to the pulses I_{probe} by normalizing the measured current $I_{measured}$ with the duty cycle D:

$$I_{probe} = \frac{I_{measured}}{D} = \frac{P}{W} I_{measured} \tag{63}$$

Where P is the period of the pulse series, and W is the width of the pulses. The duty cycle is a ratio of how long the signal is "on" compared to "off". For time resolved IV measurements the pulse widths are kept constant while their height V is swept. The result is the series of time resolved I(V) curves as shown in Fig.26(b), each corresponding to a different pulse length.

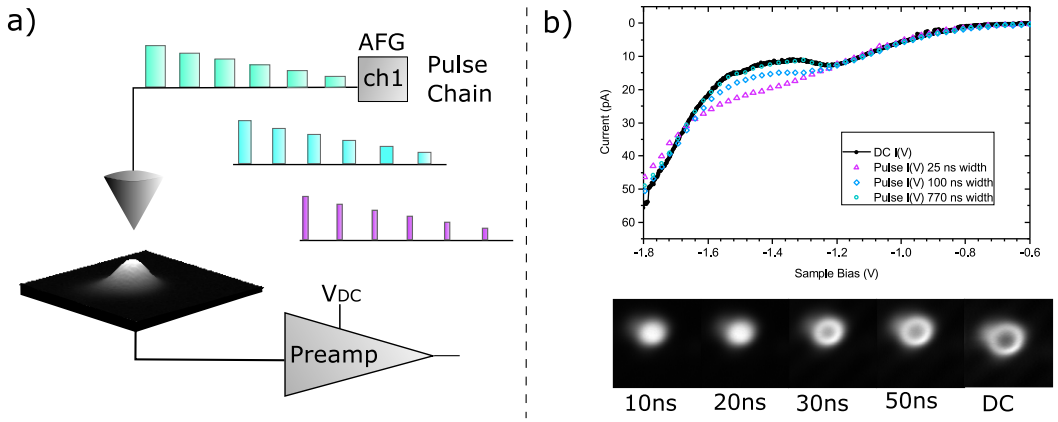

Figure 26: Time Resolved Measurements of NDR. a) Shows a schematic of the setup. The tip is connected to one channel of the signal generator which feeds in pulses while the DC bias is set to 0. b) Time resolved I(V) curves. The pulse height is swept for each pulse width. For small pulse widths the NDR feature gets extinguished. c) Time resolved 3 x 3 nm images for increasing pulse width, and pulse height set to -1.5 V

For longer pulses around 770 ns, the DC I(V) curve is replicated and for shorter pulses the NDR feature is extinguished. This is because the short pulses are not long enough to empty the (+/0) level, and conduction occurs mainly through the (0/-) level. By doing many measurements for increasing pulse lengths we observe an exponential decay in the current and can extract a time constant for a given voltage. This time constant measures the emptying rate of the (+/0) level to the

tip, T_{2t}. Assuming that the current form the $I_{(+/0)}$ level is small, we can find an expression for T_{2b} from Eq.61:

$$T_{2b} = \frac{e - I_{DC}T_{1b}}{I_{DC}T_{1b}}T_{2t} \tag{64}$$

If T_{1b} is found from the saturation current then we can calculate T_{2b}. This has been done for several different biases as shown in Fig.27(c) by Rashidi which is featured in [27].

Time resolved images are shown in Fig.26(c). These are taken in a similar way to the time resolved I(V) curves. The pulse series is kept at a set height $Vpulse = 1.5$ V, and the tip is rastered over the surface. Each pixel is the average current of many pulse series, which resolves features on the time scale of the individual pulse widths. A scan of a full plane will give a spatial time slice of the DB. The images in Fig.26(c) show time slices from 10 to 50 ns. As expected, the short time scales are more conductive, and for longer pulses the NDR donut appears and matches the DC image. The table in Fig.28 shows images of the emerging NDR

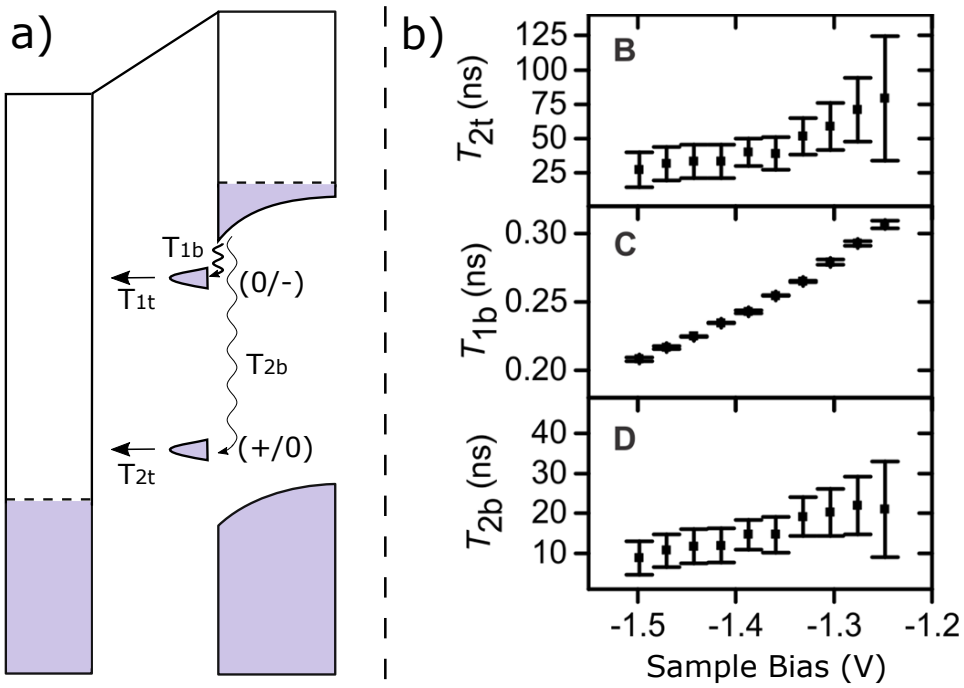

Figure 27: Emptying and Filling rates. a) A schematic of the emptying and filling rates of the two transition levels. b) Rates measured and calculated by Rashidi et al featured in [27].

feature as a function of both tip-sample separation and pulse width.

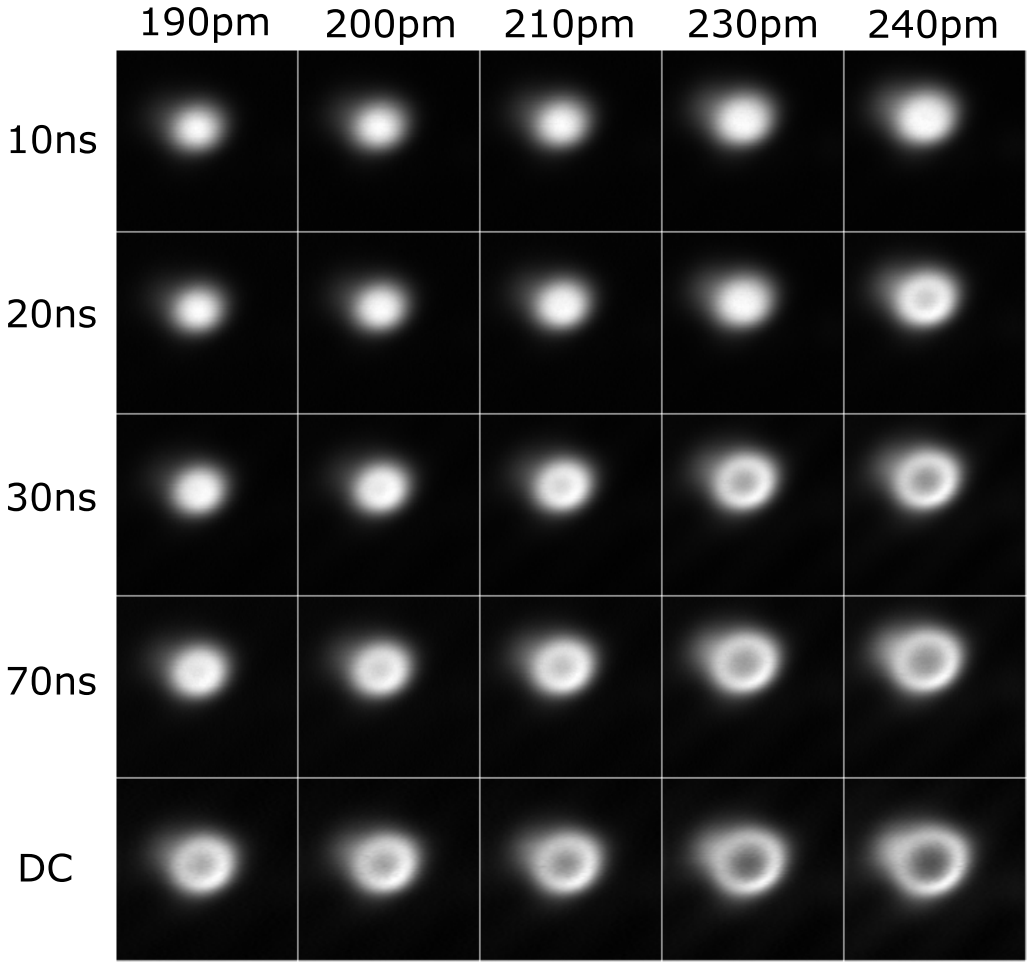

Figure 28: NDR Images. This figure summarizes the effects that approaching the surface Z (horizontal axis) and pulse width (vertical axis) have on the spatial imaging of NDR. For both small pulses and larger tip sample distance the DB appears as a circle. As either the pulse widths increase or tip sample distance decreases the circle begins to turn into the donut signature of NDR.

5.2.3 *Room temperature and 77 K*

The NDR feature is also observed at room temperature and 77 K which verifies the model as a thermally independent process. It does have an effect on the electron capture rate which becomes too fast for the bandwidth of our system to resolve.

This is likely due to the increase of thermal carriers. This effect is also seen in the I(V) curves as the tip is moved closer - the current peak does not saturate, and the current does not tend to zero.

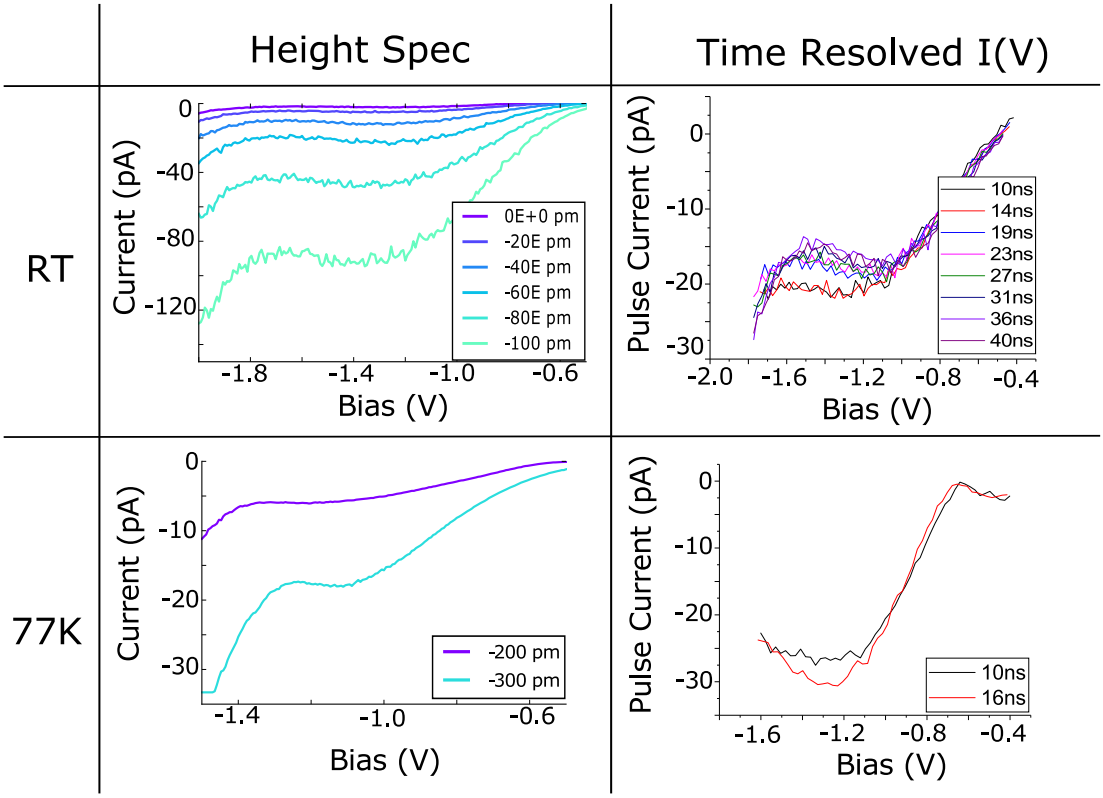

Figure 29: NDR at 300 and 77 K. The feature is still observed for the shortest pulse widths meaning that the time constants involved are too fast for us to resolve.

5.2.4 *NDR on a 1250°C Flashed Sample*

The results in the previous section were for DBs on a 1050 sample. NDR is also found on 1250°C samples, however the exact shape of the curve tends to vary. While control over the shape of the NDR will be saved for Ch7, a small comparison between the 1050 and 1250 curves will be made to illustrate the main differences between DBs on these samples. Fig.30 shows height spectra of over the DB. It is shown that for a given height set point, the NDR feature is always present, and the influence of moving closer is much less dramatic since Γ_{2t} is always fast enough.

This is because the lack of carriers of the 1250°C samples makes both filling rates from bulk Γ_{1b} and Γ_{2b} slower. Of consequence the current is easily saturated, and in the NDR region the occupation is close to 0. Time constants measured on 1250°C samples are on the order of μs, suggesting that we can tune these rates with doping level.

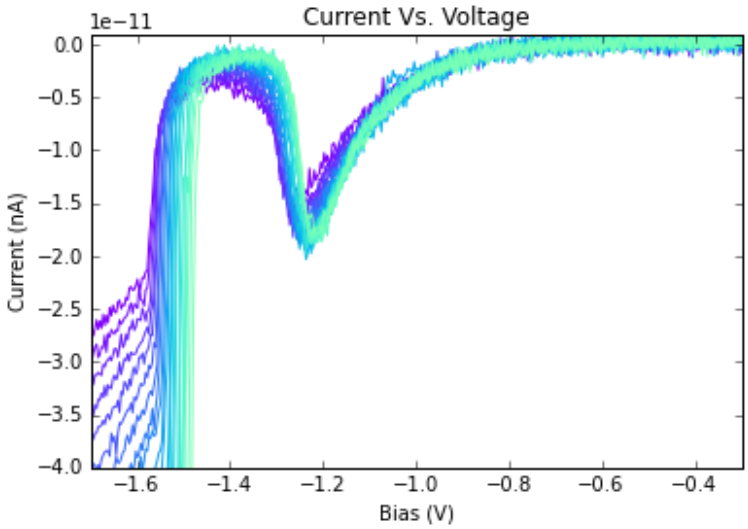

Figure 30: NDR on a 1250°C sample with the tip moving in. The current is easily saturated and the occupation in the NDR region tends to 0.

5.3 VALENCE BAND ONSET

What was not discussed in the previous section was the fourth regime, namely the onset of the valence band. Here, the the Fermi level is swept below the (+/0) level and in resonance with the valence band. There is a sharp current drop as the bulk states start to fill the tip states. For some voltage, due to TIBB, the (+/0) will also be swept into resonance with the VB where now it can be filled with a new process T_{2vb} shown in Fig.31(c). On a 1250°C sample we have been able to measure and image this threshold using a pump probe technique. The setup and premise are shown in Fig.31(a). A DC bias is applied corresponding to an energy in the NDR region where the (+/0) transition level is being emptied by the tip. A pulse is applied that pumps the system to an energy where the (+/0) can be filled

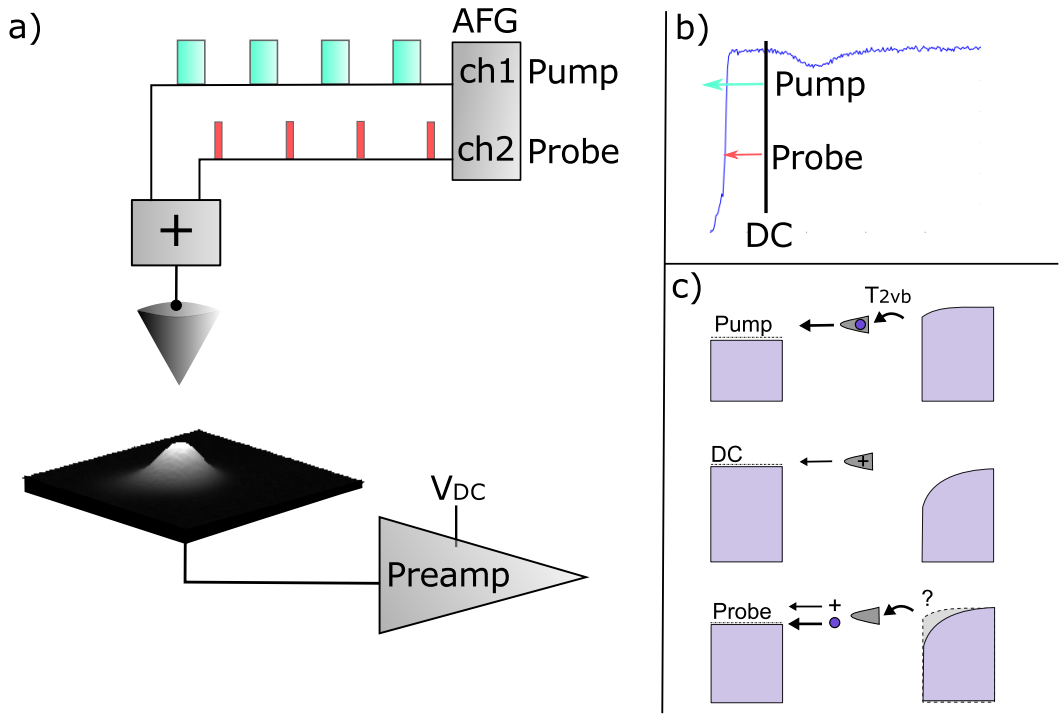

Figure 31: Probing the Valence Band Onset. a) Experimental setup, the channels of the signal generator are summed and then connected to the tip. Channel one is labeled as the pump pulse and channel two is the probe pulse. The DC bias is set to a voltage in the NDR regime b) A plot that shows an NDR curve and the corresponding pump, probe and DC biases. The pump pulses the system past the VB onset, the probe checks the VB onset, and the DC bias is set in the NDR regime. c) Energy schematics of the VB onset and the DB. The pump pulse allows the DB to be filled by the VB, the DC bias will empty the DB, and the pump will check if the DB is singly occupied or not. If the DB is fully empty then the positive charge will result in downward band bending and the probe will receive less current than if the DB was singly occupied.

by the valence band. A probe pulse is sent at the VB edge to measure the state of the system and will receive less current if the level is empty due to TIBB. To extract the probe current we run two experiments – one with both the pump and probe, and another with only the probe. Subtracting the two measured currents will give us the probe current, see Fig.32. Similar to the previous section, the pump probe experiment can be done at multiple points and be stitched together to make

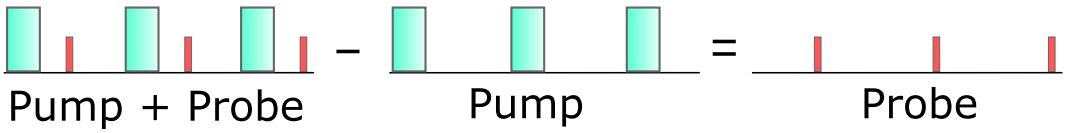

Figure 32: a) A schematic of the probe current extraction from a pump probe experiment. Two experiments are run, one with both the pump and probe on, and another with only the pump. Subtracting the two currents will give you the current from the probe.

images. Each image corresponds to a time slice that visually displays the dynamics of the hole created at the VB edge.

5.3.1 *Filling Rate*

Measurements for filling time T_{2vb} are outlined schematically in Fig.33(a and d) where we fix all parameters except the pump width. For short pump widths the VB will not have enough time to fill the (+/o) level leaving the charge state positive. In this case the probe will measure less current due to the band bending caused by the presence of this positive charge. Conversely, for long pump widths the VB will have enough time to fill the (+/o) and the probe will measure a larger current. The relative delay between pump and probe pulses must be constant and smaller than the emptying time of the tip. For the results in Fig.33(c) we set the relative delay to 10 ns, the DC bias to -1.3 V, the probe amplitude to -0.18 V and the period to 50 μs. By sweeping the pump width we observe an exponential rise in probe current from which we extract the filling rate of the valence band to the (+/o) level. For a pump amplitude of -0.2 V we measure $T_{2vb} = 1.66$ μs. As expected, this rate will increase with pump amplitude as shown in the inset of Fig.33(c). The images featured in Fig.33(b) are for a pump amplitude of -0.4 V.

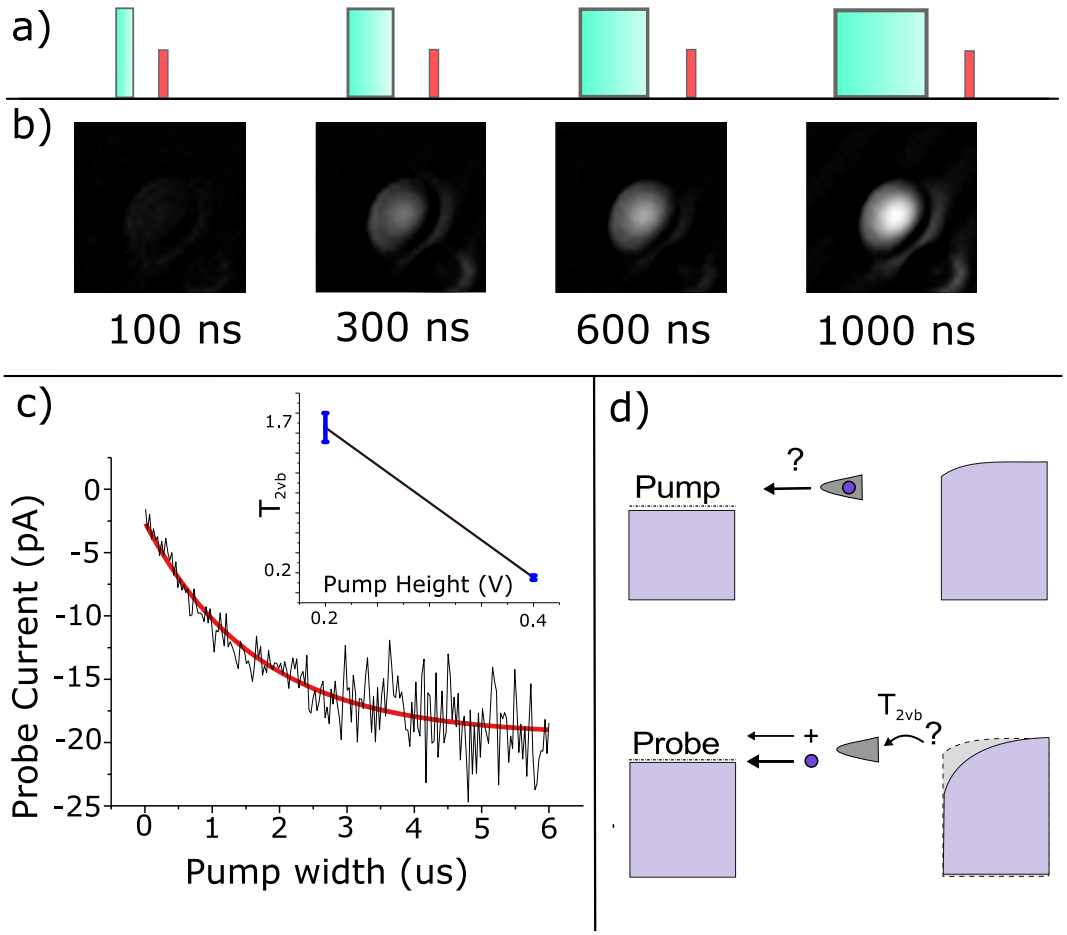

Figure 33: Measuring the Filling Rate a) A schematic of pulse series for the experiment. The relative delay between the pump and probes is swept while other parameters remain fixed.. b) Spatial images of the experiment, each image is a different time slice corresponding to a relative delay. c) The exponential decay in current, and the inset features the time constant for two different pump amplitudes. d) A schematic of the underlying mechanism being probed.

5.3.2 *Emptying Rate*

In another experiment we are able to measure the emptying rate of the (+/0) level to the tip by sweeping the relative delay between pump and probe while keeping the rest of the parameters fixed. Fig.34(a and d) show schematically the experiment. The pump pulse is set long enough to ensure that the (+/0) level is occupied with an electron. A probe pulse sent with a short delay will measure the system before

the electron has been emptied and will receive more current. A probe pulse with a long delay will measure the system after the electron has had the chance to be emptied and collect less current. We set the DC Bias -1.2 V, the pump amplitude to -0.4V, the pump pulse to 300 ns, the probe amplitude to -0.28 V, the probe pulse to 1 μs and the period to 50 μs. A sweep of delay time shows an exponential decrease in current from which we extract the emptying rate to the tip as $T_{2t} = 6$ μs.

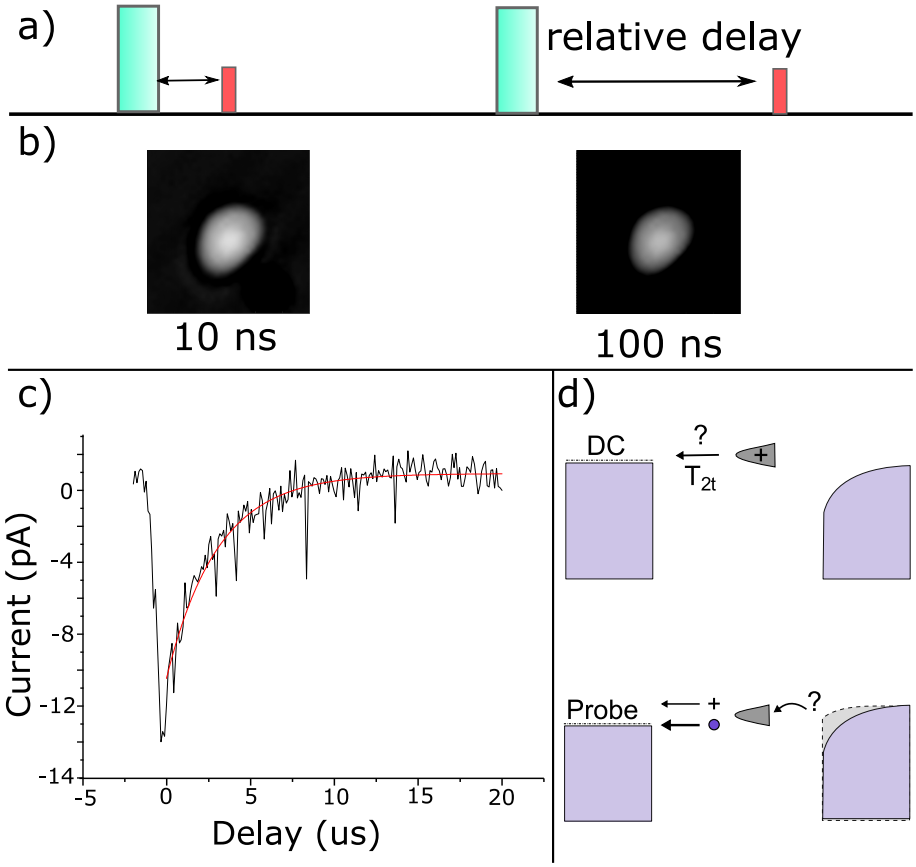

Figure 34: Measuring the Emptying Rate a) A schematic of pulse series for the experiment. The relative delay between the pump and probes is swept while other parameters remain fixed. b) Spatial images of the experiment, each image is a different time slice corresponding to a relative delay. c) The exponential decay in current. d) A schematic of the underlying mechanism being probed.

6

DANGLING BOND STRUCTURES

Techniques for the exact placement of DBs have allowed for fabrication of atomic patterns on the silicon surface. These advancements are critical in the development of atomic devices as it enables us to create structures with reproducible properties. This chapter will focus on several structures and their properties based on the interactions of the constituent DBs. All work presented here will be on a 1050 sample whose dopant network is assumed to be uniform. We will first take a cursory glance at several 2 DB structures to demonstrate the impact of their relative distance. We will then go into detail about multiple DB structures, namely dangling bond chains, building off the work of Wood et al [36]. The analyses presented here are unfinished, but worthy to report for future investigations.

6.1 INTERACTIONS OF TWO DBS

The electronic properties of DB structures is dependent on both their interactions with eachother and with the bulk. At close distances their interactions become strong and highly sensitive to small displacements. This section will show 2 DBs placed at various distances to illustrate this effect on their emergent properties. We will look at 2 DBs placed on a single dimer, and along the dimer row with and without an intervening H.

6.1.1 *A Bare Dimer*

When two adjacent DBs are created on a single dimer their close proximity, only 2.34 Å, allows them to couple strongly enough to form a covalent bond. The bond-

ing and antibonding orbitals are known as π and $\pi*$. dI/dV spectroscopy has measured their splitting to be slightly over 1 eV [3, 8]. This splitting is large enough that the antibonding and bonding states overlap with the CB and VB respectively. Consequently, the bare dimers are not able to localize charge as it "leaks" into the bulk – a test of this will be shown in Ch7. A schematic of the antibonding state is shown in Fig.35(a) with the corresponding empty state image featuring two distinct lobes. Similarly, Fig.35(b) shows a schematic of the bonding state where the corresponding filled state image and the dimer appears as one unit larger than a single DB.

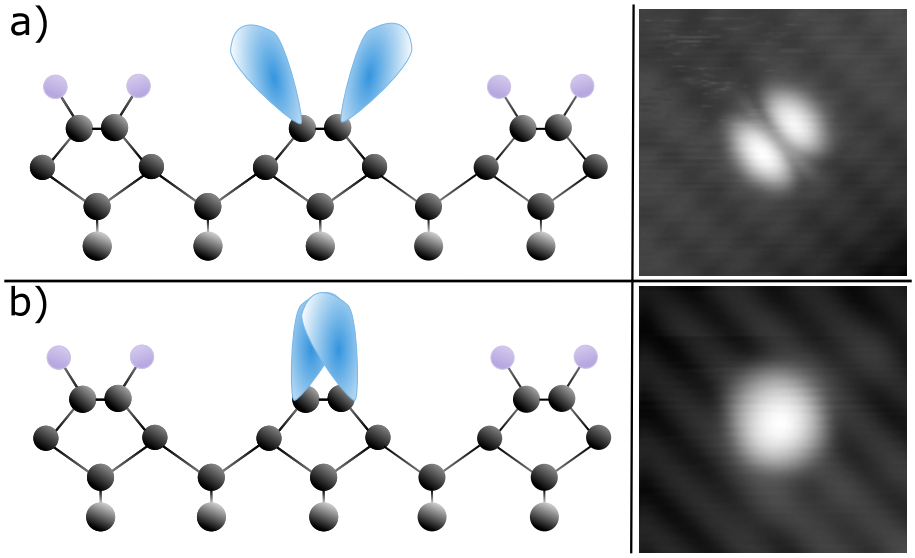

Figure 35: A Bare dimer. a) Schematic of the antibonding states and corresponding constant current 3x3 nm STM image with a setpoint of 1.4 V and 30 pA b) Schematic of the bonding states and corresponding constant current 3x3 nm STM image with a setpoint of -1.8 V and 30 pA.

6.1.2 *The "Antinode"*

The next feature is seen when 2 DBs have 1-3 intervening H atoms. Certain imaging conditions, usually empty states, will reveal a bright spot equidistant between the two atoms. The exact conditions vary, and it can vanish with microscopic tip changes. This feature is referred to in our group as the "antinode" since it ap-

pears at the midpoint where a node might be expected. An example is shown in Fig.36 where the two DBs have one intervening H atom. It can occur on different dimer rows, the same row, and at any angle. The smallest distance between atoms where it has been observed is 5.34 Å and its character varies significantly from the bare dimer bond. Previous efforts to understand this feature have been done by Schofield et al in [31] using Pösch Teller potentials as a model for single DBs. Numerical solutions of the bound states of these potential wells at appropriate spacings may shed light on the underlying physics of the antinode and other multiple DB systems. Their results show there is an excited state with a probability density in the region between the two DBs. They argue this state is imaged under the appropriate conditions and is responsible for the antinode feature.

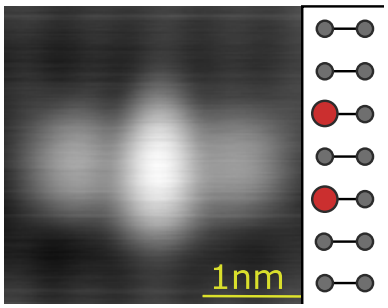

Figure 36: The Antinode. A 3x3 nm constant current picture with a setpoint of 1.3 V and 50 pA. Two DBs are place close together with one intervening H. Under these imaging conditions there is a bright feature in between the two DBs.

6.1.3 *The 2DB chain*

The final arrangement for 2 DBs is along the dimer row which has a spacing of 3.84 Å. We call this, and longer versions of it, dangling bond chains. The empty and filled state images in Fig.37 show that the two DBs look like a single unit under both imaging conditions. An additional observation is that a 2DB chain will form an antinode feature with another DB added one H spacing away as seen in Fig.38. This interaction might help in future investigations of the antinode structure, and

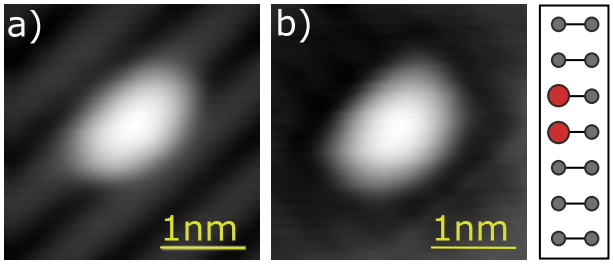

Figure 37: The 2DB chain. 3x3 nm constant current images of two DBs placed along a dimer row at the closest possible spacing. a) Filled state image taken at -1.8 V and 30 pA. b) Empty state image taken at 1.4 V and 30 pA.

it suggests that the 2DB chain acts in a similar way to a single DB. We will support the later statement in the following section as we study DB chains in detail.

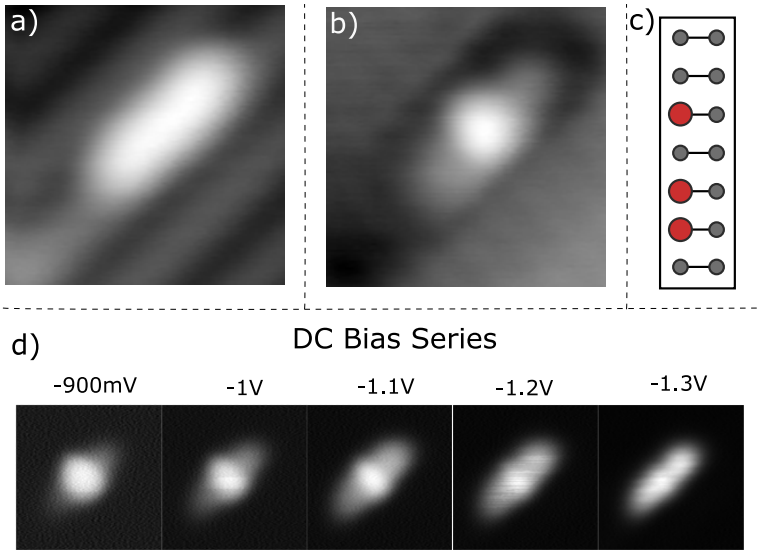

Figure 38: Antinode feature formed between a 2DB chained and another DB with an intervening H. All images are 3 x 3 nm a) Empty state constant current image with a set point of -1.8 V and 30 pA. b) Filled state constant current image with a set point of 1.4 V and 30 pA which shows the antinode feature in between the 2DB chain and the single DB. c) Schematic of the structure, where the red circles represent the position of the DBs. d) DC Bias series of constant height images with a set point of -1.8 V and 30 pA over Si-H. The antinode feature emerges at small negative bias.

6.2 DANGLING BOND CHAINS

For an extended structure with more than two equally spaced DBs, the closest possible spacing on the Si(100)-H surface is 3.84 Å along the dimer row. As described in the previous section, these are what we call DB chains. Chain lengths of 2-7 atoms have been explored in depth by Wood et al [36] using dI/dV mapping. This section will discuss this technique and my contributions to this work. Focusing on 2 and 3 DB chains we implement time resolved techniques to obtain a combined interpretation of these results. The final section will show a 6 atom ring structure on the Si(111)-H surface whose spacing is also 3.84 Å.

6.2.1 *The Implications of Probing Chains*

Before we look at the data, we will discuss initial attempts to model these chains. The single particle-in-a box description may be poor to describe our measurements because we are dealing with the following complexities: perturbations from the tip; changes in occupation; and a highly correlated few-electron system. The effects of the tip become complicated for an extended structure, especially whose occupation is not known. As we know from Ch.3 the tip creates a highly localized field at the surface. We will only look at empty state spectroscopy where the tip is positive relative to the sample. When considering spectroscopy of a single DB we understood the tip effect as shifting the DB levels lower in energy. For probing a chain structure, the presence of the tip will not only tilt the states of the entire chain, but will also force current from the bulk into the chain and then through the site below it. This may impose a change in occupation that hides the native structure from our measurements.

Previous work from our group has shown that 2 DBs are highly tunnel-coupled, estimating a tunneling rate as great as 10^{14} electrons per second [20]. If we extend these estimates to larger DB systems, we assume that the electrons can move freely within the chain to lower its total energy in the timescales we probe. This property

may give the tip the ability to "drag" charge around the chain. A study by Hitosugi et al [15] attributes the observed chain properties by STM to the lattice relaxation caused by the redistribution of charge. This energy lowering mechanism is known as Jahn-Teller distortion and should be carefully considered.

Despite these complications, our measurements ultimately do contain some information about the unperturbed electronic structure. The next few sections will not attempt to propose a model, but will make a few reasonable conclusions from our data. Further studies with Non-Contact Atomic Force Microscopy (NC-AFM) can be done at zero bias thereby mitigating the perturbations from the tip – and may provide useful information to further our understanding on this topic.

6.2.2 *dI/dV Mapping*

Using a lockin amplifier to implement the dI/dV technique we can spatially resolve the local density of states over the region of the DB chains. These measurements can be done in a plane to create an image, or in a line with a sweeping voltage to get a dI/dV spectroscopy linemap. A summary of data on 2, 3, and 4 DB chains is shown in Fig.39 made by John A. Wood and will be featured in [36]. My contributions to this work are the 2 and 4 DB chain data taken under the guidance of John A. Wood who measured the 3 DB chain data. The top of the figure shows a schematic of each structure. The two middle panels show constant current images – filled state image on the left and empty state image on the right. The emerging features at negative bias motivated the dI/dV studies at these energies. In the bottom panel are dI/dV linescans whose cross section is denoted by the dashed line in the images.

Of relevance is the apparent drop in density of states at around -1.1 V on each chain. As shown in Ch.5, this NDR feature is indicative of mutually exclusive states whose difference in energy is significant enough to alter the observed conductance when one is active over the other. We will use the time resolved tech-

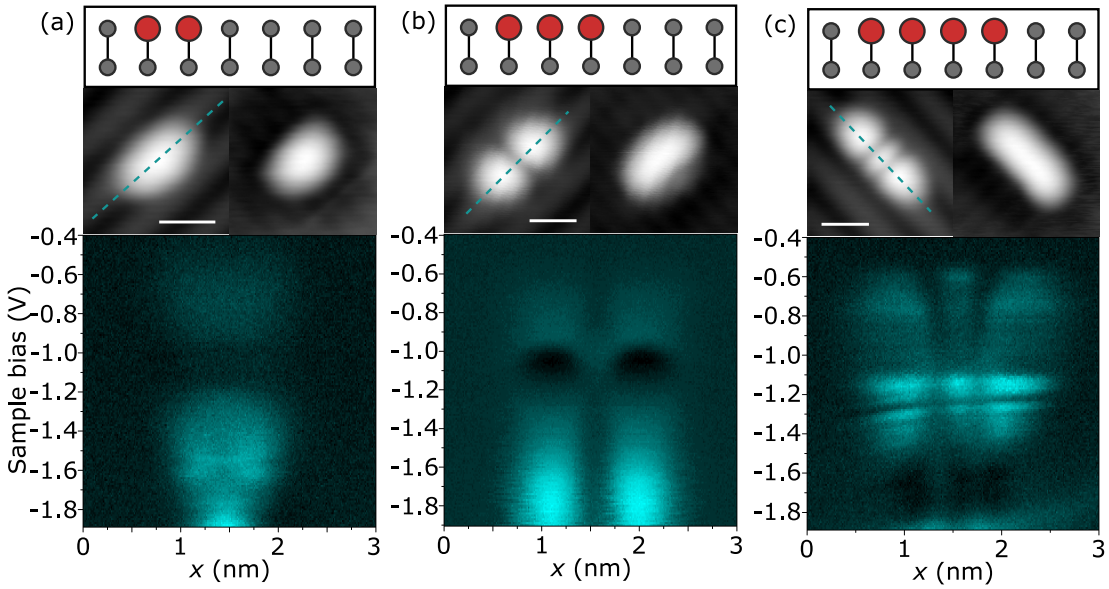

Figure 39: Characterization of 2,3 and 4 DB chains in a), b) and c) respectively. The first row shows a schematic of the chain structures along the dimer row. The second row shows 3x3 nm constant current images. Filled state image is the left with a setpoint of -1.8 V and 30 pA and empty state image on the right with a setpoint of 1.4 V and 30 pA. The last row features dI/dV linescans of each chain along the blue dotted line in the images.

niques developed in the previous chapter to explore these features on 2 and 3 DB chains.

6.2.3 *2DB chains*

The dI/dV linescans of the 2DB chain suggests that the structure acts as a single unit under the influence of the tip, and splitting only occurs past the VB onset. We predict that this chain will act similarly to a single DB in the gap for both DC and time resolved measurements. Height spectroscopy of a chain is shown in Fig.40(a) taken in between the two DB sites whose constant current images are shown in Fig.40(b). The height spectra reveal NDR, and the constant height images in Fig.40(c) reveal an NDR donut feature that extends over both DB sites.

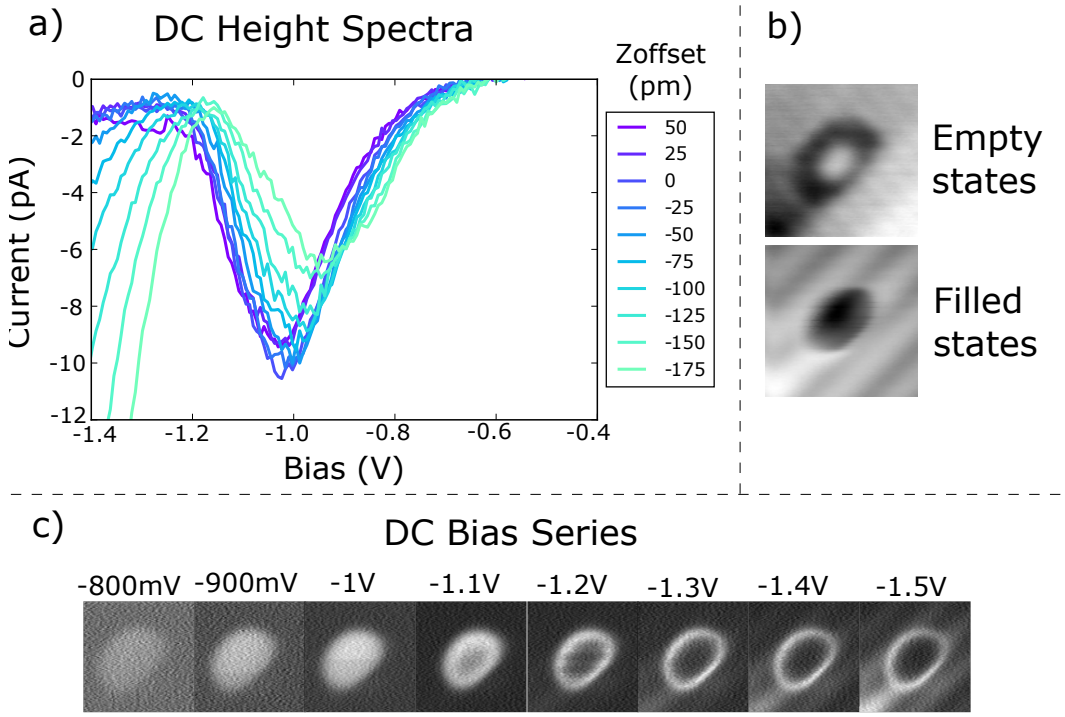

Figure 40: DC measurements over the center of a 2DB chain. a) DC height spectra over the center of the chain that shows NDR. b) 3x3 nm empty and filled state constant current images. The top image was taken at 1.4 V and 30 pA and the bottom iamges at -1.8 V and 30 pA. c) 3 x 3 nm constant height bias series with the current set at -1.8 V and 30 pA over Si-H.

The table in Fig.41(b) shows time resolved images for different heights and compares them with the DC images. Just like the single DB case, the donut feature grows for longer pulse widths and closer tip-sample distances. The time resolved I(V) curves resemble that of a single DB. Over the center, between the two DBs, the emptying rate T_{2t} at 1.2 V was found to be 282 ns while over the top DB was found to be 1.22 μs. This suggests that the overlap of the tip wavefunction at this energy is not maximal over the atom, but in the space between them. If we assume that this structure follows the same mechanism as the single DB system, these values can be used to calculate the filling rate T_{2b} of the lower energy state using Eq.64.

This collected evidence suggests that the 2DB chain forms two mutually exclusive states within the band gap of silicon that behave in similar way as the tran-

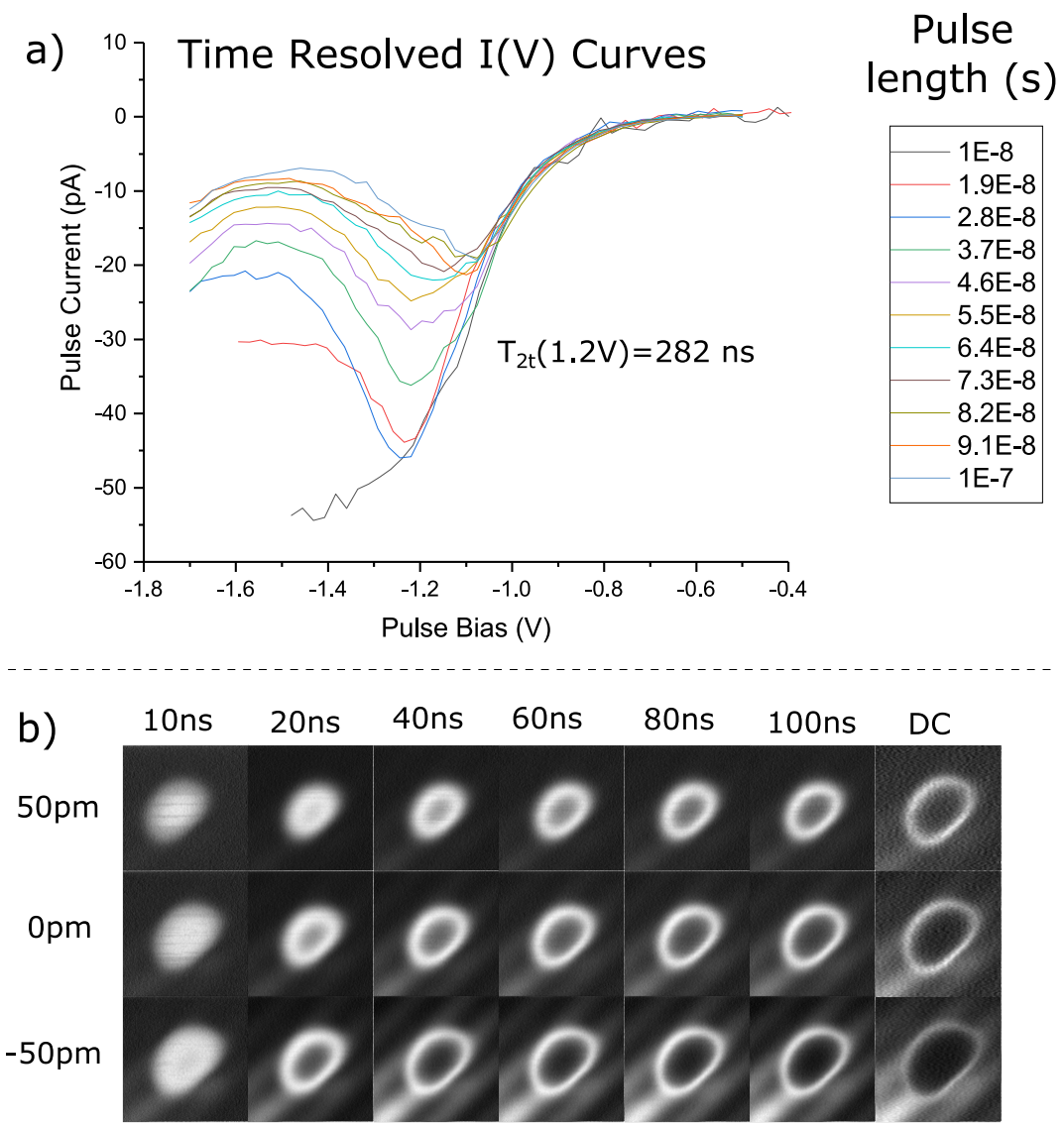

Figure 41: Time Resolved Measurements of a 2DB chain. a) Shows the time resolved I(V) curves over the center of the chain. b) A table shown the emerging NDR donut feature over the 2DBs for increasing pulse length and decreasing tip-sample distance. All images are 3x3 nm with a set point -1.8 V and 30 pA. The images compare a bias of 1.3 V.

sition levels of a single DB. The density of states is peaked in the region between the two DB sites.

6.2.4 *3DB chains*

Both the dI/dV mapping and the constant current images of the 3DB chain show a more exotic character than the 2DB chain. It features two distinct lobes with a minimum over the center DB. The two lobes have a clear NDR feature around -1.1 V while the center region is generally less conductive except for in the NDR region.

Fig.42 shows height I(V) spectra over the left, middle, and right DB. First seen by Wood et al [36], at far distances, the outside DBs show NDR, while the center one does not. Upon further investigation it was seen that as the tip approaches the sample, the center DB begins to show NDR. As you move in even further, the I(V) curves of the outside and middle DBs approach eachother. The constant height images in Fig.42(b) are taken in the NDR region at decreasing tip sample distances. We see that from farther out the chain looks like the constant current images. At 0 pm the lobes begin to show the NDR donut feature. The dark regions grow as the tip moves closer to the chain since the overlap between the tip and chain state increases in all directions. What begins as a low conductive region in between the lobes becomes more conductive as edges of the two donuts seem to merge. It appears that the character of the chain is spatially dominated by the two outside lobes that each behave similar to an isolated DB.

In a similar fashion we do time resolved measurements of the emerging NDR features of this chain. A table of time resolved images at different heights is shown in Fig.43. The NDR donut appears on each lobe for longer pulse widths and closer tip-sample distances – behaving like single DBs. For our I(V) curves we will first probe at a height where the two outside DBs show NDR while the center one does not - such as the 200pm offset in Fig.42. We perform time resolved I(V) measurements over each DB site to produce the curves seen in Fig.44. Similar to an isolated DB, the NDR of the outside lobes becomes extinguished for shorter pulse widths. What differs is a second feature that emerges at -0.95 V which decreases the peak of the current for shorter pulse widths. The emptying rate at -1.15 V over the top

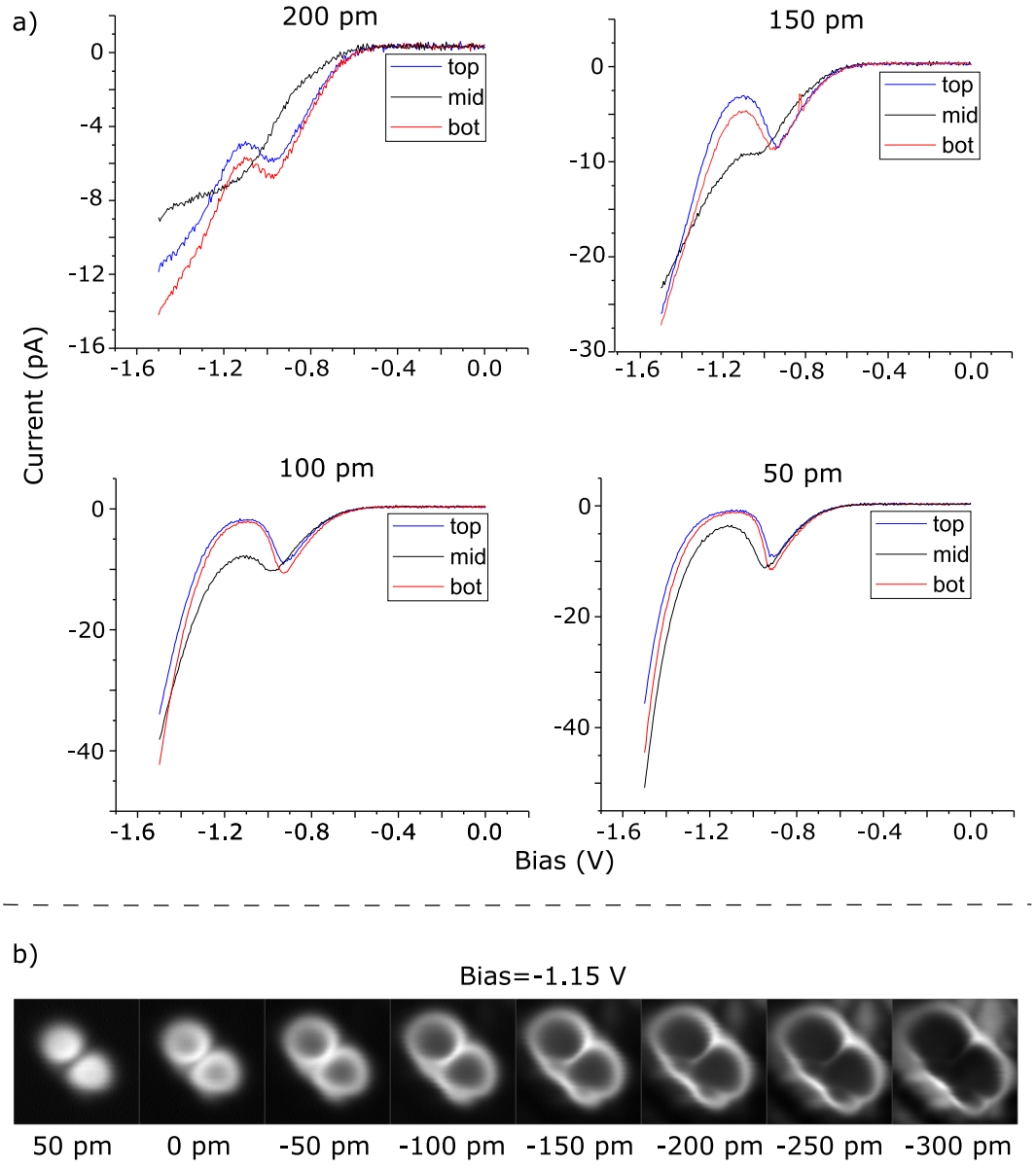

Figure 42: DC measurements of a 3DB chain. a) A comparison of height spectra over each site of a 3DB chain for different offsets. b) 3 x 3 nm constant current images with a set point of -1.8 V and 30 pA over Si-H. The images were taken with a DC bias of -1.15 V and moved closer in 50 pm intervals.

lobe was measured to be 264 ns and 258 ns over the bottom lobe. While the middle site is mostly unchanged with pulse length, there seems to be some splitting in the time resolved curves at -1.1 V onwards.

We continue this analysis at a height where each DB site shows NDR, namely the 100 pm offset in Fig.42. The time resolved curves in Fig.45 show the NDR

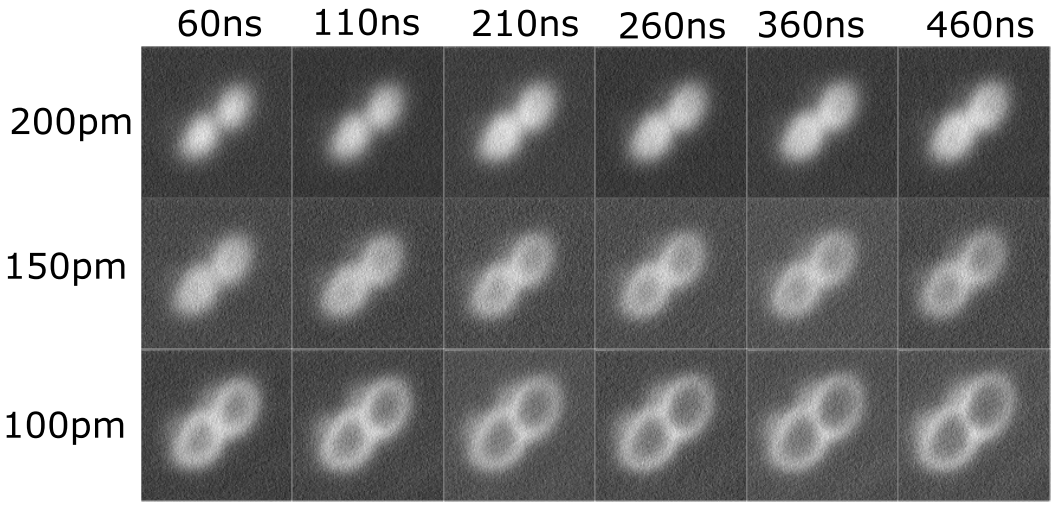

Figure 43: Bare dimer. a) Schematic of the antibonding states and corresponding filled state constant current STM image, 3x3 nm and setpoint of 1.4 V and 30 pA b) Schematic of the bonding states and corresponding empty state constant current STM image, 3x3 nm and setpoint of -1.8 V and 30 pA

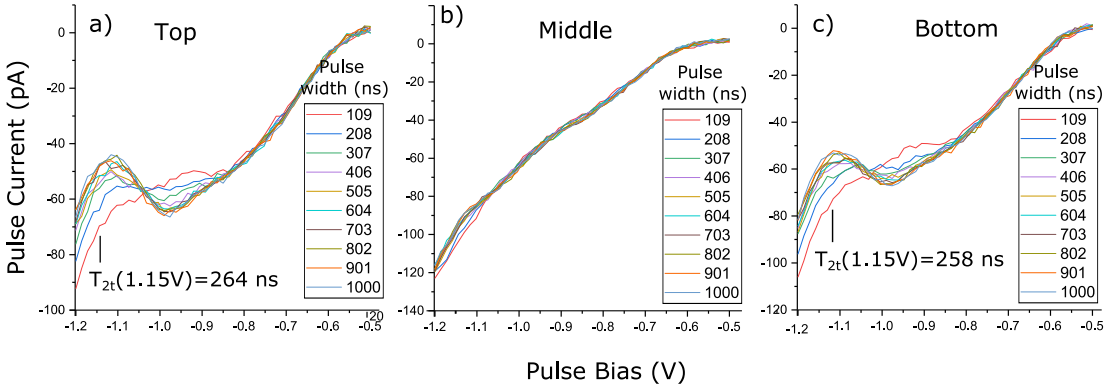

Figure 44: Time Resolved Curves for 3DB chain for far tip-sample distance. a and c) show the nearly identical time resolved responses for the outside lobes of the 3DB chain. b) Time resolved curves over the " node" in between the two lobes and shows no time dependence.

becoming extinguished at all three points for shorter pulses. The extra feature at -0.95 V is also present at each site. To look closer at this feature we separate the curves of the bottom DB site into two different time scales shown in Fig.46.

Starting at long pulses of 1μs we reproduce the DC I(V) curve. As the pulse widths decrease we see that the current peak shrinks while the NDR region be-

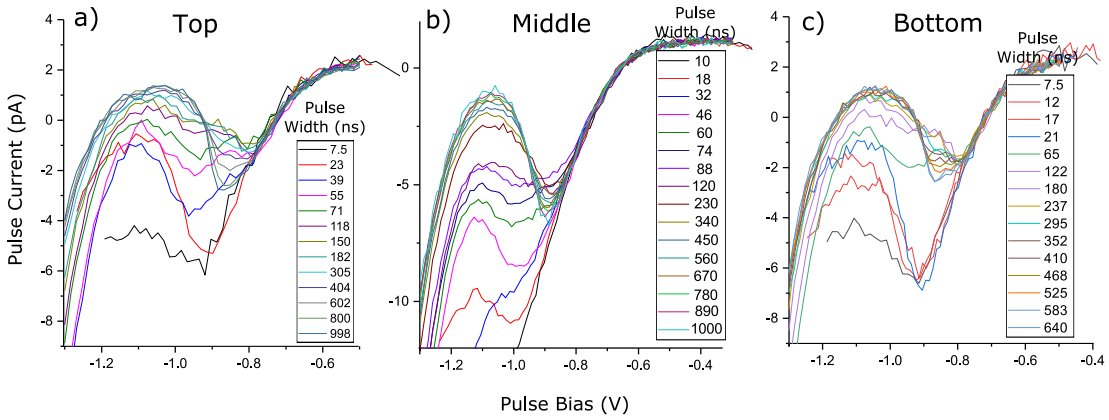

Figure 45: Time Resolved Curves for 3DB chain at close tip-sample distance. a and c) show the nearly identical time resolved responses for the outside lobes of the 3DB chain. b) Time resolved curves over the " node" in between the two lobes which now shows time dependence, but remains distinct from the lobes.

gins to gain current. For pulse lengths around 100 ns a second bump appears marked by the red star. Here begins the second phase. Now as the pulse widths continue to decrease the peak current begins to grow, and eventually we return to the time resolved curves we would expect over a single DB. This suggests there is some intermediate process between the two mutually exclusive states we would normally attribute to NDR. If we try to do a fit in the NDR regime at -1.1 V then we get a double exponential. Over both the outside and center DB sites the fast time constant is around 5 ns, and the larger is on the order of 200 ns. This may also be true for the curves taken at 200 pm in Fig.44, however this data was not taken. The origin of these effects is difficult to determine, but may be related to delocalization of charge or Jahn-Teller distortion [15].

6.2.5 *6 atom Ring*

The symmetry of the Si(111)-H surface allows for patterns that cannot be made on Si(100)-H. Fig.47 shows a 6 atom "Benzene" like ring made with DBs on the silicon surface. Like the chains, the distance between each DB on the ring is 3.84 Å. While patterning it was found that the DBs are more likely to "hop" over from an adjacent

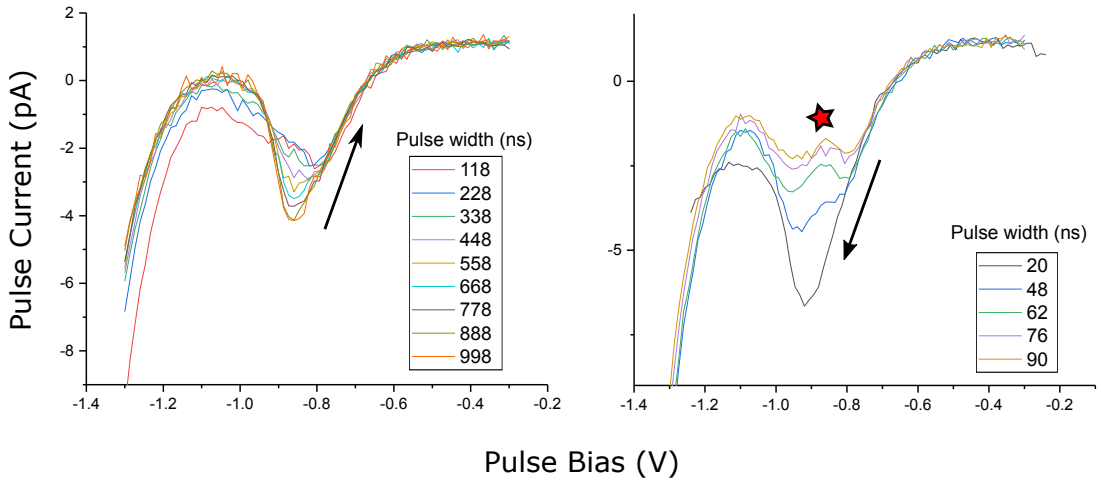

Figure 46: Spectroscopy of in Fig.45(c) split into two time regimes. a) Longer pulses from 1μs to 100 ns. The red star marks an emerging second bump b) Short pulses from 90 to 20 ns.

site instead of making a new DB. Fig.47(c) shows filled and empty state images of the patterns leading up to the 6 atom structure. While the images of the ring bear a striking resemblance to a benzene molecule, it may be too presumptuous to call it so before we probe its electronic properties. For reference, the bond length between carbon atoms on benzene is around 1.40 Å. Comparing with 2, 3 and 4 DB chains, we see no emergent features in the filled state images of the ring. Future characterization may reveal the role of the lattice on the interactions of DBs but were not carried out due to the surface effects described in Ch.4.

Well known studies in scanning probe microscopy have measured the Highest Occupied Molecular Oribtal (HOMO) and Lowest Unoccupied Molecular Orbital (LUMO) of pentacene molecules on NaCl films evaporated on a Cu(100) surface [29]. Related work has used NC-AFM to probe the short range chemical forces on pentacene molecules resolving the C-C bonds [14]. Our group has the available techniques for these analyses, and it would be interesting to compare these results with measurements on a silicon "benzene". This would explore the implications of increased bond length, and the basic interactions within these quantum objects.

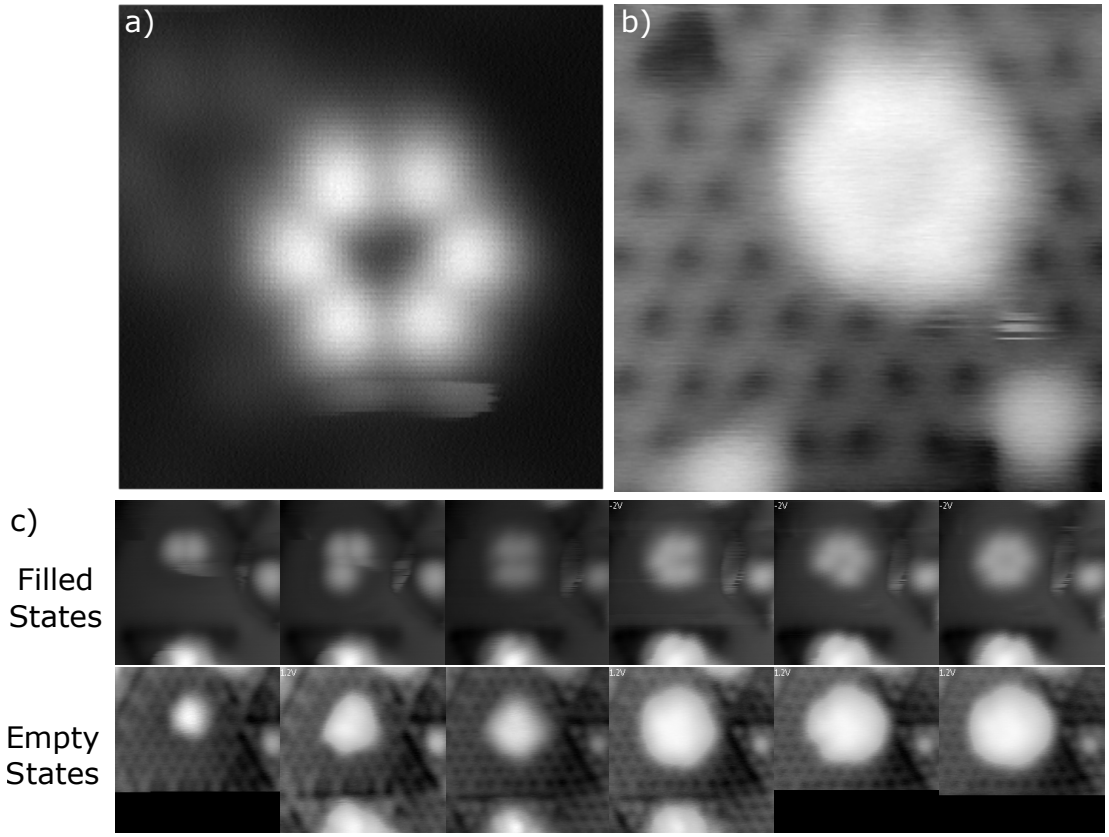

Figure 47: STM constant current images of a 6 atom ring on the Si(111)-H showing a "Benzene" type structure. Empty state images taken at 1.2V and 50 pA, filled state images taken at -2 V and 50 pA a) Filled state image where each DB in the structure is visible b) Empty state image where each site is a large bright protrusion. c) Filled and Empty state images of several structures leading up to the ring.

7

CHARGE SENSING

This chapter demonstrates the application of a DB as an electrostatic probe. Our exploration of the single DB spectroscopy in Ch.5 has given us insight into the transition levels of the DB whose energetic positions will be sensitive to nearby charge. We can interpret relative changes in spectroscopy as a measurement of the electronic environment. This will be used to indirectly probe the native charge character of nearby structures, removing the perturbation of the tip if we were to measure them directly. To do this we require the probing target to be far enough away that the tip negligibly affects it, but close enough that a DB will be electrostatically affected by it. For this reason a 1250°C flashed sample was used due to its longer screening length at the surface. First we will show examples to explain the electrostatic shifts, and then we will use them to probe the native charge of DB chains and dimers.

7.1 SHIFTING ENERGY LEVELS

Our first task is to understand how the spectrum of a DB shifts in response to a charge. The image series in Fig.48 shows clearly that the addition of DBs will change the character of the initial one. We see a bright DB in a) and successive charges are added until it becomes dark in c). To understand this observation we look back at concepts in Ch.3 where the effective field at a given site will energetically shift the states. The transition levels of the DB in the presence of a negative charge will cause them, and the surrounding bands, to bend upwards – and the opposite for a positive charge. Since the native charge state of a DB is negative, we can shift its energy levels upwards by adding another DB nearby.

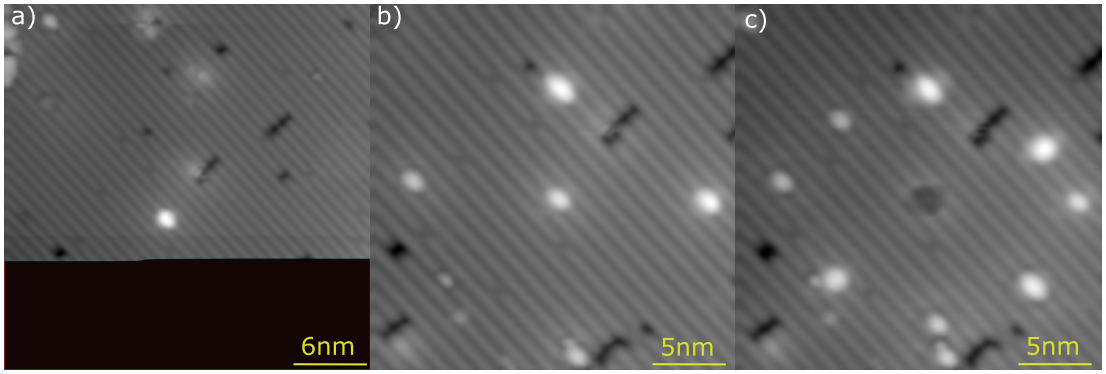

Figure 48: STM observations of DB changing the character of another. These constant height images were taken with a set point of -1.8 V and 30 pA. a) Shows a 30 x 30 nm image of a single DB that appears bright. b) Shows a 15 x 15 nm image with DBs added around the original one. c) A 15 x 15 nm images of the orignal DB now appearing dark as DBs continued to be added around it.

This is intuitive since it will take more energy to add an electron onto the DB if there are other negative charges in the vicinity.

Starting simple, we look at the response of one DB to the addition of another, shown in Fig.49. The black I(V) curve in a) shows the initial spectroscopy over the original DB, and the red curve is the spectroscopy after the second DB was added. The schematic in c) shows a simple model of the transition levels and the bands being pushed upwards in the presence of the charge. We understand the shifted curves by discussing each of its features and their relation to the newly positioned transition levels. First, the current peak has decreased indicating that the CB is bent upwards such that there are fewer states below the Fermi level. Second is the NDR region which has been shifted to smaller negative bias. This is because the (+/0) level is now higher in energy and will be emptied sooner by the tip. The NDR region tends to 0 since the current peak, and hence filling rates from the CB, have decreased – causing the average occupation of the DB to tend to 0. Finally, the VB onset is shifted lower in energy since the (+/0) level is higher and will be swept into resonance with the VB later.

We compare this with another method to adjust the local field for a DB – by approaching it with the tip as shown in Fig.50. At negative biases the tip appears

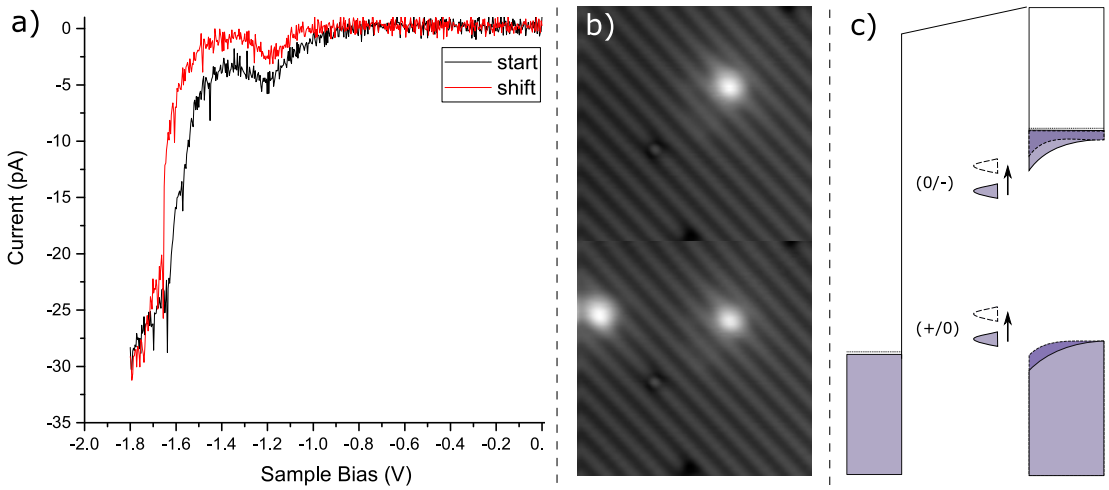

Figure 49: The response of a DB to a nearby charge. a) I(V) curves of a DB before (black) and after (red) adding a nearby charge. b) Filled state images taken at -1.8V and 30pA of the DB before and after the charge was added. c) Schematic of the level shifts due an external electric field.

.

as a positive charge to the DB. Moving the positive tip away will have a similar effect on the spectra as adding a negative DB nearby. The main differences are that the magnitude of TIBB changes with the Fermi level of the tip, and will be swept along with voltage in the I(V) curve. Secondly when the tip is moved closer, its overlap with the DB will increase and affect the spectroscopy. These implications are most obvious in the NDR region where the current tends to 0 as the positive tip is moved in. The distance that adding a charge can affect a DB is on the order of nanometers, while the tip effects occur with displacements on the order of angstroms. This indicates that the tip is not likely to affect the charge state of the surrounding negative DBs while probing the one of interest.

7.1.1 *3DB Chain Shifting*

These electrostatic effects are important for structures, and may be an integral mechanism in an atom scale device such as QCA. Here we will turn to a 3DB chain and use this level shifting technique to peek at the underlying electronic

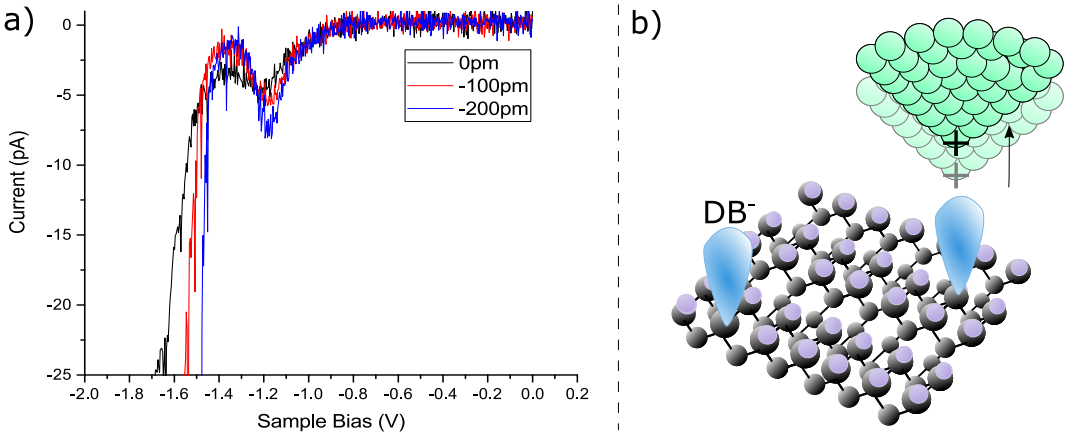

Figure 50: Tip effects. a) Height spectra of the DB in Fig.49 before the charge was added. b) Shows a schematic of the different methods to change the local field on a DB. One is to add nearby negative charge, the other is to move the tip closer.

structure. The image series in Fig.51(a-d) starts with a familiar constant current image of a 3DB chain with two distinct lobes. As DBs are added around the chain we see that at a certain point the chain switches character such that the center is bright and the outside lobes are dark. We attribute this to the higher energy state being pushed past the Fermi level of the sample and becoming inaccessible to the tip during imaging. As shown in Fig.51(e) the current can only be drawn through the lower state which is reflected in the image. The two states shown here are examples of multi potential well solutions calculated by Dr. Lucian Livadaru.

Experiments have also been done to spatially shift the electronic density of chains by adding a DB along the dimer row several sites away. For a 3DB chain this causes the NDR feature to be asymmetric in the lobes. Most notable is the work by Wood et al [36] on the pertubation of a 7DB chain. In this study, the addition of a DB with one H atom between it and the chain, the dI/dV linescan shows a significant shift of electron density to the opposite side of the chain.

7.2 CHARGE SENSING

The electrostatic effect between structures and DBs is mutual. Here we exploit the known spectroscopic character of a DB as a charge sensor to other entities on the

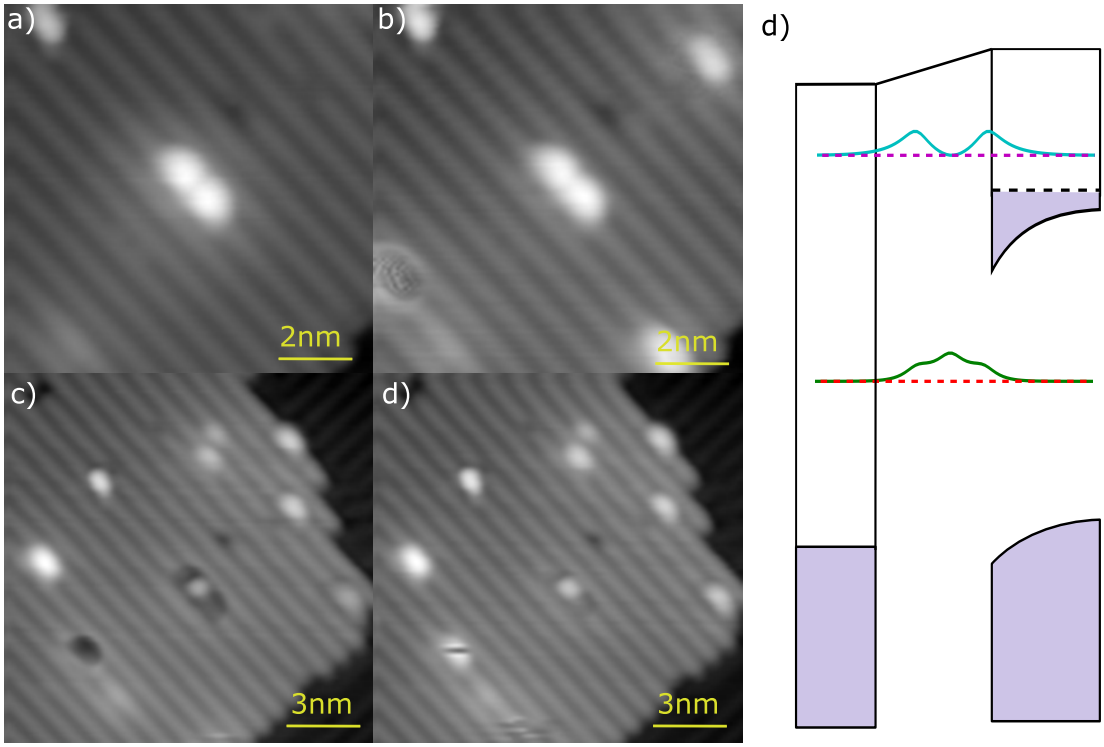

Figure 51: Shifting a 3DB chain a-d) Constant height images of a 3DB chain with successive DBs added around it. The set point is -1.8 V and 30 pA. e) Schematic of the excited 3DB chain state pushed above the Fermi level of the sample, leaving only the ground state as a medium for the current through the gap.

surface. We will show two examples, one with DB chains of various lengths and the other with a bare dimer.

7.2.1 *Chains*

First we explore the native charge state of DB chains, Fig.52(a) shows an image of the experiment. The charge sensing DB is placed at the center and the numbers indicate the order in which the other DBs were added. The corresponding I(V) curves are shown in Fig.52(b). The initial 3 added charges successfully shift the I(V) curve. Upon creating a 2DB chain there is a very small shift, and the successive addition to 3 and 4 DB lengths shows no shift. This indicates that the same amount of charge is held by the 2, 3 and 4 DB chains and is likely equal to one. We must

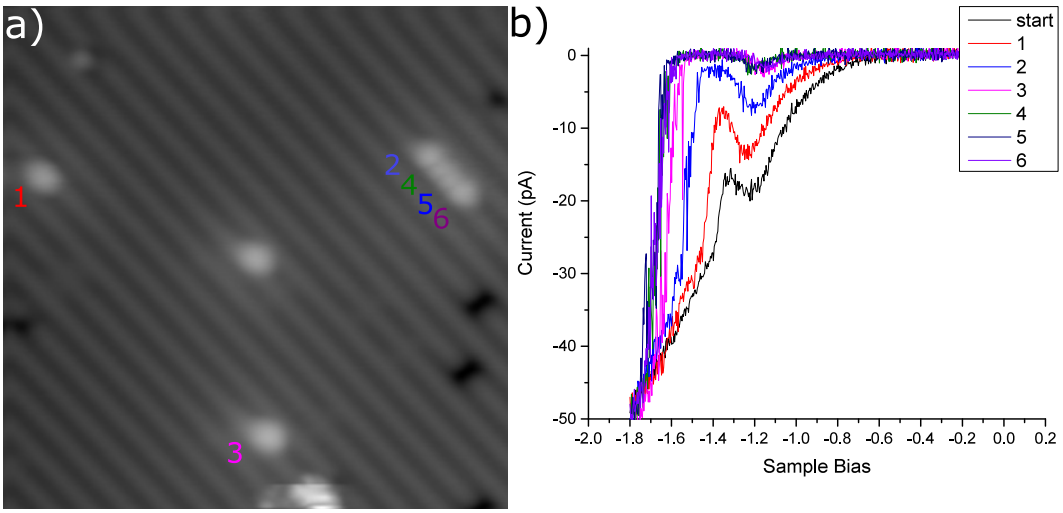

Figure 52: Charge sensing of a Molecule a) The filled state image of the experiment. The DBs were added in the order that they are labelled, the center DB is the probe. b) The corresponding I(V) curves of the probe DB after each other one was added.

keep in mind that the doping concentration of this surface is lower than the one used in Ch.6 and may have an influence on the occupation.

7.2.2 *Dimer*

The second experiment is with a bare dimer. As mentioned in Ch.6, it is believed the DBs will form a π and π* bond that overlap with the valence band and conduction band respectively. Because of this overlap charge cannot localize on a bare dimer. We predict a bare dimer should not cause a shift in our charge sensing DB. Again, as shown in the image series of Fig.53, the center DB corresponds to the charge sensing DB while the enumerated structures are labeled in the order which they are added. The addition of single DBs in a) and b) show the familar shift, while the creation of a dimer in c) shows a backwards shift. This suggests that the bare dimer holds less charge than the DB, and demonstrates its inability to localize charge.

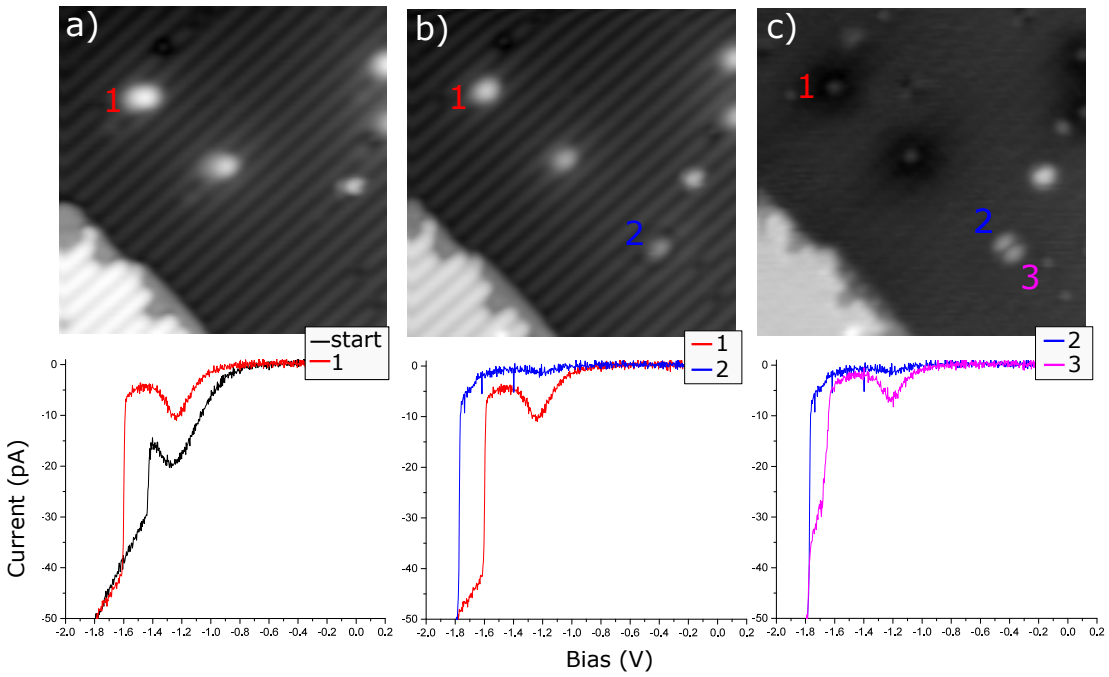

Figure 53: Charge sensing of a bare dimer. The center DB is probed as the charge sensing element whereas the surrounding DBs were added in succession as indicated by their number labels. a and b) Filled state image of a DB being added and the corresponding I(V) curve shift. c) Empty state image of a dimer being created and the corresponding backward shift of the I(V) curve.

8

CONCLUSIONS AND FUTURE WORKS

Here we will summarize what has been covered, the remaining issues, and future research paths. The work presented here is an important step on the way to creating atomic scale devices, and to explore the fundamental interactions of quantum structures on the silicon surface.

8.1 SUMMARY OF RESULTS

We have been able to characterize the mid gap states of dangling bonds, and have extended this understanding to explore their long and short range interactions.

8.1.1 *Dangling Bond Charge Dynamics*

In Ch.5 we presented the observed NDR on DBs as a signature of two mutually exclusive states within the bandgap of silicon. The decrease in current is due to a rate limiting single electron capture event to the lower (+/0) level. With time resolved techniques we were able to image and probe this capture event, giving us the lifetime of the positively charged DB before it is filled from the CB. Further, we use a pump probe technique to measure the filling of this same level when it is brought into resonance with the VB. These results not only show our understanding of the charge dynamics, but have given us real values for the associated rates. This allows us to compare the effects of doping density and temperature.

8.1.2 *Time Resolved Chains*

Upon recognition of NDR features in the dI/dV linescans of DB chains, in Ch.6 we implement time resolved techniques on these structures. We show that both 2 and 3 length chains have a rate limiting process that suggests they too have a set of mutually exclusive states in the silicon band gap. The 2DB chain acts in a similar way to a single DB with a state density centered between the two DB sites. The 3DB chain has a lobe at each end that show character similar to an isolated DB, and a node in the center whose properties are height dependent. There is an additional feature on the 3DB chains at higher energy and a second time scale we have yet to explain.

8.1.3 *Charge Sensing*

We have used our knowledge of the transition levels of a single DB as a probe for charges on the surface in Ch.7. A shift in the I(V) curve of a DB corresponds to a change in energetic positions of the transition levels that are sensitive to electrostatic forces. With this technique we have been able to indirectly probe the native charge character of structures on the surface, alleviating them of the perturbation of the tip. We have found that on the 1250 sample that chain lengths of 2, 3 and 4 have the same electrostatic effect on a probe DB and likely hold a single charge. We also explored the bare dimer, which upon its creation from a single DB shifted the spectra in a way that indicates a negative charge has been removed. We use this as a verification that the bare dimers π and π^* states are resonant with the VB and CB preventing it from localizing charge.

8.2 FUTURE WORKS

A greater understanding of DBs and their interactions will only continue to open up new paths for research and application. To explore deeper we look towards

new tools such as NC-AFM. To broaden our possibilities we look at new and more versatile surfaces such as Si(111)-H.

8.2.1 *Non-Contact Atomic Force Microscopy*

NC-AFM is a truly spectacular technique that uses frequency shifts of an oscillating cantilever to sense forces at the atomic scale without damaging the surface or probe. Labidi et al [18] from our group have used this technique to image the underlying chemical bonds between Si atoms on the Si(100)-H surface. It is particularly advantageous for probing DBs and DB structures because it does not require an applied bias to receive signal. The TIBB effects are reduced to the contact potential difference between the tip and sample materials. Further, the lack of current avoids non equilibrium situations, or imposing occupations as we discussed in Ch.6. AFM studies on the DB chains may be able to solve questions related to native occupation and deformation of the lattice.

8.2.2 *Si(111)-H*

Briefly mentioned in both Ch.4 and Ch.5 is the hydrogen terminated Si(111) surface which remains a tantalizing prospect for atomic studies. Achieving a defect free surface is an ongoing aspiration. Not only does the 1x1 reconstruction result in a more isotropic behaviour of DBs, the geometry permits more freedom in patterning – for example, a 4 atom QCA cell can be made completely symmetric.

8.3 A FINAL NOTE

We have demonstrated the controllable placement of quantum dots on the atomic scale, and that they, and their structures, have reproducible electronic properties. We have shown that we can perturb and probe their character, incrementally gaining knowledge about their nature. With every step is a new tool, and new possibil-

ities. Our ultimate goal is a unique atomic scale device, whose development goes hand in hand with scientific progress.

BIBLIOGRAPHY

[1] W. Neil Ashcroft and N. David Mermin. *Solid State Physics*. Brooks/Cole, 1976.

[2] M. Balkanski, A. Aziza, and E. Amzallag. "Infrared Absorption in Heavily Doped n-Type Si." In: *physica status solidi (b)* 31.1 (1969), pp. 323–330. ISSN: 1521-3951. DOI: 10.1002/pssb.19690310138. URL: http://dx.doi.org/10.1002/pssb.19690310138.

[3] Amandine Bellec, Damien Riedel, Gérald Dujardin, Ouarda Boudrioua, Laurent Chaput, Louise Stauffer, and Philippe Sonnet. "Electronic properties of the *n*-doped hydrogenated silicon (100) surface and dehydrogenated structures at 5 K." In: *Phys. Rev. B* 80 (24 2009), p. 245434. DOI: 10.1103/PhysRevB.80.245434. URL: https://link.aps.org/doi/10.1103/PhysRevB.80.245434.

[4] G. Binnig, H. Rohrer, Ch. Gerber, and E. Weibel. "Tunneling through a controllable vacuum gap." In: *Applied Physics Letters* 40.2 (1982), pp. 178–180. DOI: 10.1063/1.92999. eprint: http://dx.doi.org/10.1063/1.92999. URL: http://dx.doi.org/10.1063/1.92999.

[5] G. Binnig, H. Rohrer, Ch. Gerber, and E. Weibel. "7 x 7 Reconstruction on Si(111) Resolved in Real Space." In: *Phys. Rev. Lett.* 50 (2 1983), pp. 120–123. DOI: 10.1103/PhysRevLett.50.120. URL: https://link.aps.org/doi/10.1103/PhysRevLett.50.120.

[6] Julian C. CHEN. *Introduction to Scanning Tunneling microscopy. Second Edition*. Oxford University Press, 2008.

[7] C. Caroli, R. Combescot, P. Nozieres, and D. Saint-James. "Direct calculation of the tunneling current." In: *Journal of Physics C: Solid State Physics* 4 (1971), pp. 916–929. ISSN: 0022-3719. DOI: 10.1088/0022-3719/4/8/018. arXiv: 0022-3719/4/8/018 [10.1088].

[8] Dongxue Chen and John J. Boland. "Chemisorption-induced disruption of surface electronic structure: Hydrogen adsorption on the Si(100)-2x1 surface." In: *Phys. Rev. B* 65 (16 2002), p. 165336. DOI: 10.1103/PhysRevB.65.165336. URL: https://link.aps.org/doi/10.1103/PhysRevB.65.165336.

[9] "Consequences of Many-Cell Correlations in Clocked Quantum-Dot Cellular Automata." In: *IEEE Transactions on Nanotechnology* 14.4 (2015), pp. 638–647. ISSN: 1536125X. DOI: 10.1109/TNANO.2015.2426058.

[10] P.H. Cutler, Jun He, J. Miller, N.M. Miskovsky, B. Weiss, and T.E. Sullivan. "Theory of electron emission in high fields from atomically sharp emitters: Validity of the Fowler-Nordheim equation." In: *Progress in Surface Science* 42.1 (1993), pp. 169 –185. ISSN: 0079-6816. DOI: http://dx.doi.org/10.1016/0079-6816(93)90068-7. URL: http://www.sciencedirect.com/science/article/pii/0079681693900687.

[11] R. M. Feenstra, W. A Thompson, and A. P Fein. "Real-Space Observation of π-Bonded Chains and Surface Disorder on Si(111)2x1." In: *Phys. Rev. Lett.* 6 (1986), pp. 1–5.

[12] R M Feenstra, Y Dong, M P Semtsiv, and W T Masselink. "Influence of tip-induced band bending on tunnelling spectra of semiconductor surfaces." In: *Nanotechnology* 18.4 (2007), p. 044015. URL: http://stacks.iop.org/0957-4484/18/i=4/a=044015.

[13] Alex D Gottlieb and Lisa Wesoloski. "Bardeen's tunnelling theory as applied to scanning tunnelling microscopy: a technical guide to the traditional interpretation." In: *Nanotechnology* 17.8 (2006), R57. URL: http://stacks.iop.org/0957-4484/17/i=8/a=R01.

[14] Leo Gross et al. "The Chemical Structure of a Molecule Resolved by Atomic Force Microscopy." In: *Science* 325.August (2009), pp. 1110–4. ISSN: 1095-9203. DOI: 10.1126/science.1176210. URL: http://www.ncbi.nlm.nih.gov/pubmed/19713523.

[15] Taro Hitosugi, S Heike, T Onogi, T Hashizume, S Watanabe, Z Li, K Ohno, Y Kawazoe, T Hasegawa, and K Kitazawa. "Jahn-Teller Distortion in Dangling-Bond Linear Chains Fabricated on a Hydrogen-Terminated Si (100) - 2 x 1 Surface." In: 1.100 (1999), pp. 1–4.

[16] N M Johnson, D K Biegelsen, M D Moyer, S T Chang, E H Poindexter, P J Caplan, N M Johnson, D K Biegelsen, M D Moyer, and S T Chang. "Characteristic electronic defects at the Si-SiO2 interface Characteristic electronic defects at the Si-SiO2 interface." In: 563.May 2014 (1988), pp. 57–60. DOI: 10.1063/1.94420.

[17] D. Dale Kleppinger and F.A. Lindholm. "Impurity concentration dependent density of states and resulting fermi level for silicon." In: *Solid-State Electronics* 14.5 (1971), pp. 407 –416. ISSN: 0038-1101. DOI: http://dx.doi.org/10.1016/0038-1101(71)90191-2. URL: http://www.sciencedirect.com/science/article/pii/0038110171901912.

[18] Hatem Labidi, Mohammad Koleini, Taleana Huff, Mark Salomons, Martin Cloutier, Jason Pitters, and Robert A Wolkow. "images of a hydrogen-terminated silicon surface." In: *Nature Publishing Group* 8 (2017), pp. 1–7. DOI: 10.1038/ncomms14222. URL: http://dx.doi.org/10.1038/ncomms14222.

[19] Haiping Lin, Janosch M C Rauba, Kristian S. Thygesen, Karsten W. Jacobsen, Michelle Y. Simmons, and Werner a. Hofer. "First-principles modelling of scanning tunneling microscopy using non-equilibrium Green's functions." In: *Frontiers of Physics in China* 5.4 (2010), pp. 369–379. ISSN: 16733487. DOI: 10.1007/s11467-010-0133-4.

[20] Lucian Livadaru, Peng Xue, Zahra Shaterzadeh-Yazdi, Gino A DiLabio, Josh Mutus, Jason L Pitters, Barry C Sanders, and Robert A Wolkow. "Dangling-bond charge qubit on a silicon surface." In: *New Journal of Physics* 12.8 (2010), p. 083018. URL: http://stacks.iop.org/1367-2630/12/i=8/a=083018.

[21] Lucian Livadaru, Peng Xue, Zahra Shaterzadeh-Yazdi, Gino A. Dilabio, Josh Mutus, Jason L. Pitters, Barry C. Sanders, and Robert A. Wolkow. "Dangling-

bond charge qubit on a silicon surface." In: *New Journal of Physics* 12 (2010). ISSN: 13672630. DOI: 10.1088/1367-2630/12/8/083018. arXiv: 0910.1797.

[22] Sebastian Loth, Markus Etzkorn, Christopher P Lutz, DM Eigler, and Andreas J Heinrich. "Measurement of fast electron spin relaxation times with atomic resolution." In: *Science* 329.5999 (2010), pp. 1628–1630.

[23] F. J. Morin and J. P. Maita. "Electrical Properties of Silicon Containing Arsenic and Boron." In: *Phys. Rev.* 96 (1 1954), pp. 28–35. DOI: 10.1103/PhysRev.96.28. URL: https://link.aps.org/doi/10.1103/PhysRev.96.28.

[24] Nevill F Mott and WD Twose. "The theory of impurity conduction." In: *Advances in Physics* 10.38 (1961), pp. 107–163.

[25] Fredrik Owman and Per Mårtensson. "STM study of Si(111)1 × 1-H surfaces prepared by in situ hydrogen exposure." In: *Surface Science* 303.3 (1994), pp. L367 –L372. ISSN: 0039-6028. DOI: http://dx.doi.org/10.1016/0039-6028(94)90772-2. URL: http://www.sciencedirect.com/science/article/pii/0039602894907722.

[26] Jason L Pitters, Paul G Piva, and Robert A Wolkow. "Dopant depletion in the near surface region of thermally prepared silicon (100) in UHV." In: *Journal of Vacuum Science and Technology B* 30.2 (2012), pp. 021806+. ISSN: 2166-2746. DOI: 10.1116/1.3694010.

[27] Mohammad Rashidi, Marco Taucer, Isil Ozfidan, Erika Lloyd, Mohammad Koleini, Hatem Labidi, Jason L. Pitters, Joseph Maciejko, and Robert A. Wolkow. "Time-Resolved Imaging of Negative Differential Resistance on the Atomic Scale." In: *Phys. Rev. Lett.* 117 (27 2016), p. 276805. DOI: 10.1103/PhysRevLett.117.276805. URL: https://link.aps.org/doi/10.1103/PhysRevLett.117.276805.

[28] Mohammad Rashidi, Jacob A. J. Burgess, Marco Taucer, Jason L. Achal Roshanand Pitters, Sebastian Loth, and Robert A. Wolkow. "Time-resolved single dopant charge dynamics in silicon." In: *Nature Communications* 7 (2016),

p. 13258. DOI: 10.1038/ncomms13258. URL: http://dx.doi.org/10.1038/ncomms13258.

[29] Jascha Repp, Gerhard Meyer, Sladjana M. Stojković, André Gourdon, and Christian Joachim. "Molecules on insulating films: Scanning-tunneling microscopy imaging of individual molecular orbitals." In: *Physical Review Letters* 94.2 (2005), pp. 1–4. ISSN: 00319007.

[30] Moh'd Rezeq, Jason Pitters, and Robert Wolkow. "Tungsten nanotip fabrication by spatially controlled field-assisted reaction with nitrogen." In: *The Journal of Chemical Physics* 124.20 (2006), p. 204716. DOI: 10.1063/1.2198536. eprint: http://dx.doi.org/10.1063/1.2198536. URL: http://dx.doi.org/10.1063/1.2198536.

[31] S. R. Schofield, P. Studer, C. F. Hirjibehedin, N. J. Curson, G. Aeppli, and D. R. Bowler. "Quantum engineering at the silicon surface using dangling bonds." In: *Nature Communications* 4 (2013), p. 1694. DOI: 10.1038/ncomms2679. URL: http://dx.doi.org/10.1038/ncomms2679.

[32] "Structure of Si(111) surfaces etched in 40% NH4F: Influence of the doping." In: *Microscopy Microanalysis Microstructures* 5.December 1994 (1994), pp. 291–299. ISSN: 1154-2799.

[33] Datta Supriyo. *Electronic transport in mesoscopic systems*. Cambridge University Press, 1997.

[34] Datta Supriyo. *Quantum Transport. atom to transistor*. Cambridge University Press, 2005.

[35] Marco Taucer, Lucian Livadaru, Paul G. Piva, Roshan Achal, Hatem Labidi, Jason L. Pitters, and Robert a. Wolkow. "Single-Electron Dynamics of an Atomic Silicon Quantum Dot on the H-Si(100)-(2x1) Surface." In: *Physical Review Letters* 112.25 (2014), p. 256801. ISSN: 0031-9007. DOI: 10.1103/PhysRevLett.112.256801. URL: http://link.aps.org/doi/10.1103/PhysRevLett.112.256801.

[36] J.A. Wood, M. Rashidi, M. Koleini, J .L. Pitters, and R.A. Wolkow. "Multiple Silicon Atom Artificial Molecules." In: *ArXiv e-prints* (2016). eprint: 1607.06050.

[37] O Zitouni, K Boujdaria, and H Bouchriha. "Band parameters for GaAs and Si in the 24-k p model." In: *Semiconductor Science and Technology* 20.9 (2005), p. 908. URL: http://stacks.iop.org/0268-1242/20/i=9/a=003.